UNIVERSITEIT GENT

Faculteit Wetenschappen
Vakgroep Vastestofwetenschappen
Voorzitter: prof. dr. P. Clauws

Hydrogen plasma induced defects in germanium and silicon

Johan Lauwaert

Promotor: prof. dr. P. Clauws
Proefschrift voorgelegd tot het behalen van de graad van doctor in de wetenschappen: natuurkunde

Academiejaar 2007-2008

Contents

Dankwoord

In de loop van de jaren die geleid hebben tot dit doctoraatsproefschift heb ik de bijdrage van verschillende mensen bijzonder gewaardeerd.
Als eerste bedank ik mijn promotor Prof. dr. P. Clauws. Door hem werd dit onderzoekswerk mogelijk gemaakt en bovendien heb ik in de loop van de jaren als doctoraatsstudent veel van hem bijgeleerd. Niet alleen op vlak van de experimentele fysica maar ook tijdens het zorgvuldig en geduldig nalezen van mijn teksten. Ik benadruk zijn bijdrage tot dit werk met veel plezier.
Dit FWO-project (G.0344.03) werd mede mogelijk gemaakt door Prof. dr. ir. C. Claeys and dr. ir. E. Simoen (IMEC). Hen had ik graag willen bedanken voor de zinvolle discussies tijdens de projectvergaderingen. Special thanks to dr. ir. E. Simoen and dr. Y.L. Huang (University of Hagen) for the many discussion about hydrogen enhanced donor formation (Even on the beach of Crete) and the silicon samples they made available for infrared spectroscopy. I cannot forget to mention my appreciation for their interest in the results of my research.
During my research I have benefited from the cooperation with different people and research groups: dr. M.L. David (University of Poitiers) for the TEM measurements, dr. J. Debaerdemaeker (Ugent department of subatomic and radiation physics) for positron annihilation spectroscopy, Prof. dr. J. Weber (TU-Dresden) for the invitation to the TU-Dresden and dr. M. Hiller (TU-Dresden) for the raman measurements and the guided tour through the city center of Dresden. I appreciated the introduction they gave about their favorite experimental technique and the contribution to the careful analysis of

my samples.
Mijn collega's uit de defectkarakterisatiegroep: O. De Gryse, S. Hens, A. Hikavyy, P. Vanmeerbeek, J. Van Gheluwe en J. Versluys wil ik graag bedanken voor de aangename sfeer binnen onze onderzoeksgroep. J. Van Gheluwe wil ik nog eens extra bedanken voor de aangename samenwerking tijdens de DLTS metingen van de transitiemetalen in Ge.
Ook wil ik de andere collega's van onze vakgroep bedanken. Met in het bijzonder de Surface Physics and Thin Films group waarmee onze onderzoeksgroep het tweede verdiep deelt: A. Colpaert, R. Van Paemel en G. Notebaert voor de technische ondersteuning en de hulp tijdens het bouwen van de plasma reactor.
Ook Prof. dr. D. Depla wil ik graag persoonlijk bedanken voor zijn spontaan initiatief om vacuummateriaal ter beschikking te stellen voor het bouwen van een eigen plasma opstelling.
Tenslotte wil ik graag mijn familie bedanken voor hun onvoorwaardelijke steun.

Chapter 1

Introduction

A factor which to a major extent determines the properties of semiconductors, the basic materials of the modern electronics, is their impurity content. In this PhD the defects induced in the semiconductors germanium and silicon by means of hydrogen plasma treatments are examined using spectroscopic techniques. An overview of the different chapters is shown in figure 1.1.
In chapter 2 the effect of this hydrogenation on oxygen containing silicon is studied using far-infrared spectroscopy. Oxygen is the most common defect in silicon, due to the Czochralski growth technique and is extensively studied since the fifties. However, the microscopic structure of the electrically active oxygen containing clusters, which can be created using thermal treatments, the so-called oxygen thermal donors (OTD) is still a problem which has not been completely unraveled. It is well-known that the presence of hydrogen can strongly influence the reliability of devices. An example is the catalytic effect of hydrogen on the formation of OTDs, and thus an unexpected amount of additional donors can be formed during the processing of silicon devices. Recently strong indications were obtained by means of Deep Level Transient Spectroscopy (DLTS) in combination with Capacitance Voltage profiling (CV) that hydrogen not only acts as a catalytist for the formation of OTDs but plays an active role in the formation of hydrogen related shallow thermal donors (H-STD). In particular for short annealings ($\approx 20min$) at low temperatures

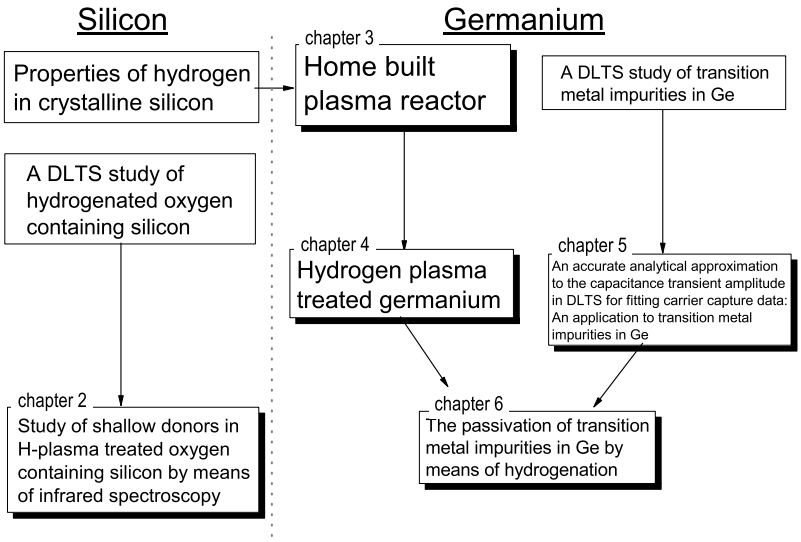

Figure 1.1: Diagram of the chapters of this thesis.

($\approx$ 300°C), which are common in semiconductor technology, an unexpected increase in shallow donors (i.e. with an ionization energy below 50 meV) was observed. To unambiguously link this observation to the creation of H-STDs a selection of samples (hydrogenated at the University of Hagen) were examined by means of far-infrared spectroscopy. Here, for the short annealing a total concentration of donors below the detection limit of absorption spectroscopy was formed and thus it was necessary to use the Photo-Thermal-Ionization spectroscopy (PTIS) variant. It could be concluded that not only the H-STD previously published in the literature were created, but also at least one unreported effective mass-like shallow donor was observed.

A second part of this thesis covers the effect of plasma hydrogenation on germanium. Due to the significantly higher carrier mobility comparing to silicon, germanium based materials are of potential interest for advanced semiconductor applications. The effect of hydrogen on as-grown material, as well as on oxygen containing and on transition metal doped germanium were studied. To introduce high concentrations of hydrogen in germanium a plasma reactor

was built, described in chapter 3. This home built plasma setup was based on the direct plasma reactor used for silicon in chapter 2. The reliability of the system was checked by repeating different effects well-known from literature of hydrogenated silicon.

Chapter 4 covers a characterization study of different defects created in germanium after hydrogenation. The formation of hydrogen related defects in germanium has recently become an interesting topic due to the discovery of semiconductor layer transfer using hydrogen implantation. Hereby it has been shown that plate-like hydrogen clusters are the important defects mediating layer transfer. Due to the presence of observable blisters on the (100) surface, it could be expected that plate-like hydrogen clusters are formed close to the surface. This defect rich region was studied by means of Transmission Electron Microscopy (TEM) (in cooperation with Dr. M.L. David, University of Poitiers), Slow Positron Defect Profiling (in cooperation with Dr. J. Debaerdemaeker, University of Ghent), Infrared Absorption Spectroscopy, Raman spectroscopy (in cooperation with Prof. Dr. J. Weber and Dr. M. Hiller, TU-Dresden) and DLTS. A combination of these characterization techniques made it possible to make a model for the first micrometers beyond the plasma-treated surface. Within the first 300nm, plate-like cavity clusters including Ge-H bonds were observed created by the plasma hydrogenation. We therefore suggest that those cavity clusters are responsible for the blistering germanium surface.

Finally the effect of hydrogenation on germanium implanted with 3d transition metals was studied. Recently a procedure for doping of germanium samples with transition metals suitable for investigation with DLTS, has successfully been developed in our research group, allowing a systematic study of the corresponding deep level parameters. Transition metal impurities in germanium give rise to deep energy levels in the band gap which (even at trace concentrations, e.g. as a consequence of contamination during processing) may affect the electronic properties of the semiconductor. Similar levels act as recombination or generation centers of electrons and holes and influence the lifetime

of carriers or leakage currents in diodes. To extend this standard DLTS study, a unique numerical tool was developed described in chapter 5 to measure the majority carrier capture cross-section for deep levels. The direct observation of the capture cross-section made it possible to correct the emission signature and determine the enthalpy and entropy corresponding with the emission of the carriers. Due to this novel method the reliability of the deep level parameters of transition metal impurity centres could be seriously improved. The data may be considered as a solid basis for comparison with literature data, with future theoretical calculations and for predicting effects of transition metals on devices.

The study of the passivation of the electrical activity of levels within the band gap is described in chapter 6. It is known that hydrogen may be important with respect to passivation of electrically active defects in semiconductors. Concerning transition metal impurities in germanium, convincing evidence of passivation has only been presented for Cu, a triple acceptor that may be passivated partially or completely by formation of CuH_n complexes. A DLTS study of transition metal implanted germanium after hydrogenation is presented. From this it could be concluded that, besides traps related to the radiation damage metal dependent levels could be observed, that could be tentatively assigned to TM hydrogen complexes.

Chapter 2

Study of shallow donors in H-plasma treated oxygen containing silicon by means of infrared spectroscopy

2.1 Introduction

As a results of the Czochralski (Cz) growth technique, oxygen is one of the most common defects in silicon, while molecular hydrogen is present in several steps of the processing of semiconductor materials. Therefore properties of hydrogen and oxygen in semiconductors and in particular in silicon have been frequently studied. An overview of the effects of hydrogen in semiconductors was given in the book 'Hydrogen in crystalline semiconductors' [1]. However even today still some hydrogen related effects are not well understood, one of these is the property of hydrogen plasma to enhance the formation of donors in oxygen containing material. An enhanced formation of oxygen thermal donors (OTDs) was first observed by Brown et al.[2]. Thus it has been accepted until now that the defects which mediate the junction formation in oxygen con-

taining p-type silicon after hydrogen plasma treatments [3] are these OTDs. From a Deep Level Transient Spectroscopy [1](DLTS) study of the formed diodes Simoen et al. [4] concluded that not only the enhanced formation of OTDs but also additional shallower donor defects should be formed. Here the incorporated hydrogen is not only a catalytic element for the formation of OTD but also would play an active role in the formation of hydrogen related shallow thermal donors (H-STD). The small difference between the ionization energy of H-STD and the ionization energy of the dopant is below the detection limits of DLTS and thus no spectroscopic observation was available to identify the donors. In this work we present a far-IR absorption spectroscopy and photothermal ionization spectroscopy (PTIS) study that made it possible to identify the created donors.

2.1.1 Enhanced thermal donor formation

It was observed by Brown et al. [2] that by heating Cz-Si in a hydrogen plasma at a temperature between 350℃-450℃ OTDs are generated by a rate about five times higher than the rate observed after furnace annealing. To exclude the possibility that the exposure to the plasma could lead to surface contamination or damage due to the low-energy ion bombardment or the ultraviolet irradiation, which enhances the OTD formation instead of the presence of hydrogen, different control samples were created. Three types of control samples consist of deuterium plasma, argon plasma and a sample heated under identical hydrogen condition without plasma hydrogenation. The changes observed in resistivity of the argon plasma treated sample correspond with the annealed sample without plasma treatment. Similar enhancement effects were observed for a deuterium as for a hydrogen plasma treated sample. Thus Brown et al. showed that the combination of plasma effects and hydrogen enhances the OTD formation.

[1] A short introduction on DLTS is given as an introduction in chapter 5.

Donor transition cm^{-1}	HD3	HD4	HD5	HD6	HD7
$2p_{\pm}$-1	223.4	236.9	259.6	305.4	371.4
$2p_{\pm}$-2	224.7	237.6	260.2	306.4	372.6
$3p_{\pm}$	249.8	263.4	286.0	332.0	397.8
$4p_{\pm}$	257.0	270.8	293.5	339.4	405.4
$5p_{\pm}$	-	276.7	299.4	345.1	-
$E_i(meV)$	34.1	35.8	38.6	44.2	52.5

Table 2.1: Shallow thermal donor line positions observed after neutron irradiation and hydrogen plasma treatment of Cz-Si by Hartung et al. [8]

2.1.2 Different types of hydrogen related shallow thermal donors

Besides the well-known infrared absorption lines of OTDs [5], other spectra from effective-mass like donors with shallower ground states have been observed in thermally treated Cz-silicon. These are commonly indicated as shallow thermal donors (STDs). The different lines of STDs which have a relation with hydrogen are summarized in table 2.1, 2.2, 2.3 and 2.4. A first series of donors observed by Navarro et al. [6] was created as a result of annealing in a N_2 ambient without hydrogenation. Later in a higher resolution observation of the STDs Griffin et al. [7] concluded that nitrogen plays a catalytic role in the formation behavior of these series.

A second series was detected in neutron irradiation and subsequently hydrogen plasma treated silicon by Hartung and Weber [8]. Due to the observation of a very small isotopical shift for the HD4 to HD7 donor comparing hydrogen to deuterium plasma, it was shown that hydrogen was present as an active part of the defect structure. The observed transitions with a precision of $0.05cm^{-1}$ are given in table 2.1. The high resolution made it possible to resolve a splitting in the $2p_{\pm}$ transition.

The third series was observed by Markevich et al. [9] in silicon saturated with hydrogen using a annealing at 1000℃ in 1 atm hydrogen ambient and then

Donor transition cm^{-1}	D1	D2
$2p_0$	249.7	204.5
$2p_\pm$	291.7	246.85
$3p_\pm$	298.8	254.1
$3p_0$	-	273.35
$4p_\pm$	325.4	280.6
$E_i(meV)$	42.6	37.0

Table 2.2: Shallow thermal donor line position observed in Cz-Si after annealing in a hydrogen ambient 1000℃ and irradiation with fast electrons (3.5MeV) by Markevich et al. [9]

Donor transition cm^{-1}	A	B	C1	C2	C3	D	E	F
$2p_0$	236.8	222.4	215.5	177.4	158.1	-	203.9	204.4
$2p_\pm$	279.2	265.0	258.3	220.4	201.6	208.7	246.6	246.9
$3p_\pm$	305.5	291.4	284.6	-	226.5			
$4p_\pm$		298.9						
$E_i(meV)$	41.0	39.2	38.4			32.3	37.0	37.0

Table 2.3: Shallow thermal donor line position observed in Cz-Si after annealing in flowing hydrogen at 1300℃ by McQuaid et al. [10]

irradiated with fast electrons (3.5 MeV). The lines observed by IR-absorption are summarized in table 2.2.

The fourth series was detected after annealing in a flowing hydrogen gas at 1300℃ by McQuaid et al. [10]. The presence of hydrogen in the core of these donors (except for the donor E) is unambiguously proven by the shift of the ground state after doping with deuterium rather than hydrogen. The concentration as a function of annealing time at 350℃ could be linked to the formation of the OTD and thus it was assumed that these levels are related to partially passivated OTD centers. The lines are summarized in table 2.3.

The fifth series was described by Newman et al. [11] and consists of three

Donor transition cm^{-1}	1	2	3	4	5
$2p_0$	208.7	204.2	198.2	195.2	190.7
$2p_\pm$	253.7	246.7	241.1	238.4	233.7
$E_i(meV)$	37.8	37.0	36.3	35.9	35.4

Table 2.4: Shallow thermal donor line position observed in Cz-Si heated in hydrogen ambient by Newman et al. [11]

families depending on the ambient during thermal treatment: STD(Al)N in annealed Al-doped Si; STD(H)N in samples pre-heated in H_2-gas and STD(X)N in annealed samples pre-heated in N_2-gas (or nitrogen doped silicon). For the STD(H)N-series the presence of the hydrogen atom was demonstrated by the observed chemical shift using deuterium. The line position of the STD(H) series is shown in table 2.4.

A last series of ultra shallow thermal donors was observed by Hara [12] in carbon and nitrogen rich silicon. Although no hyperfine interaction with ^{13}C was observed by electron spin resonance, from the high carbon concentration in the initial sample the centers were tentatively assigned to carbon related centers.

2.1.3 Ab initio calculations: the effect of hydrogen on donor formation

Recently Tsetseris et al.[13] proposed a model for the catalytic role of hydrogen on the formation of OTDs and H-STD. Based on first-principle calculations of different structures they concluded that for the influence of hydrogen different atomistic mechanisms could be distinguished:

1. H^0 and H^+ transform a staggered oxygen chain to a single OTD and they bind to it strongly (i.e. formation of H-STD).

2. H^- binds to a chain and through a subsequent emission of an electron transforms it to a OTD (i.e. enhanced formation of OTDs)

3. At a high enough temperature, the dissociation of the H-STD complex is activated. The released hydrogen diffuses rapidly in Si, it aids O agglomeration, it eventually binds to a new oxygen cluster.

This set of calculations may be compared with the universal alignment of hydrogen calculated by Van de Walle and Neugebauer [14], from which it was concluded that the most stable charge state of interstitial hydrogen is H^+ in p-type material, while the most stable state in n-type is H^-. From the combination of the results from simulation of Tsetseris et al. and Van de Walle et al. one may expect that in p-type the formation of H-STD should be the preferential mechanism, while in n-type one may expect enhanced formation of OTDs.

2.2 N-type Czochralski silicon

A first type of samples were called SiOH-samples (silicon, oxygen and hydrogen). The formation of OTDs is studied in direct plasma hydrogenated n-type Cz silicon after annealing at 450℃. N-type phosphorus doped silicon with a concentration of $10^{15} cm^{-3}$ was used as starting material. An interstitial oxygen concentration of $(7-8) \times 10^{17} cm^{-3}$ and substitutional carbon concentration of $2 \times 10^{16} cm^{-3}$ was measured by means of infrared absorption spectroscopy of the vibrational bands at $1107 cm^{-1}$ and 605 cm^{-1} respectively [4]. The hydrogenation was performed at the University of Hagen. The samples were exposed to a direct RF hydrogen plasma in a Plasma Enhanced Chemical Vapor Deposition (PECVD) reactor. The plasma frequency and power were set to 110MHz and 50W respectively. The substrate temperature during this process was stabilized at 270-280℃. The post-hydrogenation annealing was carried out at 450℃ in air.

The formation of donors due to the plasma hydrogenation is demonstrated using 1MHz C-V profiling shown in figure 2.1 [4]. The increase in free carrier concentration in the plateau beyond a distance of $1.5 \mu m$ from the interface could be described by the OTD enhancement effect of the hydrogen. Wagner

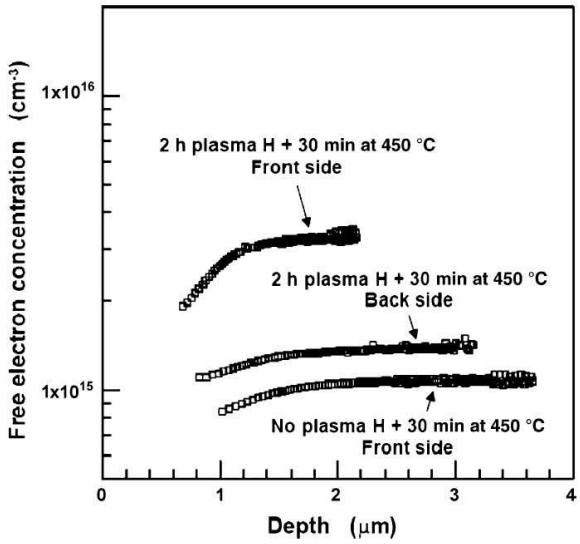

Figure 2.1: Free carrier profiles derived from 1 MHz C-V measurements on material annealed for 30 min at 450℃ (figure taken from Simoen et al. [4]).

[5] measured a formed OTD concentration for an interstitial oxygen concentration of $10^{18}cm^{-3}$, of $2 \times 10^{14}cm^{-3}$ for a sample which had an annealing for 30 minutes at 450℃. Due to the double donor character of the OTDs this corresponds with an increase in electron concentration of $4 \times 10^{14}cm^{-3}$. Due to the lower O_i concentration comparing to the samples in the publication of Wagner one expects that the concentration of additionally created free electrons by the formed OTDs without preceding plasma hydrogenation is below $4 \times 10^{14}cm^{-3}$. This change is within the error of the capacitance voltage profiling technique. It should be noted that the decrease in carrier profile closer to the surface was ascribed to the out-diffusion of hydrogen during the anneal at 450℃ in air. The back-side shows a significant increase in free electrons and thus it could be argued that a significant concentration of hydrogen reaches the backside of the $400\mu m$ thick wafer. From the increase in donor concentration at the front side of the sample it could be seen that under assumption that this is due to the OTDs (i.e. taking into account of the double donor character), a concentration of $1.1 \times 10^{15}cm^{-3}$ was formed. This is much higher than the expected

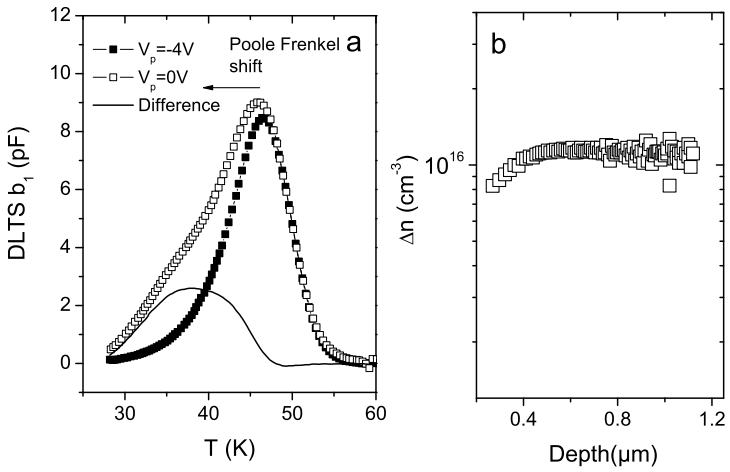

Figure 2.2: (a) DLTS-spectrum plot corresponding to a 1h plasma hydrogenated and 30h annealed n-Cz Si sample at (450℃). (b) Corresponding free carrier profile derived from a C-V measurement at 1MHz. (data made available by Simoen reference [4].)

$2 \times 10^{14} cm^{-3}$ according to Wagner and is even for a lower O_i concentration. Comparing to the sample without a preceding plasma treatment and an increase in free electron concentration of $< 10^{14} cm^{-3}$ the enhancement effect corresponds at least with a factor of 11. From the DLTS-spectrum a trap concentration of the $OTD^{+/++}$ peak of $1.7 \times 10^{14} cm^{-3}$ was observed. Comparing this with the increase in free carrier concentration ($2.2 \times 10^{15} cm^{-3}$) it is clear that the OTD cannot account for the free carrier density increase. And it can be concluded that no enhancement of OTD could be observed comparing to the measurements of Wagner. [5]

As shown in detail by Rafi et al. [15] one expects that the hydrogen effects die out for longer annealing times. A detail of the DLTS spectrum after a 30h annealing is shown in figure 2.2. From a capacitance voltage profile one can deduce an increase in free carrier concentration of $\approx 10^{16} cm^{-3}$. To determine the concentration of OTDs via DLTS-spectroscopy, one should keep in mind that different OTD-species contribute to the DLTS peak. Therefore it is dif-

ficult to include a pulse-correction factor to calculate the trap concentration. A good approximation for the λ-correction is given by [16]:

$$\frac{\Delta C}{C_\infty} = \frac{1}{2}\left(\frac{N_T}{n_0}\right)\frac{V_r - V_p}{V_r + V_{bi}} \tag{2.1}$$

Where ΔC is the transient amplitude, which is proportional to the b_1 fourier coefficient shown in figure 2.2, C_∞ is the quiescent capacitance for V_r (the reverse bias), V_p is the pulse bias, V_{bi} is the Schottky barrier height, N_T is the trap concentration and n_0 is the equilibrium free electron concentration. The n_0 concentration profile is shown in figure 2.2. From this constant profile with $n_0 = 10^{16} cm^{-3}$ and assuming an abrupt junction the electrical field within the depletion region can be calculated. From this using the field enhanced emission for the OTDs [17] a difference in emission activation of $15meV$ should be observed between -6V and -4V and -4V and 0V, this can explain the observed Poole-Frenkel shift shown in figure 2.2. Using equation (2.1) $\frac{N_T}{n_0}$ for the $OTD^{+/++}$ peak is 0.35. It may be noted that no correction for the width of the DLTS band was included. This makes that 70% of the free electrons at room temperature are due to the presence of the OTDs. From the DLTS-amplitude a trap concentration for the $OTD^{+/++}$ peak gives $3.5 \times 10^{15} cm^{-3}$, which is in very good agreement with the value measured by Wagner [5] for an as annealed sample. Thus the OTD concentration can account for the increase in carrier concentration due to the plasma treatment in combination with the 30h additional annealing. From the DLTS experiment it can be concluded that although strong enhancements effects could be observed for short annealing ($\leq 3h$), for long annealings ($\approx 30h$) the enhancement effect dies out.

To observe the remaining effect of the hydrogenation the 30h annealed sample was made available for absorption measurements in the far-infrared region. The absorption spectrum is shown in figure 2.3 (a). In the region between 400 and 600 cm^{-1} the absorption peaks are due to the neutral state of the OTD center. It may be seen that the absorption peaks of the OTDs species OTD1 to OTD6 are present. The line corresponding to the $1s \rightarrow 2p_\pm$ transition is labeled in the figure with the number of the OTD. The absorption peak at $315 cm^{-1}$ is the due to the $1s \rightarrow 2p_\pm$ transition of the dopant phosphorus. The

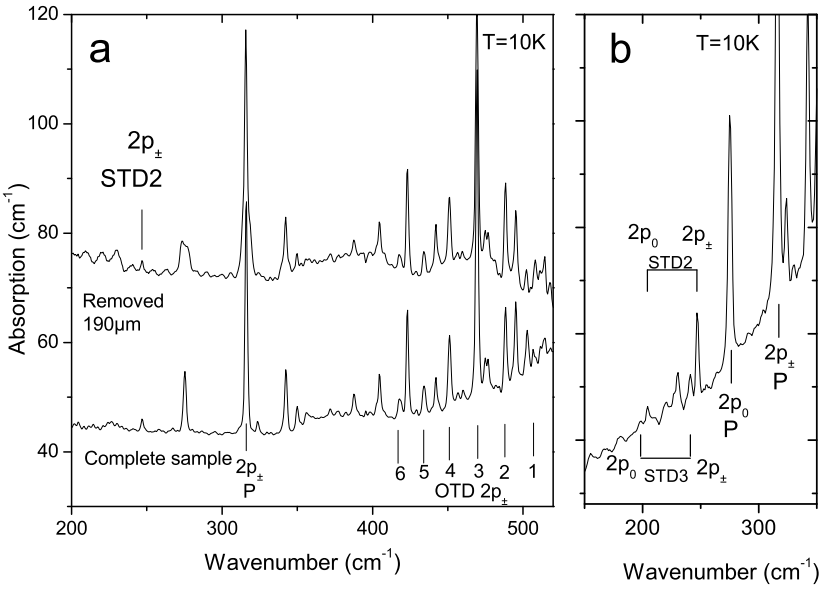

Figure 2.3: (a) Absorption spectrum corresponding to a 1h plasma hydrogenated and 30h annealed n-Cz sample at (450°C). The lines due to the OTD transitions $1s \rightarrow 2p_{\pm}$ are labeled 1 to 6 (b) absorption detail of a stack of four samples.

small feature at $246cm^{-1}$ is the $2p_{\pm}$ line due to the H-STD2 discovered by Newman et al.[18]. Using the optical cross-sections for the $2p_0$ lines measured by Wagner an average concentration over the sample thickness can be determined. The total concentration of OTDs in the neutral state is $3.6 \times 10^{15} cm^{-3}$, in very good agreement with the $OTD^{+/++}$ trap concentration calculated from the DLTS result. Not only the total OTD concentration corresponds with the expectations for as-annealed material, but also the sequence of OTD concentrations corresponds with the optical measurements of Wagner [5]. Figure 2.4 (a) shows that:

$$[OTD_3] > [OTD_4] > [OTD_2] > [OTD_5] > [OTD_6]$$

which is in agreement with the result for an annealing period of $\approx 15h$, in the paper of Wagner (where the O_i concentration is somewhat higher). Thus this

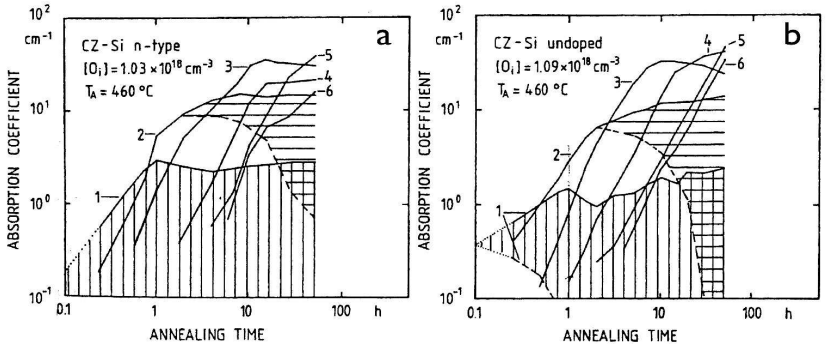

Figure 2.4: Absorption amplitudes of the $2p_{\pm}$-lines of neutral OTDs versus annealing time for (a) n-type (b) undoped samples (figure taken from Wagner [5]). Full lines refer to the results obtained when the sample was cooled under illumination. The dashed lines give the measured absorption coefficients when the sample was cooled in darkness.

sequence supports the conclusion that no significant enhancement effect of the formation of thermal donors is observed in this case. To check whether a defect profile may be observed as an effect of the plasma treatment, the absorption spectrum was recorded with $190\mu m$ of the sample mechanical removed by means of polishing. Comparing with the absorption spectrum for the complete sample one can conclude that a homogeneous spatial distribution of H-STD and OTD centers is present in this sample.

It could be argued that the only effect of the preceding hydrogenation is the presence of the H-STD. Figure 2.3 b shows a detail of the measured absorption spectrum for a stack of 4 wafers, this made it possible to detect not only H-STD2 which has the largest concentration but also the H-STD3 species. Newman et al. [18] showed that those species are present in a hydrogenated boron-doped Si-sample following an anneal at 470°C for 22h and are related to the NL10 EPR-spectrum. The presence of hydrogen in these centers and the relation to the NL8 spectrum, which could be assigned to the OTD^+ defect was shown by Martynov et al. [19].

2.3 N-type high-resistive magnetic Czochralski

High resistivity magnetic Czochralski (MCz) silicon has applications for complementary metal-oxide-semiconductor (CMOS) devices due to the significant lower high frequency noise coupling. It was shown that MCz-silicon is also a good material for the fabrication of radiation-hard detectors. In contrast to float zone wafers, which are usually applied for similar detectors and which have to be intentionally doped with oxygen, the MCz wafers intrinsically contain $10^{17} - 10^{18} cm^{-3}$ oxygen. On the other hand, hydrogen is used in many steps in the CMOS process, and it is known that hydrogen plasma enhances the formation of OTDs.

N-type High Resistive MCz silicon ($> 500\Omega cm$) wafers from Okmetic are used as starting material. This corresponds, using a drift mobility of $1500 cm^2 V^{-1} s^{-1}$ [20], with a maximum free carrier concentration of $8 \times 10^{12} cm^{-3}$. From Fourier transform infrared absorption spectroscopy an interstitial oxygen concentration of $(2 - 5) \times 10^{17} cm^{-3}$ was measured. Hydrogen plasma treatments were carried out by exposing the wafers directly to the plasma for 2 hours at 270℃. Additional isochronal anneals were performed for 20 minutes at different temperatures between 300℃ and 450℃. Huang et al. [21] argued by means of DLTS that the created excess electrons are due to both OTD and H-STD centers. The relative concentration is strongly dependent on the temperature (see figure 2.5) and it could be seen that for low temperatures (<400℃) most of the free electrons are from the H-STD centers while for higher temperatures (>400℃) mostly the OTD are formed. This was also confirmed by the C-T plots shown in figure 2.6. For the sample with an anneal at 450℃ the freeze-out of the $OTD^{+/++}$ and $OTD^{0/+}$ were clearly visible, while for the lower temperature anneals no OTD related freeze outs could be observed and still some excess electrons were created. From this result it is clear that a more shallow center donates those free electrons to the conductions band, but no real spectroscopic evidence for this idea could be given at that time. In this manuscript we present PTIS measurements that made it possible to identify those donors.

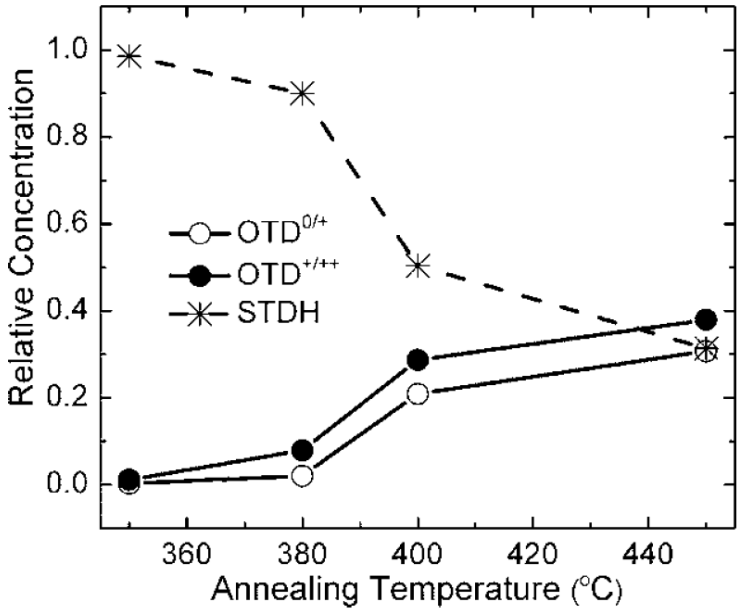

Figure 2.5: Relative concentrations of excess electrons contributed by various donor levels plotted as a function of temperature of the isochronal annealing. All concentrations have been normalized to the total concentration of the excess electrons. The H-STD centers are considered as single donors (figure taken from Huang et al. [21].)

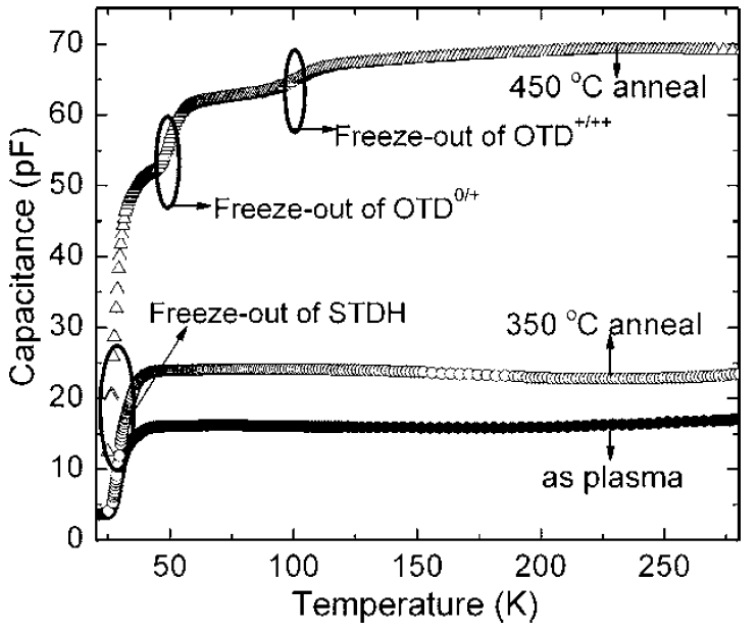

Figure 2.6: Free carrier concentration profiles for HR MCz silicon exposed to various treatments (hydrogen plasma exposure and post hydrogenation annealing) as well as for the as-plasma substrate. (figure taken from Huang et al. [21].)

In order to observe the type of H-STD that contributes to the increase in free electrons, a sample with a 20 minute anneal at 310℃ was selected. For this sample it could be concluded from DLTS measurements that the increase in carrier concentration is not due to the enhanced OTD formation but from a more shallow donor species. Due to the low donor concentration ($\approx 10^{13} cm^{-1}$) below the detection limit of infrared absorption for a $\approx 300 \mu m$ wafer, the ideal technique for observing these donors is PTIS. A short introduction is given below.

2.3.1 Photo-thermal-ionization spectroscopy

PTIS was discovered in 1964 by Lifshitz and Nad; a recent review is given by Lifshitz in reference [22]. The main advantage of PTIS is a detection limit for electrically active impurities, which is lower than the detection limit of any

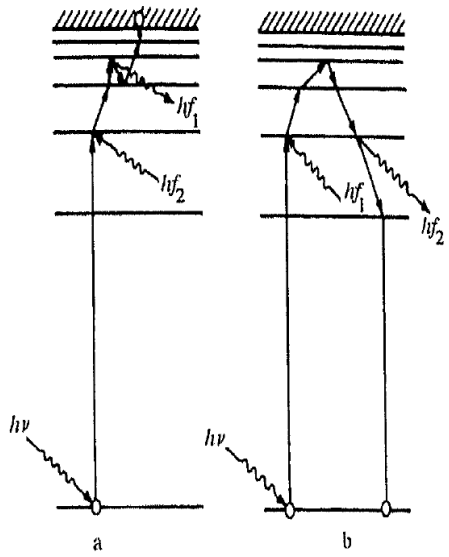

Figure 2.7: Diagram of thermal transitions in an optically excited impurity atom. The two possible outcomes of these transitions are: (a) ionization of the atom, (b) return to the ground state; $h\nu$ is the photon energy and hf_i is the phonon energy. (figure taken from Lifshits [22].)

other analytical method. The PTIS mechanism consists of a coherent process of both optical excitation and thermal ionization of the impurity. One can understand that not every impurity atom is ionized by the external perturbation and thus some carriers roam between excited states and may return to the ground state (see figure 2.7). Since there are only two different paths, the sum of the probability of the return to the ground state from the n-th excited state $S^{(n)}$ and the ionization probability $I^{(n)}$ should be one:

$$S^{(n)} + I^{(n)} = 1 \tag{2.2}$$

The photo thermal-ionization cross-section $\sigma_i(\nu)$ can be expressed in terms of the optical-absorption cross-section $\sigma(\nu)$ and the thermal ionization probability $I^{(n)}$:

$$\sigma_i(\nu) = \sigma(\nu) I^{(n)}. \tag{2.3}$$

To measure the photoconductivity two contacts are made on the semiconductor and the sample is connected in series with a voltage (U) supply and a load

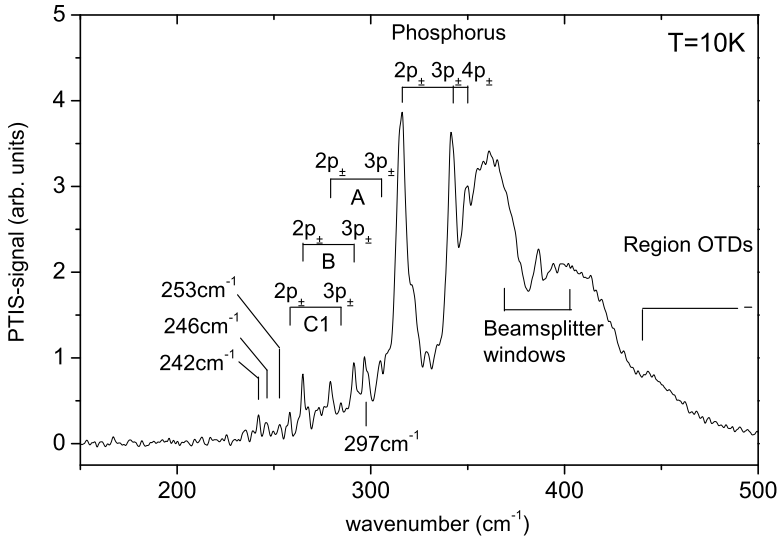

Figure 2.8: PTIS of n-type MCz silicon hydrogenated and annealed at 310℃ for 20 minutes.

resistor R_L. In this simple circuit one can see that the signal U_{ph} caused by the flux of the photons is proportional to the variation of the semiconductor conductivity and thus proportional to the variation in free carrier concentration Δn_0. With a specimen resistance R_S in equilibrium, the signal can be written as:

$$U_{ph}(\nu) = \frac{U}{1 + \frac{R_S}{R_L}} \frac{\Delta n_0(\nu)}{n_0} \tag{2.4}$$

Because the goal is to observe the created donors in the layer close to the surface the two contacts were made on top of this side of the sample.

2.3.2 The formed shallow thermal donors

Figure 2.8 shows a PTIS measurement for the sample which had an additional anneal at 310℃. The PTIS-spectrum was recorded after cooling with additional illumination using a He-Ne laser of the sample to freeze the bistable OTD1 and OTD2 in their electrically active configuration. Comparing this anneal tem-

perature to the observed trend in the fractional contribution of the H-STD to the free carriers in figure 2.5, one can conclude that all the additional carriers are due to the creation of H-STD.

The PTIS spectrum shown in figure 2.8 consists of a broad band and photo current peaks between $200cm^{-1}$ and $350cm^{-1}$. The broad band or photo-continuum originates from electrons directly excited from the defect ground state into the conduction band. In this case all the donor defects present contribute to this band. The higher wavenumber cut-off of the continuum and the negative peaks in the region of $380cm^{-1}$ are due to the beamsplitter and cryostat windows. The absence of characteristic lines in the region $400 - 500cm^{-1}$ demonstrates that no OTD defects are present, which is in agreement with DLTS. The characteristic defect lines, which can be seen on the lower wavenumber side of the continuum originate from excitation of shallow donors. It can be seen that not only the dopant phosphorus contributes to the conductivity, but also other effective mass like defects have been formed during the hydrogenation and additional annealing. The lines at $316.6cm^{-1}$, $342.6cm^{-1}$ and $350cm^{-1}$ have been assigned to the $2p_{\pm}$,$3p_{\pm}$ and $4p_{\pm}$ transitions of phosphorus respectively. The presence of the H-STD in the sample can be seen from the PTIS-lines at $279.3cm^{-1}$ and $305.5cm^{-1}$, $265.0cm^{-1}$ and $291.4cm^{-1}$ and $258.3cm^{-1}$ and $284.6cm^{-1}$, which have been assigned to the $2p_{\pm}$ and $3p_{\pm}$ of the A,B and C1 type STD respectively [10] (see also table 2.3). Other features in the region of $250cm^{-1}$ (most important peaks at 242, 246 and 253 cm^{-1}) and the peak at $297cm^{-1}$ appearing well above the noise level are due to previously unreported lines. Although these lines are possibly related to unknown shallow donors, the absence of identifiable donor series does not allow to draw firm conclusions in this respect. If we assume the same PTIS-cross-section $\sigma_i(\nu)$ for the $2p_{\pm}$ lines of the defects as equal, we can conclude that 91%, 3%, 4% and 2% of the free carrier concentration are due to the Phosphorus, A, B and C1 type of H-STD. It should be emphasized however that the P donor is present in the whole thickness of the sample, while the H-STD are possibly formed in a layer near the treated surface, where their

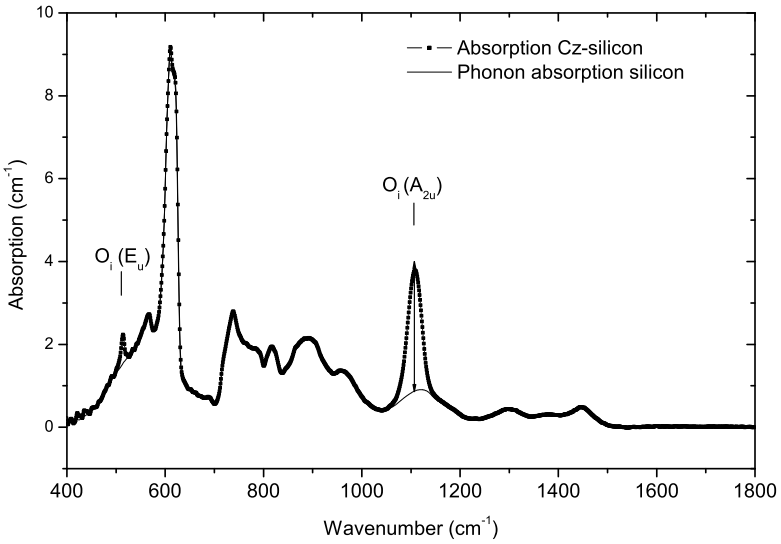

Figure 2.9: Room temperature absorption spectrum of Cz-silicon to measure the oxygen concentration. The amplitude of the O_i A_{2u} line corresponds with a concentration of $9 \times 10^{17} cm^{-3}$

relative concentration may be much higher. Finally one can conclude that this observation of the donor species (i.e. mainly the H-STD series of McQuaid et al.) is in agreement with the conclusion drawn from the DLTS-study of Huang et al. [21].

2.4 P-type Czochralski silicon

The enhanced donor formation by means of hydrogen is of potential interest for the creation of low-budget diodes. Starting with initially homogeneous oxygen containing p-type silicon, plasma hydrogenation can thus form deep junctions. P-type Cz silicon wafers with a boron concentration of $1.2 \times 10^{15} cm^{-3}$ were used as starting material. An interstitial oxygen concentration of $9 \times 10^{17} cm^{-3}$ was measured by means of Fourier transform IR-absorption spectroscopy as shown in figure 2.9.

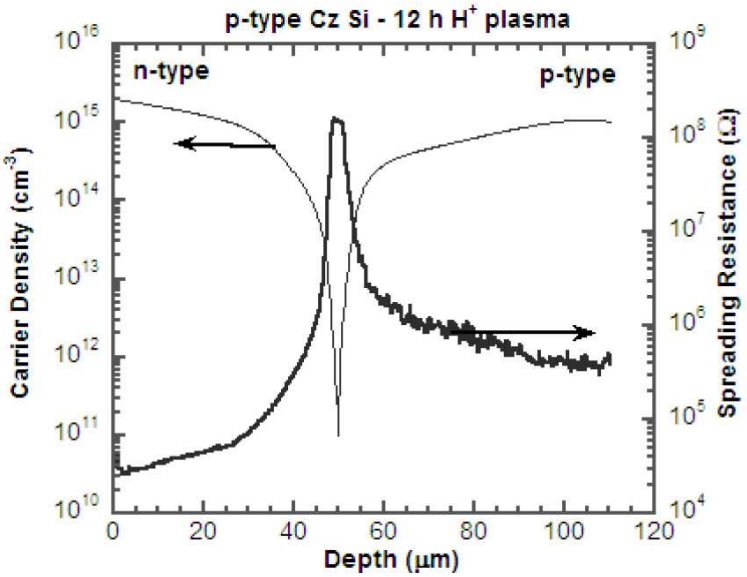

Figure 2.10: Spreading resistance profile of P-Cz Si hydrogenated at 270℃ for 12h, without additional anneal. (Measurement carried out at IMEC Leuven)

The hydrogen-plasma exposure was operated in a parallel-plate PECVD system with a constant substrate temperature of about 260-270℃ for 6 or 12 hours (University of Hagen, Germany). Afterwards different parts were isochronically annealed at 275-500℃ for 20 minutes.

Figure 2.10 shows the spreading resistance profile (SRP) after hydrogenation at 270℃ for 12h without additional anneal. It shows that a p-n junction is created at a depth of about $48\mu m$, and thus it is clear that in this region donors have been created with a concentration higher than the initial boron concentration ($1.2 \times 10^{15} cm^{-3}$). It should be mentioned that the plasma temperature is above the 200℃ below which the boron-hydrogen complex is stable, and thus no boron passivation is expected. It may be noted that the p-type saturation value of $1.1 \times 10^{15} cm^{-3}$ is in excellent agreement with the boron doping concentration. From the free carrier concentration in the n-type region adjacent to the surface exposed to the plasma, the formed donor concentration can be calculated. Due to the absence of boron passivation at this temperature, we suggest that the n-type region is formed by over-compensation of the boron

acceptors by donor centers. The highest free carrier density at the plasma-exposed side amounts to $2 \times 10^{15} cm^{-3}$. Thus a $3.2 \times 10^{15} cm^{-3}$ donors must have been created close to the surface. This concentration corresponds with resistivity values obtained by Wagner [5] for a much higher annealing temperature of 460℃, and thus a significant enhancement of formation of donors is expected. It is clear that the enhancement effect of the hydrogen treatment is visible in the carrier profile measured using SRP and that a diffusion-like enhancement effect of the donor creation could be observed.
In order to identify the shallow donors, PTIS measurements have been performed on two samples, which have been exposed to a hydrogen plasma for 12h and subsequently annealed at 300℃ for (a) 0 min and (b) 20 minutes. The PTIS-spectra are shown in figure 2.11 and can be divided in two parts: a broad continuum with negative peaks superimposed and at lower wavenumbers positive PTIS-peaks due to shallow donors. In both cases, the negative peaks appear at the position of the well-known absorption lines of the boron acceptor which are observed here without additional illumination of the sample during the measurement. The features are interpreted as normal absorption from the uncompensated boron present in the p-type side of the sample. This absorption diminuates the intensity of the light, which is multiply reflected in the sample and which gives rise to the photo conductive continuum of the shallower donor states. This observation suggests that by choosing the coplanar contacts on the n-type side, the p-n junction prevents the uncompensated boron at the back side to contribute directly to the electrical signal. The remaining interference fringes in the photocurrent-continuum of figure 2.11 confirm that the PTIS-signal is generated by light undergoing multiple reflections.

A comparison between the PTIS-spectra (a) and (b) in Fig 2.11 shows the creation of different shallow donor species by the different treatments. In the 20 minutes annealed sample (b) we observe a signal, which involves the B and C1 hydrogen-related shallow donor centers (H-STD) observed by McQuaid et al. [10]. The latter defects have been detected in n-type silicon after annealing at 1300℃ in flowing hydrogen gas and subsequently annealed at 350℃. The

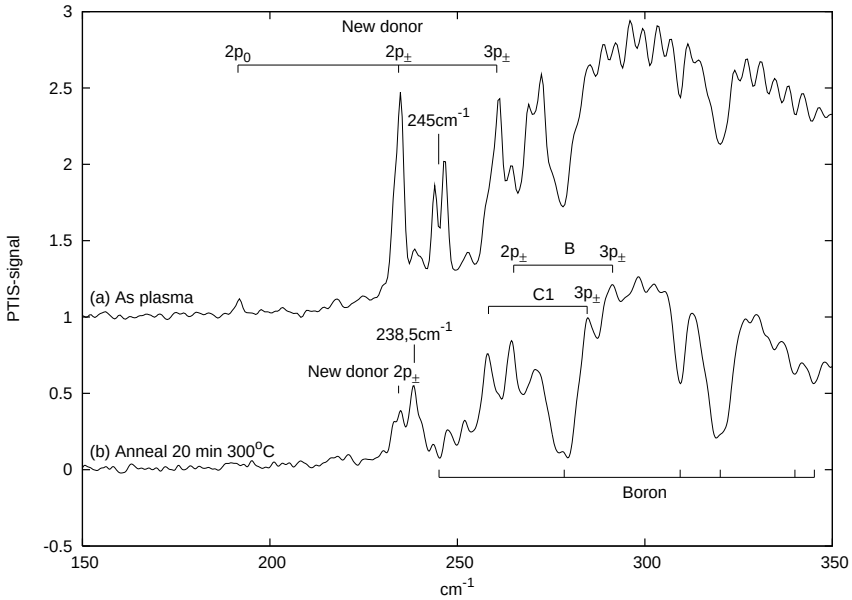

Figure 2.11: PTIS-spectra for the silicon samples hydrogenated for 12h, with an additional anneal of (a) 0 min and (b) 20 min at 300℃. Sample temperature during measurements T=23K

positive lines at 265.0 and 291.4 cm^{-1} in figure 2.11 (b) could be assigned to transitions to the $2p_{\pm}$ and $3p_{\pm}$ excited states of donor species B, respectively. The peaks at $258.3cm^{-1}$ and $284.6cm^{-1}$ correspond with the transitions to the $2p_{\pm}$ and $3p_{\pm}$ states of the strongest bound ground state C1 of the C defect. Although a peak at $238.5cm^{-1}$ is also clearly resolved, the lack of other lines conform the Effective Mass Theory (EMT) makes it impossible to assign it to a type of defect.

It is also shown in figure 2.11 (a) that the plasma hydrogenation at 270℃ has resulted in the formation of a so far unidentified effective-mass like shallow donor. Table 2.5 summarizes the measured lines and the wavenumber difference between the excited states compared with corresponding values according to the EMT [16, 23].

The $2p_{\pm}$ line at $234.3cm^{-1}$, which has the strongest contribution to the conductivity, remains visible in the sample after the 20 minutes 300℃ annealing. This indicates that the defect is still partially present after the 300℃ treatment.

	EMT (cm^{-1})	Donor (cm^{-1})
line		
$2p_0$		191.5
$2p_\pm$		234.3
$3p_\pm$		260.8
ΔE		
$2p_0 - 2p_\pm$	41.05	42.8
$2p_\pm - 3p_\pm$	26.47	26.5
E_i (meV)	31.26	35.4

Table 2.5: Line positions of the unidentified effective mass like shallow donor created after 12h plasma treatment shown in figure 2.11. The lines are labeled with the final state of the corresponding transition from 1s. The binding energy E_i for the donor has been calculated assuming that the $2p_\pm$ state has a binding energy of 6.8meV

Extra PTIS-peaks around $245cm^{-1}$ can be seen in the as plasma treated sample, which probably correspond to another donor defect. However, additional absorption at this wavelength from substitutional boron excitations makes it difficult to distinguish the contribution to the photo current from this defect.

As identified by the PTIS-spectra, not only H-STD but also the early species OTD1 and OTD2 are created in the two samples. Figure 2.12 shows the PTIS-spectra in the higher wavenumber range for different sample temperatures. It may be noted that not all the excited states of the OTD defect are observed. For the highest temperature where the OTD defects are ionized in the singly positive charge state, only the $3p_\pm$ and $4p_\pm$ transition and for the low temperature where the OTD are neutral only the $2p_\pm$ transition is observed.

In PTIS the probability for thermal ionization from the n-th excited state can be written as [24]:

$$I^{(n)} = (1 + \frac{\Delta E^{(n)}}{k_B T}) e^{-\frac{\Delta E^{(n)}}{k_B T}} \tag{2.5}$$

where $\Delta E^{(n)}$ is the binding energy for the (n)-th excited state. The total

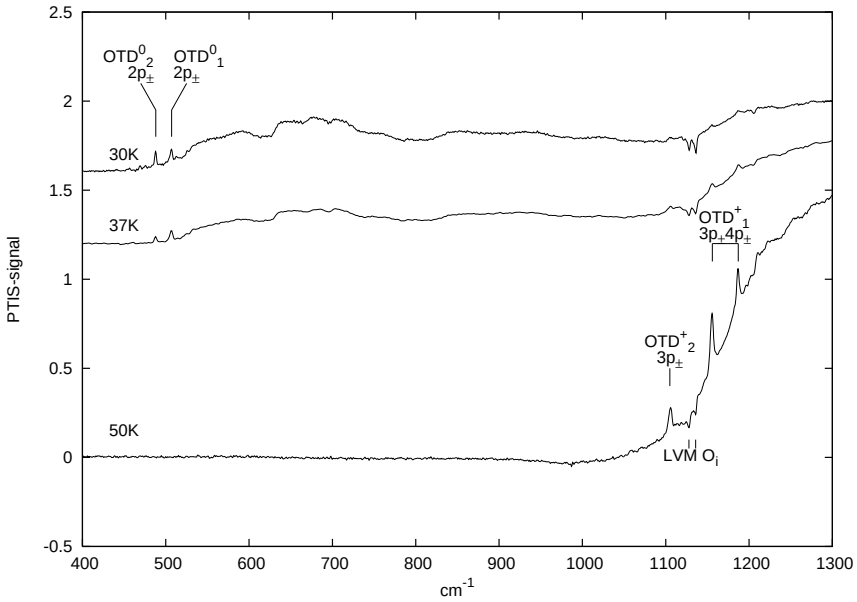

Figure 2.12: Mid-infrared PTIS-spectra for the as-plasma treated sample showing the presence of OTD_1 and OTD_2 in the n-type region of the treated specimens for different sample measuring temperature. Similar spectra were observed after 300℃ anneal for 20 minutes.

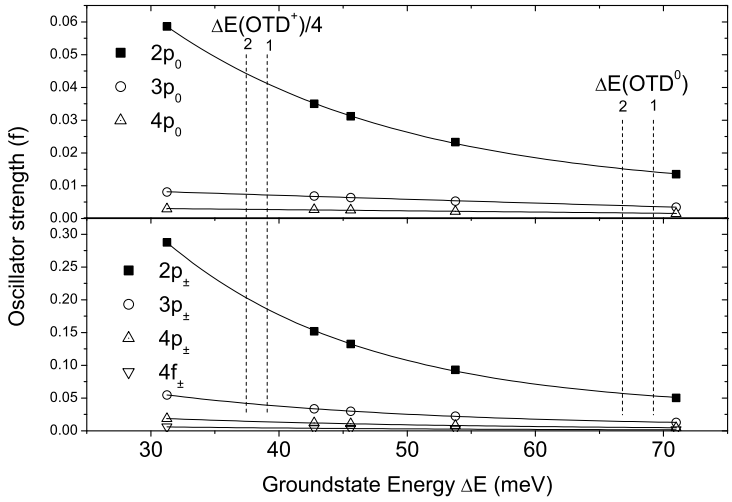

Figure 2.13: Oscillator strength as a function of binding energy for shallow donors, data taken from Clauws et al. [25]. Lines corresponds with a fit using the empirical relation in equation 2.6

ionization probability is obtained by formula (2.3) where the absorption cross-section $\sigma(\nu)$ is proportional to the oscillator-strength of the corresponding optical transition. To estimate this oscillator strengths we have interpolated the oscillator strength calculated by Clauws et al. [25] for substitutional donors in silicon to other binding energies, using an empirical exponential trend:

$$f = \alpha_1 e^{\beta(\Delta E_i)} + \alpha_2 \tag{2.6}$$

with α_1, α_2 and β empirical constants and ΔE_i the binding energy of the ground state for the neutral OTD. For the He^+-like ground state of the ionized OTDs the ground state energy should be divided by 4 due to the 2 times positively charged core. The observed fitted trends are shown in figure 2.13.

Combination of equations (2.5) and (2.6) makes it possible to estimate the proportionality of the different characteristic PTIS-lines for a given defect structure. Using the data of Wagner and Hage [26] for the energy position of the different electronic states of the thermal donors, the observed PTIS intensities

line	OTD_1^+	OTD_2^+	OTD_1^0	OTD_2^0
T	50K		30K	
$2p_\pm$	2.75E-03	3.13E-03	<u>1.58E-02</u>	<u>1.70E-02</u>
$3p_\pm$	<u>8.06E-03</u>	<u>8.79E-03</u>	8.95E-03	9.57E-03
$4p_\pm$	<u>5.18E-03</u>	-	4.02E-03	-
$2p_0$	4.35E-06	5.31E-06	7.51E-04	8.25E-04

Table 2.6: Oscillator strength multiplied by the ionization probability for the electrical transitions of the OTD 1 and 2 species. Strongest lines corresponding with the observation are underlined.

can be explained. The calculated oscillator strength multiplied by the ionization probability is given in table 2.6. Although the oscillator strength of the $2p_\pm$ line is the largest it could be noted that for 50K the two most intense lines are the $3p_\pm$ and $4p_\pm$ line. For 30K in the neutral OTD species the strongest line is the $2p_\pm$, which corresponds with the observations. The observed PTIS-lines for the OTDs as a function of sample temperature can thus qualitatively be explained. However the observation of OTD^+ for a sample temperature of 50K is rather unexpected. For such a high netto donor concentration (i.e. at least $10^{15}cm^{-3}$ donors are created) it is impossible that the Fermi-level lies below the donor ionization energy for temperatures of 50K. Indeed by solving the neutrality equation for $10^{15}cm^{-3}$ donors with an ionization energy of 60 meV one obtains that 90% is ionized at 96K, which is remarkably higher than the sample temperature during the measurement (i.e. 50K). Why we were able to observe a spectrum of OTD^+ species in absence of the OTD^0 peaks remains an open question.

2.5 Conclusions

The infrared experiments described in this chapter have allowed to confirm the hypothesis that due to plasma hydrogenation of silicon not only enhanced OTD formation takes place but also H-STDs are formed. The donors formed in

different circumstances have been spectrscopically identified. Since the donors are formed in a layer of a not well known thickness, it is difficult however to make an accurate calculatioon of the local concentration based on infrared results only. The results are, however, in general agreement with the DLTS data. Among the H-STD formed we were able to identify species described by Newman et al. [11] and McQuaid et al.[10]. Also new features have been observed, including a new effective-mass donor.

Bibliography

[1] S.J. Pearton, J.W. Corbett, and M. Stavola. *Hydrogen in crystalline semiconductors*. Springer, 1991.

[2] A.R. Brown, M. Claybourn, R. Murray, P.S. Nandhra, R.C. Newman, and J.H. Tucker. Enhanced thermal donor formation in silicon exposed to a hydrogen plasma. *Semiconductor science and technology*, 3:591, 1988.

[3] A.G. Ulyashin, Y.A. Bumay, R. Job, and W.R. Fahrner. Formation of deep p-n junctions in p-type czochralski grown silicon by hydrogen plasma treatment. *Applied physics A*, 66:399, 1998.

[4] E. Simoen, C. Claeys, J.M. Rafi, and A.G. Ulyashin. Thermal donor formation in direct-plasma hydrogenated n-type czochralski silicon. *Materials science and engineering B*, 134:189, 2006.

[5] P. Wagner. Infrared absorption studies of thermal donors in silicon. *Material research society symposium proceedings*, 59:125, 1986.

[6] H. Navarro, J. Griffin, J. Weber, and L. Genzel. New oxygen related shallow thermal donor centres in czochralski-grown silicon. *Solid state communications*, 58(3):151, 1986.

[7] J.A. Griffin, J. Hartung, J. Weber, H. Navarro, and L. Genzel. Photothermal ionization spectroscopy of oxygen-related shallow defects in crystalline. *Applied physics A*, 48:41, 1989.

[8] J. Hartung and J. Weber. Shallow hydrogen related donors. *Physical review B*, 48(19):14161, 1993.

[9] V.P. Markevich, M. Suezawa, and K. Sumino. Radiation-induced shallow donors in czochralski-grown silicon crystals saturated with hydrogen. *Journal of applied physics*, 76(11):7347, 1994.

[10] S.A. McQuaid, R.C. Newman, and E.C. Lightowlers. Hydrogen-related shallow thermal donors in czochralski silicon. *Semiconductor science and technology*, 9:1736, 1994.

[11] R.C. Newman, M.J. Ashwin, R.E. Pritchard, and J.H. Tucker. Shallow thermal donors in silicon: The role of Al, H, N and point defects. *Physica status solidi b*, 210:519, 1998.

[12] A. Hara. Hydrogen like ultrashallow thermal donors in silicon crystals. *Japanese journal of applied physics*, 34:3418, 1995.

[13] L. Tsetseris, Sanwu Wang, and S.T. Pantelides. Thermal donor processes in silicon and the catalytic role of hydrogen. *Applied physics letters*, 88(5):051916, 2006.

[14] C.G. Van de Walle and J. Neugebauer. Universal alignment of hydrogen levels in semiconductors, insulators and solutions. *Nature*, 423:626, 2003.

[15] J.M. Rafi, E. Simoen, C. Claeys, Y.L. Huang, A.G. Ulyashin, R. Job, J. Versluys, P. Clauws, M. Lozano, and F. Campabadal. Impact of direct plasma hydrogenation on thermal donor formation in n-type cz silicon. *Journal of the electrochemical society*, 152(1):16, 2005.

[16] P. Clauws. *Spectroscopische methodes voor de bepaling van defecten in halfgeleiders; identificatie en studie van de fysische eigenschappen van thermische donors in zuurstofrijk germanium.* Universiteit Gent, 1991.

[17] L.C. Kimerling and J.L. Benton. Oxygen-related donor states in silicon. *Applied physics letters*, 39(5):410, 1981.

[18] R.C. Newman, M.J. Ashwin., R.E. Pritchard, J.H. Tucker, E.C. Lightowler, T. Gregorkiewicz, I.S. Zevenberg, R. Falster C.A.J. Ammerlaan, and M.J. Binns. Shallow thermal donors in annealed cz silicon and links to the NL10 EPR spectrum: the relevance of H, Al and N impurities. *Materials science forum*, 258:379, 1997.

[19] Y.V. Martynov, T. Gregorkiewicz, and C.A.J. Ammerlaan. Endor identification of a hydrogen-passivated thermal donor. *ICDS18 proceedings of the 18th international conference on defects in semiconductors*, 196:849, 1995.

[20] S.M. Sze. *The physics of semiconductor devices*. John Wiley and Sons, 1969.

[21] Y.L. Huang, E. Simoen, C. Claeys, J.M. Rafi, R. Job, and W.R. Fahrner. Hydrogen-plasma-induced thermal donors in high resistivity n-type magnetic czochralski-grown silicon. *Applied physics letters*, 89:031911, 2006.

[22] T.M. Lifshits. Photothermal ionization spectroscopy of impurities in semiconductors. *Instruments and experimental techniques*, 36(1):1, 1993.

[23] A.K. Ramdas and S. Rodriguez. Spectroscopy of the solid-state analogues of the hydrogen atom: donors and acceptors in semiconductors. *Reports on progress in physics*, 44:1297, 1981.

[24] V.N. Abakumov, V.I. Perel, and I.N. Yassievich. Capture of carriers by attractive centers in semiconductors (review). *Soviet Physics semiconductors*, 12:1, 1978.

[25] P. Clauws, J. Broeckx, E. Rotsaert, and J. Vennik. Oscillator strength of shallow impurity spectra in germanium and silicon. *Physical review B*, 38(17):12377, 1988.

[26] P. Wagner and J. Hage. Thermal double donors in silicon. *Applied physics A*, 49:123, 1989.

Chapter 3

Hydrogen plasma treatments

3.1 Introduction

To introduce hydrogen in a controlled way in a semiconductor, mainly two methods are used in literature: plasma exposure and ion implantation. In the previous chapter, we have seen that direct-plasma exposure of oxygen containing silicon results in the introduction of hydrogen and the formation of shallow thermal donors. With regard to the relative simplicity of a direct-plasma (i.e. the sample is in direct contact with the glow-discharge) setup and the successful application of the method to silicon, the direct-plasma approach for hydrogenation of germanium was chosen here by using a home built instrument.

3.2 Experimental setup

Figure 3.1 shows a photograph taken from the plasma-setup. A diagram of the plasma reactor is shown in figure 3.2. Similar as in commercially available plasma-assisted deposition or etching reactors, the electrodes were put inside the chamber. The two electrodes are parallel and the bottom electrode will function as a sample holder. In between those two electrodes a glow-discharge will be created, which is called the plasma. The observable light purple color

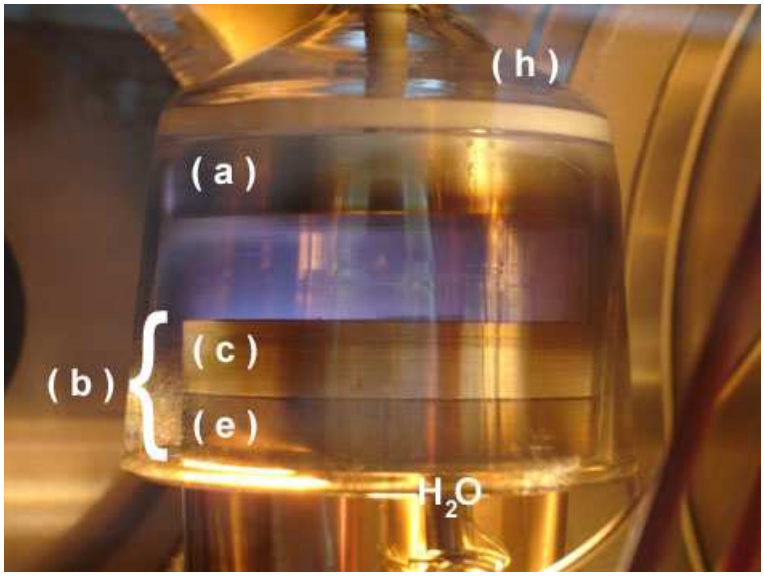

Figure 3.1: Photograph taken from the home-built plasma-setup

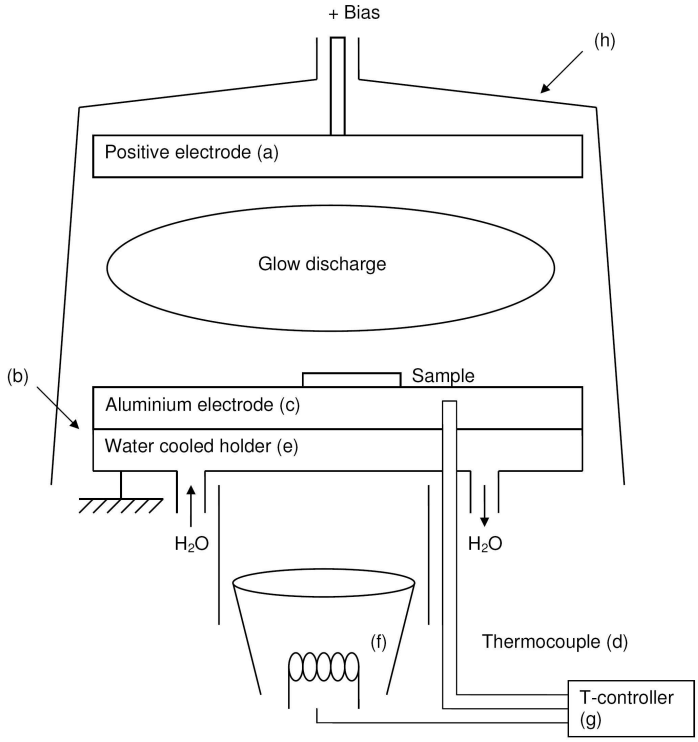

Figure 3.2: Diagram of the plasma-reactor

is due to the emission from the transition between electronic levels of the hydrogen molecules. This plasma consists of positive and negative ions, neutral atoms and molecules and radicals. The energy distribution and composition of the generated plasma is beyond the scope of this study. However we want to use this setup to introduce hydrogen in the sample, therefore the upper electrode (a) is connected to a power supply applying a positive potential and the lower electrode is grounded (b). Thus the fraction of positive ions are repelled from the upper electrode. Due to the fact that the bottom electrode is fixed at ground potential, it is technically more easy to use it as a sample holder that can be heated or cooled. The bottom electrode has two layers. The upper layer is an aluminium electrode (c) to create a homogeneous temperature distribution. The temperature can be measured with the thermocouple (d) inside the aluminium. The layer underneath (e) is a holder that can be cooled using a water flow. Thus water cooling can be used to decrease the sample temperature sufficiently fast after the treatment. Under this electrode an infrared source (f), (OSRAM 64625 HLX gold coated lamp) is installed as a heater. The infrared light is guided upward by a tube, to increase the intensity on the bottom of the lower electrode. The heater is connected to a temperature controller (g) (Eurotherm), which makes it possible to stabilize the temperature between 30℃ and 400℃. It may be noted that for the low temperature (<90℃) water cooling is needed because the sample will get heated by the plasma irradiation. Indeed at an electrical current density of $0.3 mA/cm^2$ a temperature of 90℃ was noticed without additional heating. To avoid discharge to the walls of the chamber the plasma region is shielded by means of a quartz funnel(h).

The plasma treatment is performed in a high vacuum chamber, which is ideal for this kind of research as sample contamination can be significantly reduced. Of course for industrial applications, this would increase the cost of the treatments too much. A pressure of $1.5 \times 10^{-8} mbar$ was reached in the vacuum system by a combination of a rotary and turbo molecular pump for the first

pumping cycle and an ion gettering pump for the second pumping cycle. Once this chamber has reached a pressure of $1.5 \times 10^{-8} mbar$ mbar it is filled with hydrogen gas H_2. No gas flow was used because this vacuum chamber is going to operate as a hydrogen reservoir during the plasma treatments. Describing the reservoir as a volume filled with an ideal gas at room temperature, one can calculate the total number of H_2 molecules. With the operating pressure of $6 \times 10^{-1} mbar$ and the volume of the vacuum chamber $\geq 2.3 \times 10^{-2} m^3$ this reservoir contains at least 3.3×10^{20} H_2 molecules. The diameter of the bottom electrode is $6cm$, this results in a maximum plasma treated surface area of $28.3cm^2$. Hydrogen concentration profiles observed in silicon after a plasma hydrogenation are typically lower than $10^{20} cm^{-3}$ within the first $10\mu m$ [1]. The total consumed hydrogen from the reservoir would thus be lower than 2.8×10^{16}. Comparing with the concentration of molecules in the reservoir one can expect no observable pressure changes (i.e. changes within the error of the pressure gauge), due to the introduction of hydrogen in the specimen.
Typical plasma parameters used in this study are a 1.2 kV voltage applied over the electrodes, a hydrogen gas pressure of $6 \times 10^{-1} mbar$, resulting in an electrical current of $0.3 mA/cm^2$. Due to the fact that the upper electrode can move, the electrode separation can be tuned, which makes it possible to treat samples using other electrical currents for the same gas pressure.

3.3 Test cases: the properties of plasma hydrogenated silicon

The hydrogen plasma reactor has first been tested on silicon samples, for which many results are available in the literature.

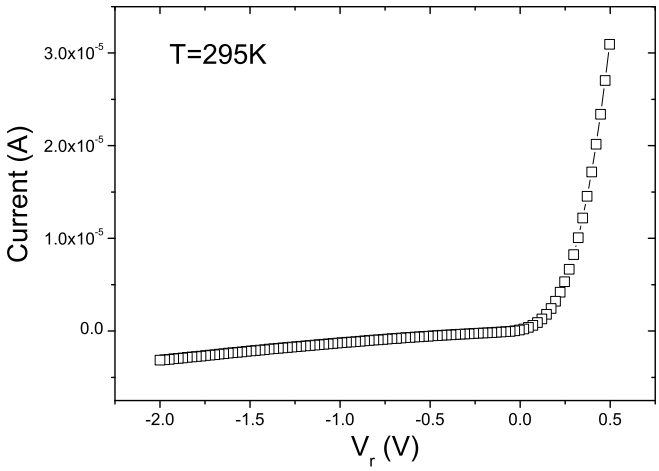

Figure 3.3: Current-Voltage plot curve for the formed pn-junction measured at room temperature

3.3.1 The formation of a np-junction

A first test is the formation of a n-type region due to the enhanced formation of donors in oxygen rich p-type silicon. P-type Cz-silicon was used as starting material with boron as shallow dopant and a resistivity of $1.8\Omega cm$. The interstitial oxygen concentration was $4 \times 10^{18} cm^{-3}$. Figure 3.3 shows the rectifying property of the pn-junction formed by means of a 5 hours 270℃ plasma ($0.3 mA/cm^2$) treatment. More details on the formation of donors by means of plasma hydrogenation have been given in the previous chapter.

3.3.2 The passivation of boron in silicon

A second check is the passivation of the electrical activity of the substitutional boron impurity. A boron doped p-type silicon sample with a resistivity of $18 m\Omega cm$ was treated in the plasma reactor for 5 hours at 150℃($0.3 mA/cm^2$). The optical reflection as a function of the wavenumber before and after the treatment is shown in figure 3.4. Before the treatment a resistivity of $18 m\Omega cm$

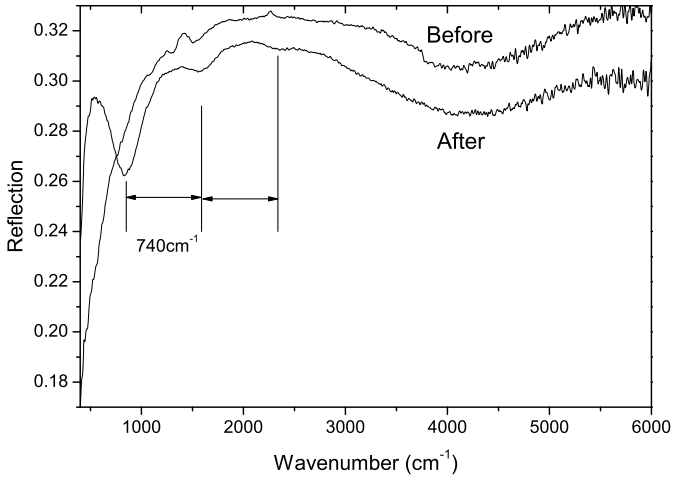

Figure 3.4: Optical reflection for a p-type silicon sample before and after plasma hydrogenation.

would mean $5 \times 10^{18} cm^{-3}$ free holes [2]. We use the equation:

$$\omega_P^2 = \frac{p_0 q^2}{m^* \epsilon} \tag{3.1}$$

for the plasma frequency for heavily doped semiconductors. Herein p_0 is the free hole density in the neutral semiconductor, q is the elementary charge, m^* is the effective mass and ϵ is the permittivity of the crystal. For p-type silicon with $p_0 = 5 \times 10^{18} cm^{-3}$, the plasma frequency is $260 cm^{-1}$. The minimum of the reflection corresponds with $\epsilon_R = \epsilon_\infty \left(1 - \frac{\omega_P^2}{\omega^2}\right) = 1$, which is shown in figure 3.5. The calculated minimum of the reflection is at $270 cm^{-1}$, which is below the measured middle infrared range of the spectrometer. This makes that before the treatment only the high frequency edge of the plasma onset of the reflection could be observed. After the treatment interference could be detected on top of the reflected signal, which is ascribed to a passivated layer. A diagram of the internal reflection in the passivated layer is shown in figure 3.6. The equidistant minima marked in figure 3.4 with a period of $740 cm^{-1}$, correspond with a passivated layer of $2\mu m$, which is in good agreement with

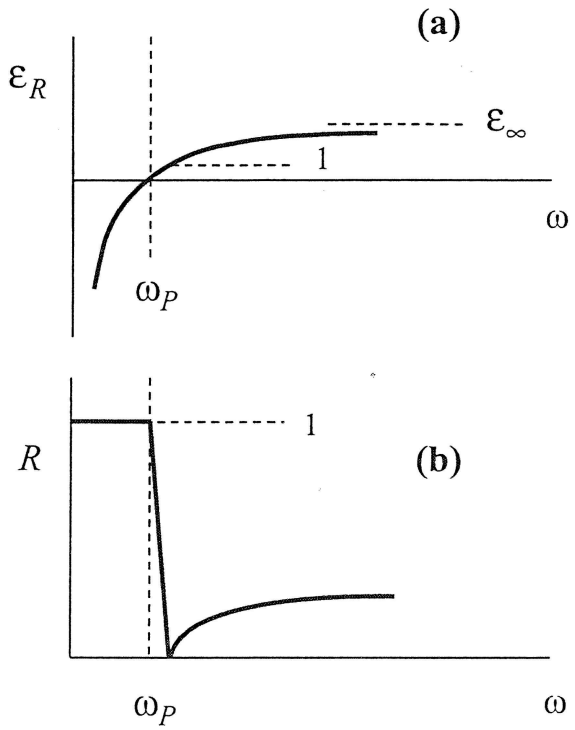

Figure 3.5: Dielectric constant (a) and reflection spectrum (b) from free carriers in a semiconductor (figure taken from reference [3])

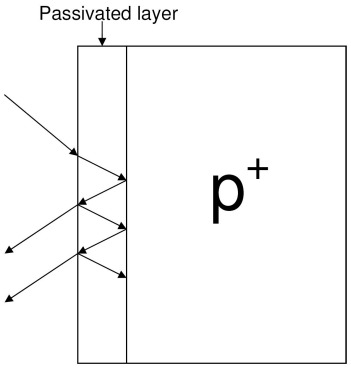

Figure 3.6: Diagram of the internal reflection in the passivated layer.

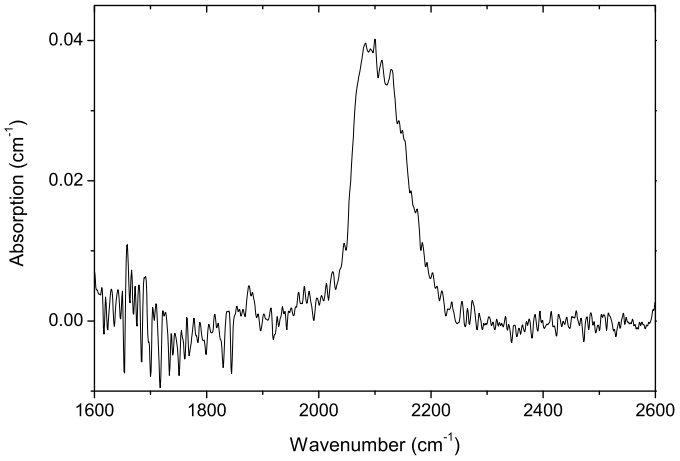

Figure 3.7: Absorption spectrum of plasma treated silicon showing the Si-H vibrational mode

the passivated depth for boron acceptors reported in reference [1].

3.3.3 Hydrogen related platelets

As a last check we want to create hydrogen related platelets[1]. Johnson et al. [4] observed these defects by means of Transmission Electron Microscopy and correlated the presence of these hydrogen related extended defects to different spectroscopic observations. Figure 3.7 shows the absorption spectrum of silicon after 2.5 hours hydrogenation at 150℃. Herein the Si-H vibrational band, which was ascribed to hydrogen bonds within a plate-like extended structure, could be observed. It may be noted that no additional absorption due to the introduction of contamination could be observed within the mid-infrared range (i.e. $400cm^{-1} - 4000cm^{-1}$).

[1] More details on hydrogen related platelets is given in chapter 4

3.4 Conclusions

A direct plasma reactor was built, which makes it possible to introduce hydrogen in silicon at a chosen stabilized temperature. Different known properties of hydrogen in silicon were tested using this new setup. It could be concluded that due to the high vacuum chamber, the presence of contamination is reduced and thus this configuration is ideal as an experimental tool in the research to the properties of hydrogen in other materials like for example germanium.

Bibliography

[1] S.J. Pearton, J.W. Corbett, and M. Stavola. *Hydrogen in crystalline semiconductors.* Springer, 1991.

[2] S.M. Sze. *The physics of semiconductor devices.* John Wiley and Sons, 1969.

[3] P. Clauws. *Vaste-stoffysica en halfgeleiders.* Syllabus Universiteit Gent, 2004-2005.

[4] N.M. Johnson, F.A. Ponce, R.A. Street, and R.J. Nemanich. Defects in single-crystal silicon induced by hydrogenation. *Physical review B*, 35(8):4166, 1987.

Chapter 4

Hydrogen plasma treated germanium

4.1 Hydrogen in germanium

High purity germanium crystals are usually grown in hydrogen ambient, for protection of the material from oxidation, as a heat transfer medium and to passivate trapping centres (see e.g. chapter 6). In this way the quest for ultra-pure germanium for radiation detectors has driven the early research on hydrogen-related defects. According to the experiments of Frank and Thomas [1] near the melting point the hydrogen solubility amounts to $4 \times 10^{14} cm^{-3}$. A recent review on hydrogen in germanium was given by Weber et al. [2].
Due to the fact that silicon and germanium have similar properties, in general one would not expect qualitative differences in the behavior of H between the two semiconductors. Also the chemistry of Si-H and Ge-H compounds is very similar. However Estreicher and Maric [3] noted that whenever identical experiments involving H are done on comparable Si and Ge samples, the results are very different, and thus one can conclude that qualitative differences do exist. Below the observed differences are summarized:

- From thermal effusion experiments using Si and Ge exposed to a 20h

deuterium plasma at different plasma temperature (T_{pl}), one observed that the total amount of D extracted from Si increases with T_{pl}, while it decreases with T_{pl} for Ge.

- No dopant passivation is observed in Ge under conditions that lead to almost complete passivation in Si.
- In high-purity samples at low temperature injected with muons, one could conclude that in Si a third of the incoming muons manage to force their way into their most stable state at the bond center (BC) site. For Ge only 8% reaches the BC site, even though the Ge-Ge bond is longer and weaker, from which one should expect that the expansion needed is easier to accomplish. Muonium (μ^+, e^-) can be interpreted as the light pseudoisotope of hydrogen with a mass $\frac{m_H}{9}$.
- PTIS measurements of high-purity Ge grown under a hydrogen ambient show that the electrically inactive species carbon, silicon and oxygen becomes electrically active after forming a complex with H.

Due to these observed differences Estreicher and Maric [3] expected a qualitative difference between H in Si and Ge. From ab initio calculation they concluded comparing the formation energy of H_{BC} (H at the relaxed BC site) to H_T (H at the T site), that for silicon the H_T is the most stable while for Ge the H_{BC} configuration is the most stable. The main conclusion is that H^+ is very abundant in Si, which results in the passivation of acceptor levels. The absence of very high H^+ concentrations in Ge reduces the capture cross-section for passivation of negatively charged acceptors. Also due to the fact that almost all H are found at the T-site in the neutral configuration the formation of the hydrogen molecule ($H^0 + H^0 \rightarrow H_2$) is more probable. At higher temperatures these H^0 are more mobile and the immobile H_2 concentration increases, which prevents the further indiffusion of H.
Different results were observed by Van de Walle et al. [4]. Using DFT-calculations they conclude on a universal alignment of hydrogen in semiconductors, insulators and solutions. And thus it is found that H^+_{BC} is the stable

state in p-type, while H_T^- is the most stable state in n-type.
The purpose of this chapter is to characterize the different defects created in germanium after hydrogenation. Comparing to silicon less is known about the effect of hydrogen plasma treatments on germanium. However the formation of hydrogen related defects has become an interesting topic due to the discovery of layer transfer, which is discussed in the next paragraph. Structural characterization techniques as TEM and Positron Annihilation Spectroscopy are used to study the formed plate-like structures, which mediate the blister formation observable on the surface. Until now only Raman Spectroscopy [5] has confirmed the presence of hydrogen in these structures, therefore Infrared Absorption Spectroscopy is used here to identify the infrared active counterpart of the vibrational modes. The effect of a hydrogenation on the electrical properties of the germanium is studied by means of DLTS measurements. Finally also the formation of shallow donors in hydrogenated oxygen containing germanium is explored by means of PTIS measurements.

4.2 Hydrogen related plate-like structures

Silicon on insulator (SOI) technology has substantial advantages over traditional bulk Si processing for a wide range of Ultra Large Scale Integration (ULSI) applications. A very attractive technique for fabricating high-quality SOI systems was developed by Bruel et al. [6] at LETI based on skillful hydrogen implantation and wafer bonding. This Smart-Cut process (which is a registered trade mark of SOITEC) consists of four main steps shown in figure 4.1. The different steps involved in the Smart-Cut process are summarized by Feng and Huang [7]:

- A wafer A capped with a dielectric layer (e.g. thermally grown SiO_2) is exposed to hydrogen implantation at room temperature with a dose in the range 3.5×10^{16} to $1.0 \times 10^{17} cm^2$ in order to introduce a thin layer with hydrogen ions of sufficiently high density.

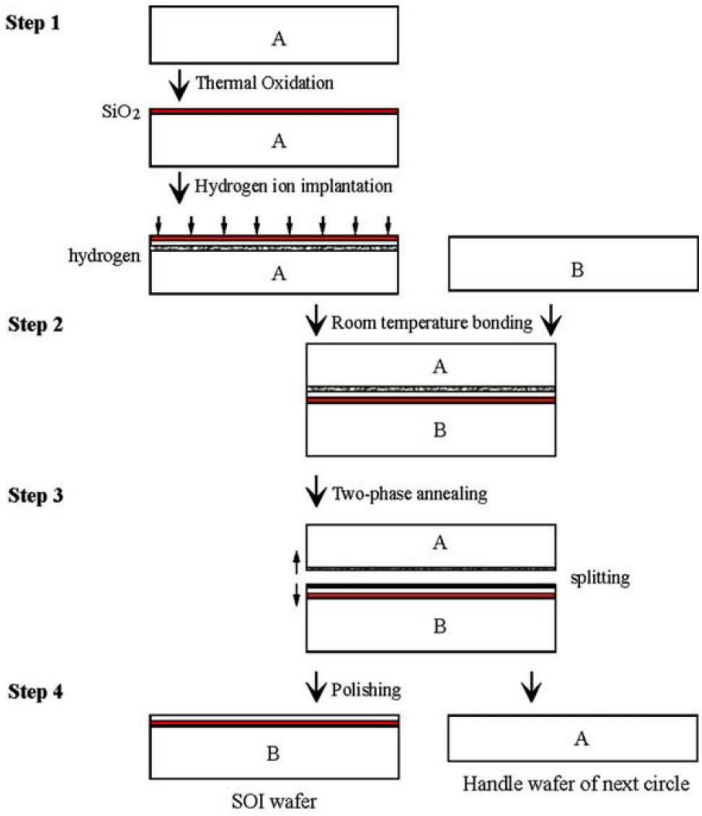

Figure 4.1: Schematic of the Smart-Cut process (figure taken from [7])

- The second step consists of chemical cleaning and hydrophilic bonding at room temperature of wafer A to a handle wafer B by van der Waals forces. The handle wafer serves as a stiffener and provides the bulk silicon beneath the buried SiO_2 in the final SOI structure.

- The third step consists of splitting and annealing of the two bonded wafers including two stages of heating, a medium-temperature stage (400 600 ℃) and a high-temperature stage (about 1100℃). During the first stage, a thin damaged layer appears at the depth of the maximum hydrogen ion concentration in the implanted wafer A, which splits into two parts yielding a SOI structure and the remainder of wafer A. The subsequent high-temperature thermal treatment removes radiation defects in the silicon layer and strengthens the chemical bonds between the two wafers.

- The top silicon layer is polished by a chemical-mechanical method to obtain a high-quality surface. Thus, as a result of the process, an SOI wafer and a residual wafer A are obtained, and the latter can be used again as a handle wafer.

Due to the technological importance of Ge as a material with a significantly higher carrier mobility, germanium on insulator becomes a good candidate as a substrate for electronic applications. In combination with the discovery of the semiconductor layer transfer using hydrogen implantation the formation of hydrogen related defects in germanium has recently become an interesting topic. Hereby it was shown that plate-like hydrogen clusters are the important defects mediating layer transfer for silicon [8]. Recently also GeOI (Germanium on insulator) structures produced by Smart Cut technology attracted significant interest [9]. With Transmission Electron Microscopy (TEM) Akatsu et al. [10] observed in Ge the defect structures within this heavily damaged region due to the ion implantation and additional annealing. The majority of the observed defects were platelets (plate-like structures) in the {100} plane, parallel to the implanted surface. The platelets in the {111} planes are detected at

the deeper side of the implanted zone. And also some extended structure in the {311} planes are observed. In sharp contrast with Si, a large density of spherical nano cavities of 1-2nm in diameter are observed randomly distributed in the damaged region. Some nanocavities are aligned in micro cracks. This might indicate that the individual micro cracks in Ge may grow by propagation through nanocavities.
Recently David et al. [11] showed by means of TEM that for implantation at room temperature small {001} and {111} platelets and {311} defects are nucleated while for higher substrate temperatures, micro cracks, cavities and plate-like cavity clusters are formed as well.

4.3 Experimental

The germanium samples used in this study were different Cz (100) wafers from Umicore. The hydrogen has been introduced using the direct plasma system discussed in the previous chapter. Different hydrogenation temperatures, electrical current densities and treatment times were used. The choice of parameters was made to allow the introduction of high concentrations of hydrogen in the crystal without direct formation of blistering or observable radiation damage on the treated surface. In the following paragraph the effect of high doses and the effect of an additional annealing step are treated first. Later the experimental observation after the different treatments with no observable damage on the surface will be discussed. More details on the samples and the treatment as a function of the characterization technique will be given in the different sections of the text below.

4.4 Structural Characterization

4.4.1 Blisters on the surface

In absence of the right wafer splitting parameters or a support wafer, similar plate-like extended defects could still be formed due to the high hydrogen concentrations and form observable blisters on the treated surface. Two types of treatments will be discussed below, which resulted in a blistering Ge surface. First a high dose plasma treatment of 16h at 150℃ with a current density of $0.5mA.cm^{-2}$ was applied. Due to this long plasma exposure a blistering surface was observed directly after the plasma treatment. Figure 4.2 shows a detail of the popped up circular surface blisters observed with Scanning Electron Microscopy (SEM).

For blisters one mostly assumes that, due to the high plasma dose, nucleation appears close to the surface and probably the size of the blisters (Radius R) is larger than the depth of the platelets below the surface (h). The germanium crystal above the platelet parallel to the surface can then be approximated as a circular plate with radius (R) and thickness (h) (see figure 4.3) One can then assume that the critical size of the blisters corresponds with the radius when the surface energy equals the strain energy in the plate. Therefore we can use the formula for the critical radius for blistering (see reference [12]):

$$r_{\text{crit}} = \left(\frac{16\gamma_p E h^3}{3\alpha \left(1-\nu^2\right) \Delta P^2} \right)^{\frac{1}{4}} \tag{4.1}$$

with E the Young modulus, ν the Poisson ratio, h the depth of the platelet from the surface, γ_p the surface energy, α a numerical factor (in the order of ≈ 1 depending on the details of the calculations) and ΔP the difference between the pressure inside the platelets and that of the outside atmosphere. It should be noted that this γ_p is associated with the interaction between the hydrogen-covered surfaces of the platelets. Reasonably it can be assumed that γ_p is lower than the surface energy γ_{Ge} (i.e. the surface energy corresponding with crystal planes of germanium). We assume that $\gamma_p = 0.5J.m^{-2}$ and $\Delta P = 10^9 Pa$, which is equal to the value for silicon assumed by Huang et al.

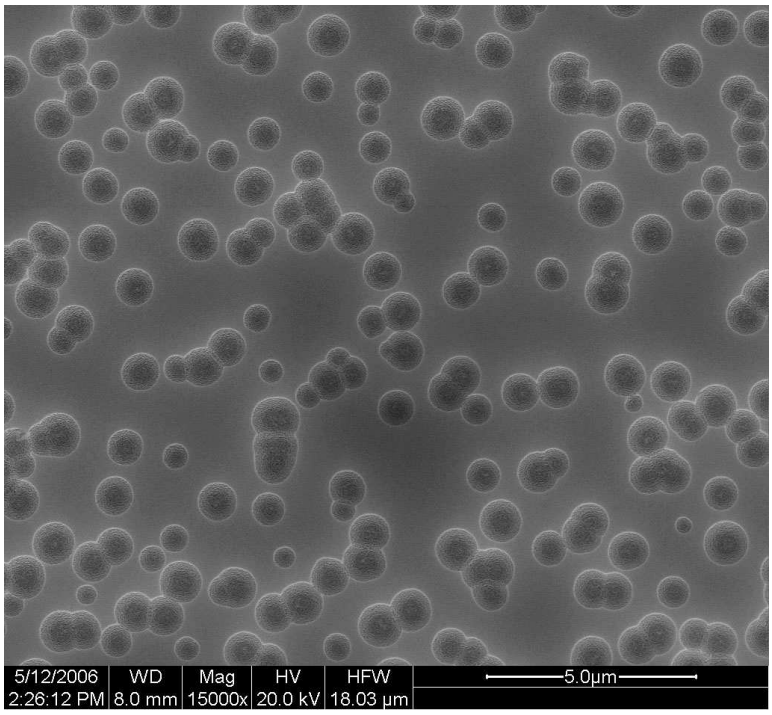

Figure 4.2: SEM image of the germanium surface, after 16h hydrogen plasma treatment at 150℃ with a current density of $0.5mA.cm^{-2}$.

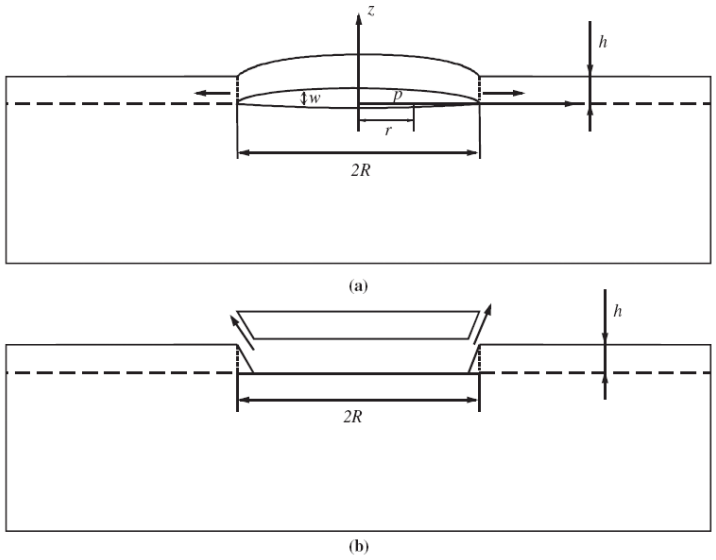

Figure 4.3: (a) Planar growth of a sub-surface crack and(b) its flaking (Figure taken from Feng et al. [7])

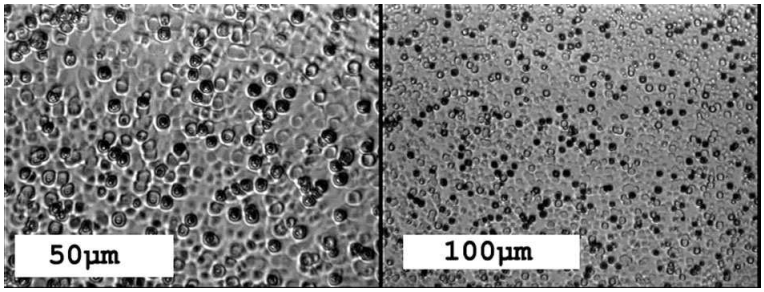

Figure 4.4: Optical microscope image of the blistered germanium (100) surface after plasma treatment (observed for both 150℃ and 250℃ $0.3mA.cm^{-2}$) and additional 2h 600℃ annealing in an argon-gas flow.

[12]. For the mechanical parameters of the $< 100 >$ direction of germanium we use: $\nu = 0.26$ and $E = 1.03 \times 10^{11} Pa$. From the radius of the observed blisters $r_{\text{crit}} = 250nm$ one can then calculate the approximate depth of the platelets as $h = 0.24\mu m$. It will be shown later that this depth is in agreement with the observed extended defects.

A second method to create a blistering surface is first start with a low dose (i.e. 4h $0.3mA.cm^{-2}$) and expose the sample to an additional anneal. Figure 4.4 shows a typical optical microscope image of the blistering surface observed for samples hydrogenated at 150℃ after 2h 600℃ anneal. Similar blisters could be observed for a preceding hydrogenation with a sample temperature of 250℃. In the case of a lower current plasma treatment no damage could be observed on the surface before the additional anneal. It suggests that although no direct blistering was observed with the plasma parameters used here (lower dose), a part of the introduced hydrogen has nucleated in hydrogen platelike structures. Due to the additional annealing one can assume that those clusters grow and the molecular hydrogen gas pressure increases inside the clusters, which results in the flaking (see figure 4.3 b) of the surface without increasing the total hydrogen concentration in the sample. For the size of those blisters $r_{\text{crit}} = 1.5\mu m$, the depth calculated using equation (4.1) is about $2.6\mu m$. Although the demand $h < r_{crit}$ for equation (4.1) is not fulfilled one

can assume that the platelets are formed more deeply into the bulk comparing to the high dose treatment.

4.4.2 Transmission Electron Microscopy

To observe the defects that are responsible for the observed blisters on the surface, Transmission Electron Microscopy (TEM) was performed on a Ge crystal before and after plasma treatment at 150℃ for 2.5h ($0.5mA/cm^2$). It should be noted that due to the shorter treatment (2.5h instead of 16h) comparing to the sample discussed in the previous paragraph no blisters were observable on the surface.
The TEM experiments have been made using a JEOL 200 CX microscope at the University of Poitiers (France). Those measurements have shown that due to the plasma hydrogenation a damaged region containing defects extends from the surface to a maximum depth of $1.1\mu m$. The first 70nm from the surface is a highly damaged region which can be seen in the very dark contrast (see figure 4.5. Figure 4.6 a shows the platelets of about 30nm long inside this region. They are located in {100} and {111} planes, as in the case of H implantation or plasma immersion in Si [13] and Ge [10]. Figure 4.5 shows defects presenting a strong deformation (ring) contrast (in two beam conditions) located between 70 nm and 1100 nm from the surface. As seen in the magnification of figure 4.5 tiny cavities, between 2 and 5 nm in diameter, are observed inside the deformation contrast. From the circular shape of the deformation contrast, we can deduce that some of the plate-like structures, labeled A in figure 4.5, are located in the {110} planes. However, some of them are observed edge-on, labeled B in figure 4.5. They are probably in the {111} planes. The presence of cavities is confirmed by the Fresnel fringes observed around the cavities in under- and over focus conditions (Figure 4.6 b and c). The cavities are arranged in clusters forming plate-like structures (i.e. they are located in a plane) giving rise to the deformation contrast seen in figure 4.5. Dimensions lie between 40 and 70 nm in diameter, the smaller ones being closest to the surface. These dilute cavity systems have also been observed in He implanted

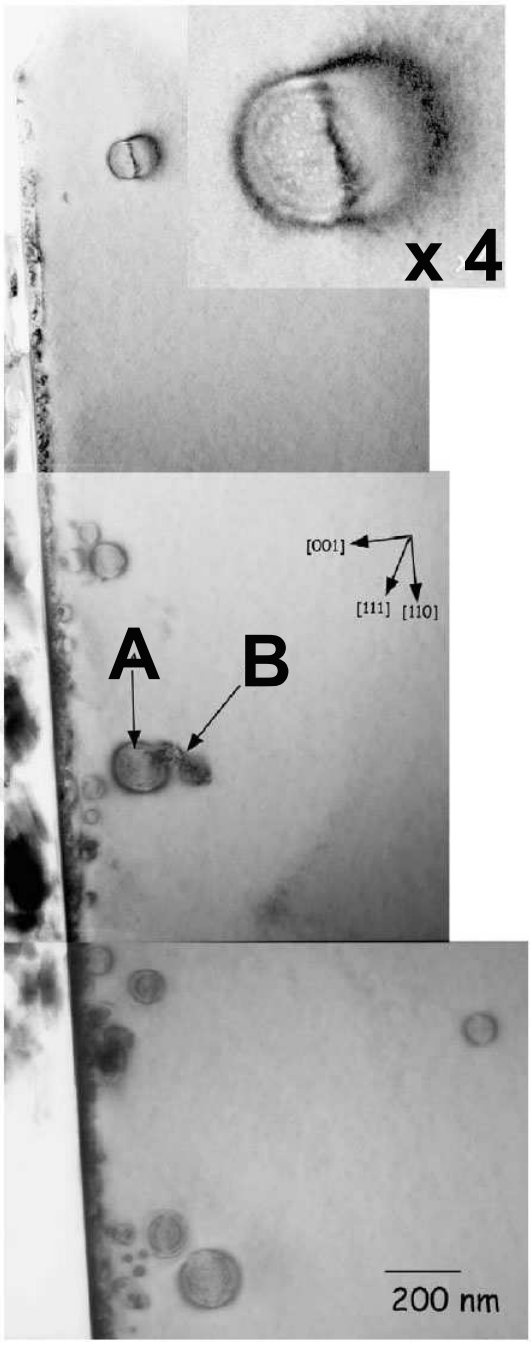

Figure 4.5: High magnification TEM image of the sample treated for 2.5h at 150℃ $(0.5mA.cm^{-2})$ in two beam conditions.

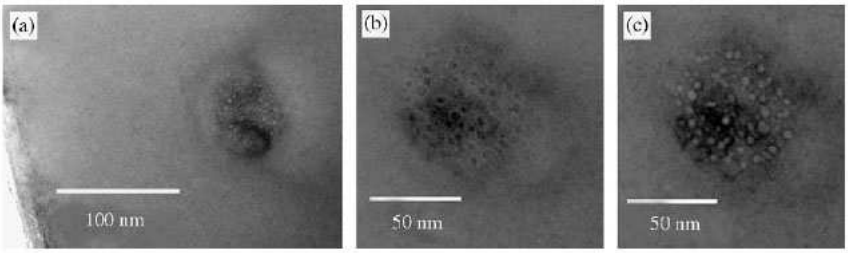

Figure 4.6: (a) Bright field TEM image of a plate-like structure and the platelets and cavities close to the surface. (b)(c) Plate-like cluster of cavities in under focus and over focus conditions

Si samples with a dose of $1 \times 10^{16} cm^{-2}$ and an energy of 40 keV [14, 15].

4.4.3 Positron annihilation Spectroscopy

The open volume defects created in the Ge crystal are studied by means of Positron annihilation measurements. N-type Ge wafers with an Sb concentration of $5 \times 10^{13} cm^{-3}$ were used. This low dopant concentration was chosen to minimize the influence on the positron annihilation measurements. Positron annihilation measurements were made at the Ghent slow positron facility [16]. The positrons can be implanted in the sample with an energy from 200 eV up to 30 keV, resulting in an average implantation depth of maximum 1.7 μm in Ge. For a slow positron experiment the implantation depth profile for different energies can be calculated using a Makhov profile using the density of the germanium ($5.35 g/cm^3$). The resolution of the Ge detector used for the Doppler broadening experiments is 1.14 keV at 514 keV. The Doppler broadened annihilation line was characterized using the well known S and W parameters. The S-parameter (Shape) represents the fraction of photons with an energy $511keV - E_s$ and $511keV + E_s$, while the W-parameter (Width) equals the fraction of photons in the sides of the Doppler peak. The S-parameter can be interpreted as the valence electron contribution to the annihilation and the W-parameter stands for the core electron contribution. In an open volume defect more valence electron contributions should be expected. This means that the

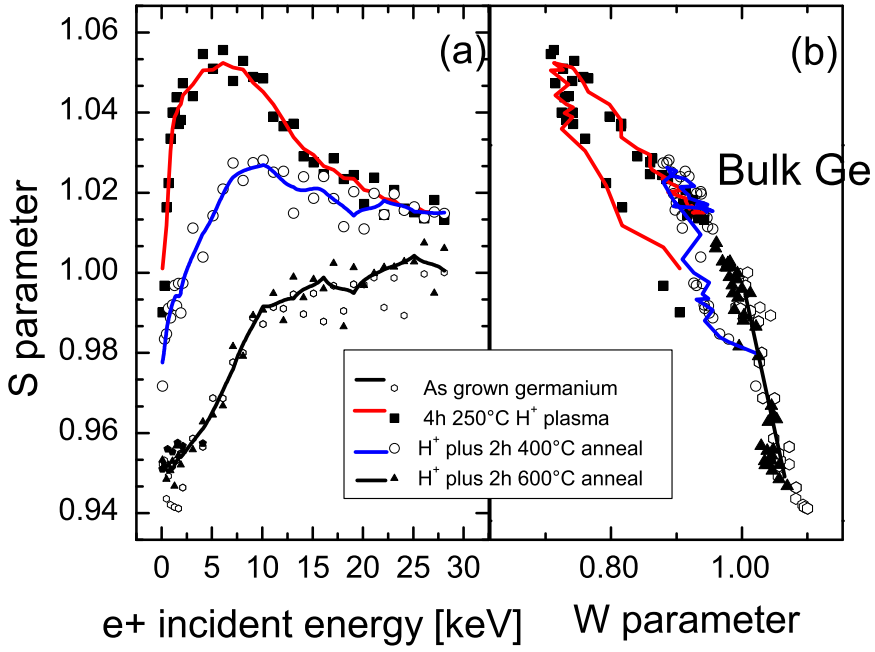

Figure 4.7: Evolution of the normalized line shape parameter S as a function of the positron incident energy and the evolution in the (S,W) representation for the samples hydrogenated at 250℃, after an additional anneal at 400℃ for 2h and at 600℃ for 2h.

material-specific S and W parameters change to a larger S and a smaller W due to the annihilation in the open volume.

Figure 4.7 shows the evolution of the normalized line shape parameter S as a function of the kinetic energy of the positron and the corresponding evolution in the (S,W) representation for the sample hydrogenated at 250℃ and after different annealing steps. In figure 4.7 a it can be seen that the S-parameter starts from a surface state and converges for larger positron energies to a S-parameter that corresponds with bulk defect free germanium. For the W-parameter a similar trend can be observed. Thus for the defect free germanium,

Modified layer	S	L (nm)	Thickness (nm)
Hydrogenated 250℃	0.566	80±10	300±20
Annealed 400℃ 2h	0.566	155±10	300±20
Annealed 600℃ 2h	0.538	235 ±10	-

Table 4.1: Overview of the fitted parameters using VEPFIT.

for every positron energy the (S, W)-couple can be written as a linear combination of the (S, W) of annihilation at the surface and (S, W) of annihilation in the bulk. Both the red curve (sample 4h 250℃ H^+ plasma) and blue curve (sample 4h 250℃ H^+ plasma + 2h 400℃anneal) start for low positron energies with a different surface (S, W)-couple and converge to the bulk germanium (S, W)-values. In between (i.e. e^+ incident energies of $\approx 10keV$ the S-parameter is higher and the W-parameter is lower. Thus one can assume that a fraction of the positrons annihilate in the defect rich layer.
VEPFIT analyses the depth selective measurements using a 1 dimensional diffusion equation. The positron diffusion length (L) can be calculated using:

$$L = \sqrt{D\tau_{eff}} = \sqrt{\frac{D}{\frac{1}{\tau_{eff}} + \mu_t C_t}} \tag{4.2}$$

where D is the diffusion constant, τ_{free} is the bulk life time, C_t the trap concentration and μ_t the trapping efficiency. Thus the diffusion length provides info about defect concentrations. The results of the VEPFIT analysis of these samples are summarized in table 4.1. The bulk positron lifetime of the substrate before hydrogenation was 228 ps corresponding to the defect free lifetime. The positron diffusion length (L) was measured on these defect free samples by depth selective Doppler Broadening experiments and calculated using the VEPFIT [17] software to be $235 \pm 10nm$. Using a box shaped defect profile in the VEPFIT routine for the sample hydrogenated at 250℃ a thickness of the region influenced by the hydrogenation of approximately 300nm was calculated (thickness in table 4.1). While the defect free bulk S parameter value for Ge is $S_B = 0.538$, the S parameter value of the defects in this damaged layer is $S_D = 0.566$. These defects have hence a normalized S parameter of S=1.044.

The increase in S-parameter and decrease in W-parameter can thus be interpreted as an annihilation in an open volume defect. It was shown in the case of silicon that a defect with such a signature corresponds to a vacancy cluster V_n with $n \geq 3$ [18]. A reasonable fit on the 400℃ annealed samples was only feasible by fixing the S value of the modified layer to 0.566 and hence assuming that the same type of defect is present after annealing. Fixing only this value the VEPFIT results indicated that the width of the modified layer does not change by the 400℃ anneal but the diffusion length of the positrons increases from 80nm to 150nm, indicating a reduction of the total concentration of open volume defects by a factor of 6. After a final anneal of 600℃ the positron diffusion length and S parameter coincide again with those of the virgin defect free sample.

4.5 Vibrational mode spectroscopy

Due to the very low concentration of hydrogen within a thin germanium layer close to the treated surface, the total number of hydrogen related complexes within the optical path of the beam in infrared absorption spectroscopy is small (i.e. close to the detection limit of absorption spectroscopy). This might be the reason that until now no absorption spectrum was detected of hydrogen related defects in Ge after plasma treatments. Only Raman spectroscopy [5] measurements have confirmed until now the introduction of hydrogen and the formation of $Ge - H$ bonds due to plasma treatments in germanium.

A typical absorption spectrum recorded at room temperature for plasma treated germanium is shown in figure 4.8. The phonon absorption was subtracted from the spectrum. It should be noted that the strong phonon absorption in the region of the wag mode makes that this absorption band is less accurately determined. Absorption spectra were calculated from the transmission taking account of multiple reflection between the parallel surfaces of the sample.

After a plasma treatment at 150℃ for 2.5h two broad absorption bands could

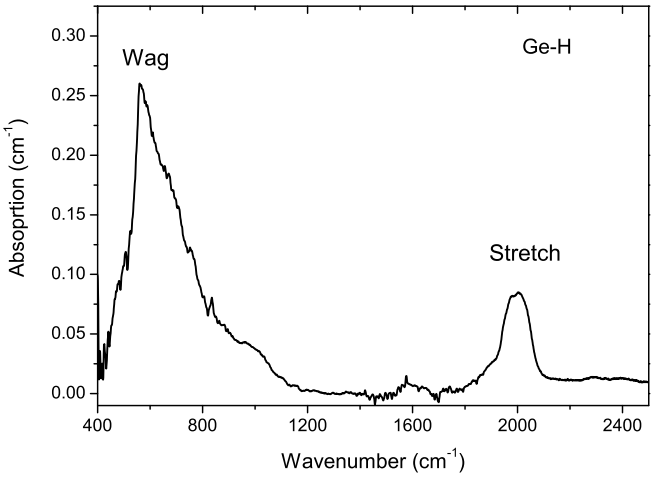

Figure 4.8: Room temperature absorption spectrum of the plasma hydrogenated p-type Ge sample (plasma temperature 150℃, duration 2.5 hours) with an unapodized resolution of $4cm^{-1}$. The phonon absorption of germanium has been removed by subtracting the absorption of an untreated sample.

be observed, one at lower wavenumber with a maximum at $630cm^{-1}$ and another one at higher wavenumber at $1980cm^{-1}$. Both absorption bands are absent after a short etch in HNO_3 : HF or after mechanical removal of the first $\approx 2\mu m$, showing that the signal originates from defects close to the surface. Due to the similarity with the absorption spectrum of amorphous-Ge (a-Ge), the two broad bands located at $630cm^{-1}$ and $1980cm^{-1}$ can be assigned to the wag and stretch-mode of Ge-H bonds respectively.
The absorption of a-Ge (and a-Si) was reviewed by Cardona [19]. The GeH_n related compounds were described in terms of a valence force field. A stretch-stretch force constant f_{DD} is defined for $Ge-H$ and bond bending constants f_{AA} and f_{BB} for $H-Ge-H$ and $H-Ge-Ge$ bonds respectively. For simplicity the bond bending forces are set equal $f_{AA} \approx f_{BB}$. All other cross-coupling force constants such as stretch-bend and bend-bend are set negligible. Starting to describe the germane molecule GeH_4 using this model one can calculate the four vibrational frequencies (ω_i) (shown in figure 4.9 a) as a function of the force constants:

$$\begin{aligned} m\omega_1^2 &= f_{DD} \\ m\omega_2^2 &= 3f_{AA} \\ m\left(\omega_3^2+\omega_4^2\right) &= f_{DD}\left(1+\frac{4m}{3M}\right)+2f_{AA}\left(1+\frac{8m}{3M}\right) \\ m\omega_3^2\omega_4^2 &= 2f_{DD}f_{AA}\left(1+\frac{4m}{M}\right) \end{aligned} \tag{4.3}$$

with m the mass of the hydrogen atom and M the mass of the germanium atom. It may be noted that for $m << M$ the formulae for ω_3 and ω_4 reduce to $m\omega_3^2 = f_{DD}$ and $m\omega_4^2 = 2f_{AA}$. From the observed frequency for the bend E and stretch A_1 mode of the germane molecule: $2120cm^{-1}$ and $931cm^{-1}$ respectively, one can calculate the force constants for the Ge-H system using equation (4.3):

$$\begin{aligned} f_{DD} &= 2.67 \times 10^2 N/m \\ f_{AA} &= 1.71 \times 10^1 N/m \end{aligned} \tag{4.4}$$

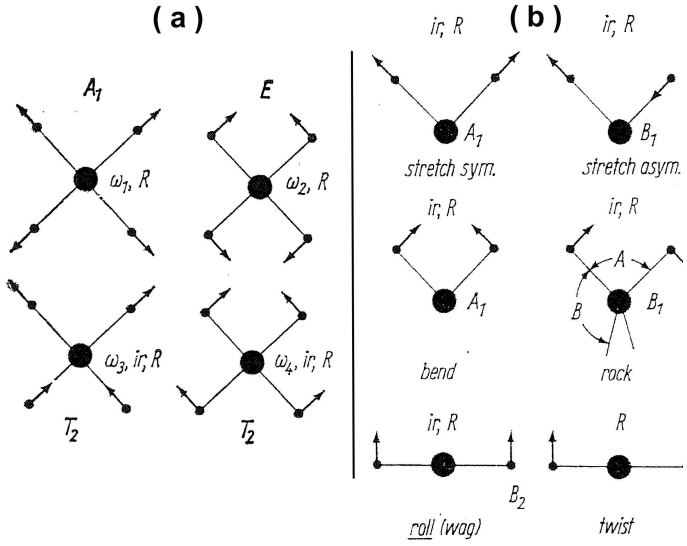

Figure 4.9: (a) Schematic diagram of the four vibrational modes of GeH_4 assuming $M >> m$. The figure represents the projection on a 100 plane with the bonds along the <111> directions. (b) Schematic diagram of the vibrations of GeH_2 radicals.

To evaluate the stretching mode for the Ge-H bond one can extrapolate the value for the germane molecule using the observed stretching frequency for the GeH_2 molecule at $2036cm^{-1}$. In this way one can calculate the stretch vibrational frequencies $2078cm^{-1}$ and $1994cm^{-1}$ for GeH_3 and GeH respectively. Values for the frequencies are summarized in table 4.2. For the angular modes of the GeH_2 molecules one can assume that the bend A_1 can be obtained as a linear combination of the E and T_2 mode of the germane molecule:

$$|A_1\rangle_{GeH_2} = \frac{1}{\sqrt{2}}\left(|E\rangle_{GeH_4} + |T_2\rangle_{GeH_4}\right) \tag{4.5}$$

Hence for $m << M$ one can obtain:

$$m\omega^2(A_1) = 2f_{AA} + \frac{1}{2}f_{BB} \approx \frac{5}{2}f_{AA} \tag{4.6}$$

Using the force constant f_{AA} from equation (4.4) one can calculate the frequency for the A_1 bend mode of GeH_2 $\omega(A_1) = 850cm^{-1}$.
Similar calculations can be made for the B_2 (roll) and A_2 (twist) modes considering them degenerate. The A-angle shown in figure 4.9 b between the

	cm^{-1}		
GeH	stretch	wag	
	1994	658	
GeH_2	stretch A_1, B_1	roll B_2	bend A_1
	<u>2036</u>	658	850
GeH_3	stretch		
	2078		
GeH_4	stretch A_1		bend E
	<u>2120</u>		<u>931</u>

Table 4.2: Vibrational frequencies (in cm^{-1}) of Ge-H bands deduced as discussed in the text (experimental values to calibrate are underlined)

$H-Ge-H$ bonds varies only quadratically with the atomic displacements of these modes and hence the frequencies of these modes are the same as if only one atom would move. Thus the frequency of the vibration of one $Ge-H$ bond is easily obtained from the equation 4.6 by dividing the f_{AA} contribution by two and thus in this model:

$$m\omega^2(B_2)_{GeH_2} = m\omega^2(A_2)_{GeH_2} = m\omega^2(\text{wag})_{GeH} \approx f_{AA} + \frac{1}{2}f_{BB} = \frac{3}{2}f_{AA} \tag{4.7}$$

From this one can calculate $658cm^{-1}$ for the wag mode of the $Ge-H$ bond. The different modes and frequencies calculated from the force constants are summarized in table 4.2. Comparing the absorption spectrum with the modes calculated using the method of Cardona [19], one can conclude that the bands can be interpreted as the wag mode and stretch mode of $Ge-H$ bonds (shown in figure 4.10).

Recently the $1980cm^{-1}$ stretching mode was observed by means of Raman spectroscopy of plasma treated germanium [5]. Polarization sensitive Raman measurements show that the plasma treatment results in the formation of hydrogen induced platelets oriented along {111} crystallographic planes. The $Ge-H$ mode at $1980cm^{-1}$ corresponds with $Ge-H$ bonds in the platelets

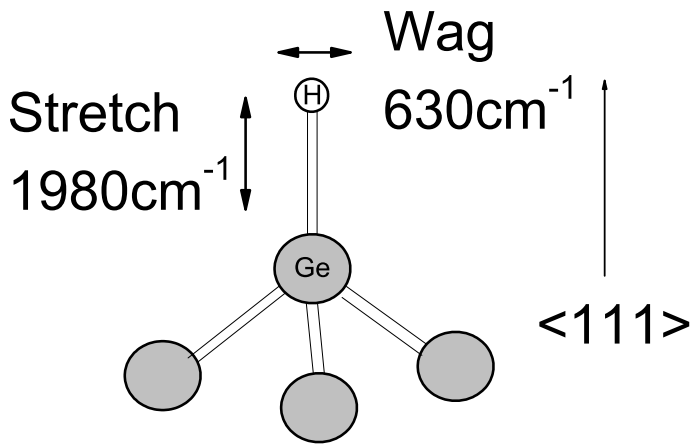

Figure 4.10: Molecular model showing the stretch and wag mode in a classical interpretation.

directed along the {111}, while a mode observed at $4150cm^{-1}$ belongs to molecular H_2 within the platelets.

Hourahine et al. [20] have calculated the vibrational modes of platelets and the molecules inside. Table 4.3 shows the vibrational modes of a few structures. A model for the atomic structure of the platelets is shown in figure 4.11. The molecule containing platelets posses modes at around $4120cm^{-1}$, with the frequency increasing as a second molecule is added. There are two bands of GeH related modes in these structures, and again increasing the number of hydrogen molecules pushes these upwards by $\approx 50cm^{-1}$. This then suggests that the width of the bands observed at 1980 and $4155cm^{-1}$ may in part be due to a range of concentrations of hydrogen molecules in different platelets. Similar bands have also been detected in plasma treated silicon [22, 23], see also chapter 3.

Figure 4.12 shows the Raman spectrum of the same hydrogenated sample as for the infrared spectrum in figure 4.8. Two bands are observed, one with a maximum at $1980cm^{-1}$ and one at $4150cm^{-1}$. The two bands correspond with the ones observed by Hiller et al. [5] and thus it is concluded that they belong to stretching modes of the $Ge-H$ and H_2 species in the {111} platelet.

	cm^{-1}
$2\mathrm{Ge}-\mathrm{H}$	1966
	1886
$2\mathrm{Ge}-\mathrm{H}+\mathrm{H}_2$	4111
	1984
	1882
$2\mathrm{Ge}-\mathrm{H}+2\mathrm{H}_2$	4146
	2025
	1956

Table 4.3: Average vibrational frequencies of hydrogen related platelets as calculated by Hourahine et al. [20]. $2Ge-H$ means a double layer of $Ge-H$ bonds as shown in figure 4.11; nH_2 indicates the number of H_2 molecules for each $2Ge-H$ couple.

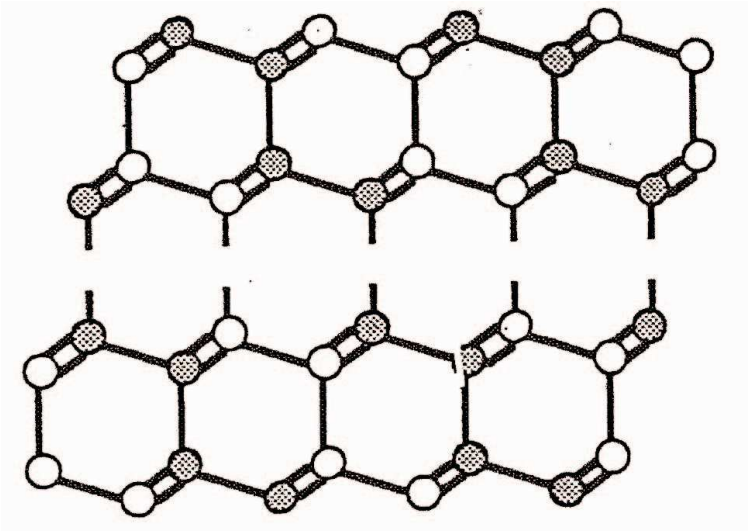

Figure 4.11: Molecular model for the {111} platelets. Only the silicon atoms are taken into consideration and broken bonds are supposed to be saturated by hydrogen. (figure taken from Muto et al. [21])

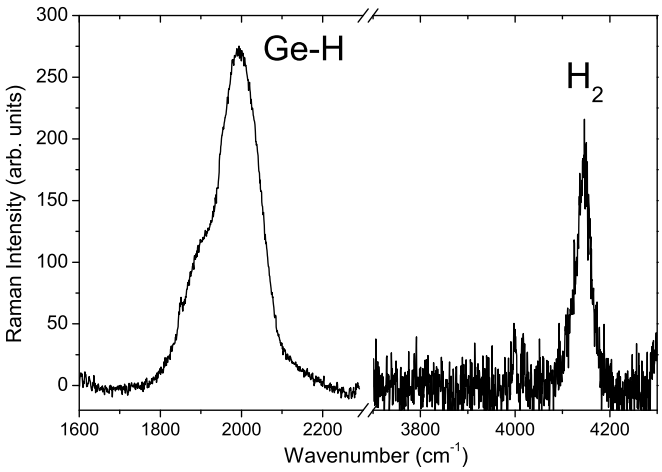

Figure 4.12: Raman Spectrum showing the $Ge-H$ and H_2 bonds present after 2.5h 150℃ hydrogenation. (measured at University of Dresden); same sample as in figure 4.8.

Comparing with the simulation of Hourahine et al. it may thus be concluded that in the first 10nm (i.e. the penetration depth of the laser used for raman measurements) the hydrogen preferentially forms {111} platelets with different H_2 concentrations.

In figure 4.13 the intensity of the Raman bands and of the infrared band due to $Ge-H$ are plotted as a function of the sample temperature during plasma treatment. The similar behaviour for the $Ge-H$ mode is obvious. Both the annealing behavior and the form of the $1980cm^{-1}$ band indicate that Raman and infrared measurements observe the same $Ge-H$ defect structure.

To compare the annealing behavior observed with positron annihilation spectroscopy with absorption spectroscopy, this sort of samples were also examined by means of absorption spectroscopy. In figure 4.14 the absorption spectrum of the $Ge-H$ stretch mode after two different plasma treatments for 4h is shown in detail. For a sample temperature of 150℃ a maximum absorption at

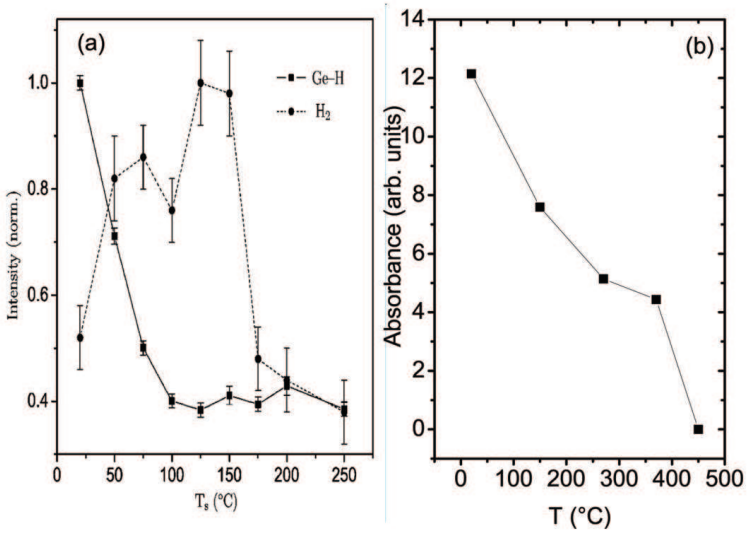

Figure 4.13: (a) Dependence of the integrated and normalized intensities of the Raman bands at $1980cm^{-1}$ for GeH and $4155cm^{-1}$ for H_2 on the sample temperature T during plasma treatment. (figure taken from Hiller et al. [5]) (b) Total infrared absorbance of the stretch mode as a function of plasma temperature for 6h ($0.3mA/cm^2$) (This work).

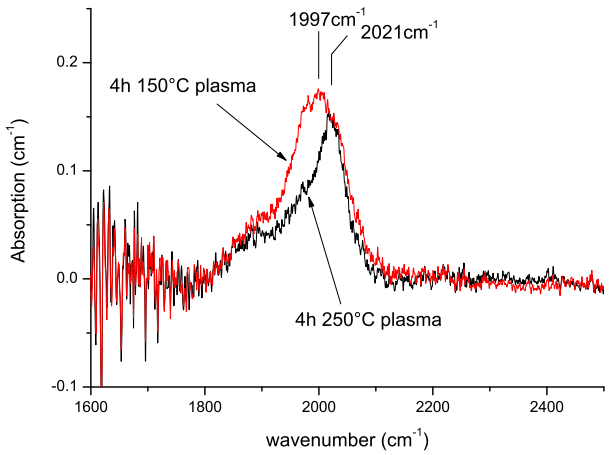

Figure 4.14: Absorption spectrum of as-plasma treated Ge sample: Ge-H stretching mode band. Measurements were made at room temperature using a resolution of $1cm^{-1}$ and interference fringes from multiple internal reflection has been removed.

$1980cm^{-1}$ is observed, while for a sample temperature of 250℃ the maximum shifts to $2020cm^{-1}$. This also corresponds with a reduction of the total absorption in this range. From the integrated absorption it can be concluded that for a higher plasma temperature less $Ge-H$ bonds have been formed. Although this stretching band may be due to a distribution of platelets with different H_2 concentration in the clusters, the different components corresponding with the calculated modes summarized in table 4.3 cannot be distinguished. The proof by means of high resolution TEM that direct or remote plasma treatments of silicon or germanium result in the formation of plate-like defects [21], are in agreement with the conclusion that this broad band originates from planar structures, which was also shown by the Raman study [5] using polarization measurements. Thus taking the simulated vibrational modes (table 4.3)into account it can be concluded that for the higher temperature treatment (250℃) in terms of percentage of the total amount of IR-active Ge-H bonds, more clusters involving more molecular hydrogen have been created.

Figure 4.15 shows the absorption spectra before and after additional anneal-

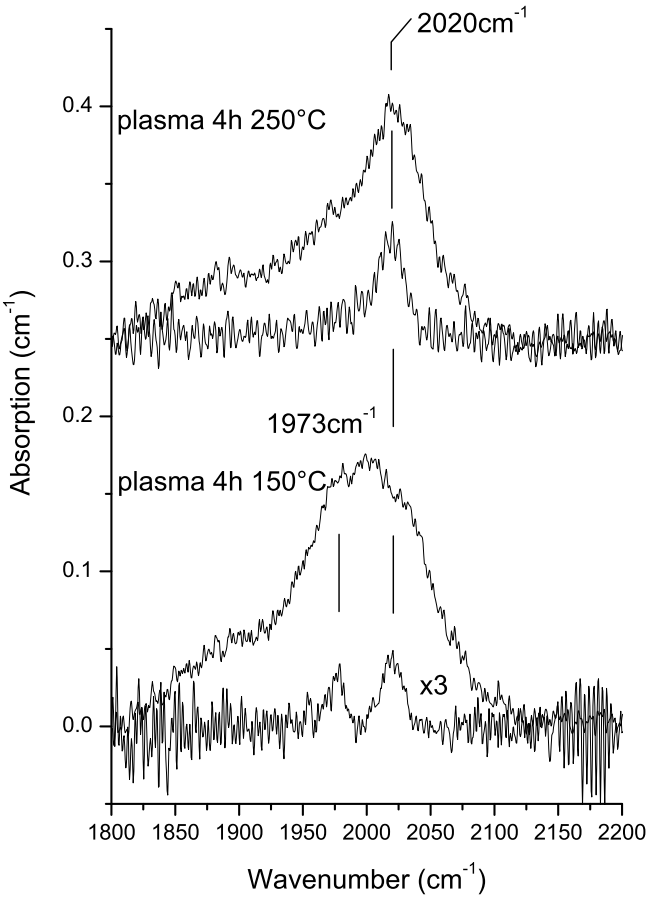

Figure 4.15: Absorption spectrum recorded at room temperature of samples hydrogenated at 150℃ and 250℃ before and after additional anneal at 400℃ for 30min under argon flow. Spectra have been shifted vertically for the clarity of the graph and a slowly varying background has been subtracted.

ing of the two samples at 400℃ for 30minutes under argon flow. A shorter annealing time was chosen comparing to the samples examined by means of positron annihilation because after a 2h 400℃ treatment no absorption within the stretching range ($2000cm^{-1}$) was left. In the spectrum corresponding with the 250℃ plasma sample only one band can be observed at $2020cm^{-1}$. While for the sample hydrogenated at 150℃ on the other hand two bands with low absorbance at $1973cm^{-1}$ and $2020cm^{-1}$ could be observed, which corresponding to the calculations summarized in table 4.3 can be assigned to the stretching band of $Ge-H$ in a $(2Ge-H+nH2)$ platelet structure. The fact that in a sample with this thermal history two distinct absorption bands can be resolved indicates that at least two different structures have formed in the crystal. Comparing with the original stretching band in the as plasma samples where it might be possible that also a part of the absorption is due to hydrogen decorated cavities, these two bands may be tentatively assigned to two types of platelets. From the range of platelets structures that have been calculated [20] one may assign the $1973cm^{-1}$ band to either the structure containing zero or one molecular hydrogen (predicted at $1966cm^{-1}$ and $1984cm^{-1}$ respectively). Although from the simulations it could be concluded that each type of structure results in two bands of $Ge-H$ related modes, we have not been able to detect two modes. Due to the weak absorption it may be possible that the second band remained undiscovered. If we assume that the shoulder at lower wavenumber in the absorption band directly after the hydrogenation (Figure 4.14) originates from the same defect structure being another vibrational mode, it might be possible that due to the difference in oscillator strength (in combination with the low concentration) the second mode is not visible after the annealing step. The total reduction of absorption by the annealing of the band around $2000cm^{-1}$ is not accompanied by increasing absorption in a different wavenumber range. In all these samples no other absorption band could be detected in the complete range from $900cm^{-1}$ to $4000cm^{-1}$.

4.6 Deep Level Transient Spectroscopy

Both n-type and p-type wafers with a net shallow dopant concentration of respectively $8 \times 10^{14} cm^{-3}$ and $1 \times 10^{14} cm^{-3}$ were examined. Schottky barriers were evaporated on the plasma treated surface. In this case no etching step was included in the preparation in order to allow measurement close to the defect rich region, although etching usually decreases the leakage current of the device.

The DLTS-spectrum of the two types of samples which received a hydrogenation for 150 minutes at 150℃ is shown in figure 4.16, the leakage current for both p- and n-type is below $10^{-4} A$. Due to the difference in doping concentration of the samples we can conclude that the band measured in the n-type sample originates from defects closer to the treated surface. The depletion width calculated from the quiescent capacitance extends between 0.8 μm and 1.4 μm for the biases used. Similar calculations for the p-type sample results in a depletion between 4 μm and 13 μm. From this we can conclude that the peaks seen in figure 4.16 originate from defects beyond the region where most of the platelets have been detected with TEM. Figure 4.17 shows the corresponding Arrhenius diagrams for the two defect levels. The corresponding signatures yield $E_C - E_T = 237meV$, $\sigma_a = 1.1 \times 10^{-18} cm^2$ and $E_T - E_V = 170meV$, $\sigma_a = 2.2 \times 10^{-18} cm^2$ for the n-type and p-type substrate respectively. It can be seen that the activation energies are remarkably close to the ionization energies 0.17eV and 0.23eV found for the charge-state transition for muonium (Mu) in tetrahedral and bond-centered position respectively [24]. Lichti et al. [24] observed two different charge cycles for Mu in germanium. One involves the Mu_T^0 center and the second involves Mu_{BC}^0. The best fit for both cases assumed a 0/+ charge cycle with electron ionization and recapture as the transition processes. Thus it might be possible that the E1 level 0.23 eV below the conduction band would be related to the following charge transfer $H_{BC}^0 \rightarrow H_{BC}^+ + e^-$. One should however be careful with this assignment since Dobacewski et al. [25] found a hydrogen bond centered donor level at

$E_c - 0.11eV$, which could only be observed after in situ hydrogen implantation at low temperature (80K), showing that interstitial hydrogen is not stable at room temperature. The H1 level is however a hole trap with level energy refered to the valence band, so it cannot be compared to the 0.17eV of muonium which is refered to the conduction band. A correspondence with other trap signatures in literature could not be found. The relation of E1 and H1 to the same defect structure could also not be demonstrated. However their absence in as grown germanium makes it likely to assign them to defects induced by the plasma treatment.

DLTS-spectra of the n-type sample as a function of the forward filling pulse are shown in figure 4.18. It can be seen that the spectrum is composed of a peak with constant position around 180K and another one at lower temperature, with position dependent on the pulse height. This broad band within 80K-160K reacts differently as a function of filling pulse applied comparing to the E1-level. The E1 level has the characteristics of a single defect level where only the amplitude changes for increasing pulse height. The broad band expands for increasing pulse heights to lower temperatures. This effect is typical for a continuum of states more close to the interface, because due to the increasing pulse bias the Fermi level shifts to higher electron energies close to the surface. Thus more states contribute to the DLTS-signal for a higher pulse. The latter DLTS-signal is thus typical of surface or interface states. In any case the measurements suggest that the plasma treatment results in states close to the treated surface, which are distributed in energy. Possible candidates for these bands are the platelets seen with TEM or surface states formed due to the radiation damage. From the E1-level profile shown in figure 4.19 it is seen that the trap concentration increases toward the surface. From the free carrier profile measured by SRP a small increase in the free carrier concentration is observed, which might be related to the broad DLTS-band located close to the surface or could be due to the extrapolated concentration of E1 toward the surface.

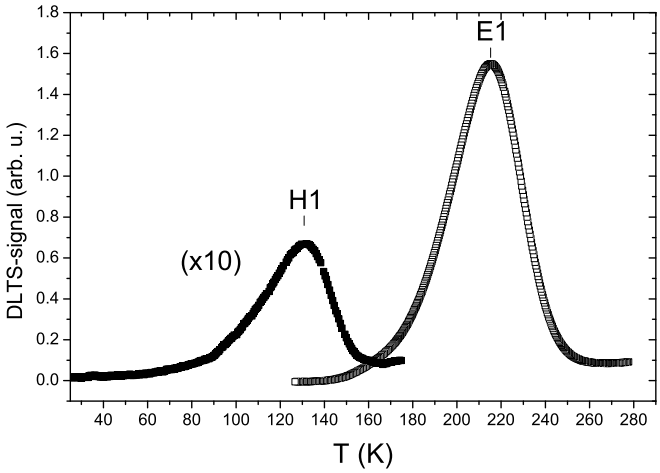

Figure 4.16: DLTS-spectra of n- and p-type germanium plasma treated for 150minutes at 150℃. Reverse bias = 1V, pulse voltage = 0V. T_w = 51.4 ms and 19.9 ms for the p-type and n-type respectively.

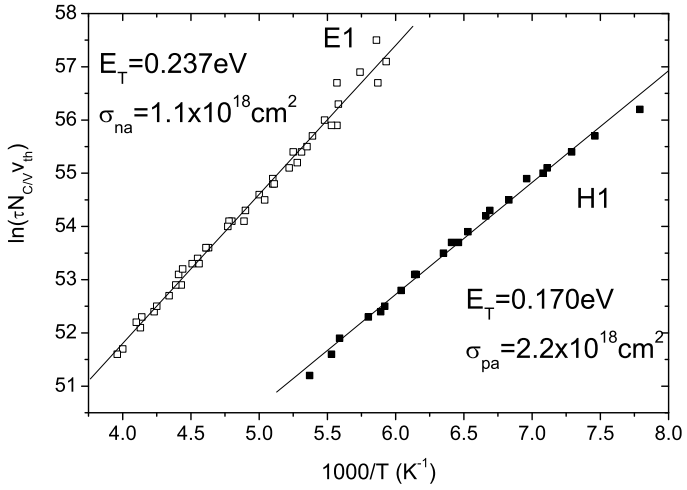

Figure 4.17: Arrhenius plot of DLTS-peaks E1 and H1 observed in figure 4.16.

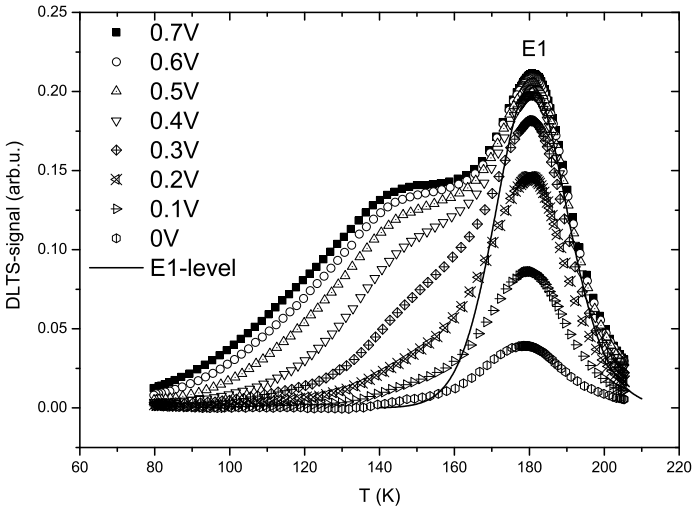

Figure 4.18: DLTS-spectra of the the n-type plasma treated Ge sample at different forward biases. The full line shows the band corresponding with the single bulk level E1. Spectra have been recorded with constant reverse bias (-5V), emission window $T_w = 51.4ms$ and pulse duration $t_p = 50ms$.

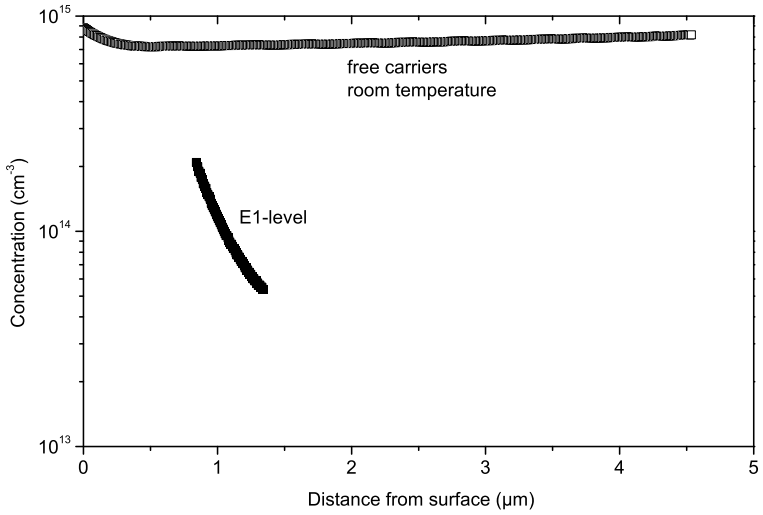

Figure 4.19: Trap level profile measured for the E1 level in n-type germanium after hydrogenation (DLTS, measured by variation of the reverse bias), and free carrier concentration at room temperature (SRP)

4.6.1 Laplace Transform Deep Level Transient Spectroscopy

Laplace Transform DLTS[1] has been applied to the n-type sample of figure 4.18 in order to further investigate the broad band at lower temperatures. Laplace DLTS is a numerical tool that uses the inverse Laplace transform of the exponential capacitance transient and is able to resolve different emission constants better than standard DLTS. The spectral function $F(s)$ is defined as the solution of the integral:

$$C(t) = \int_0^{+\infty} F(s)e^{-st}ds \tag{4.8}$$

where $C(t)$ is the capacitance transient. The exponential function e^{-st} describes a single emission with s the emission rate over which will be integrated. Because the transient of the capacitance can only be recorded on a discrete number (N) of points (k) equation 4.8 is written as:

$$C(t_k) = \sum_{m=1}^{N} F(s_m)e^{-s_m t_k} \tag{4.9}$$

A review of different methods to solve this equation and their application in Laplace DLTS was given by Dobaczewski et al. [26]. To analyze our transients the CONTIN [27] procedure was modified and implemented in our DLTS-software. CONTIN is a general program package written in Fortran IV for solving equation 4.9. Equation 4.9 is an ill-posed problem. This means that for an arbitrary small error (i.e. noise on the measurement), there exist a large set of possible solutions, all satisfying equation (4.9) within the experimental error. The members of this set of solutions can have arbitrary large deviations from each other and therefore from the true solution. The CONTIN program uses the following strategy. First it adds the constraint that the spectral function $F(s)$ should be positive. This is very powerful because it can eliminate the oscillating solutions. Secondly it uses a least square fit to the experimental data. As last from all the solutions left it chooses the simplest one (i.e. the one that reveals the least amount of detail or information that was not expected)

[1] Standard DLTS will be discussed as an introduction in chapter 5.

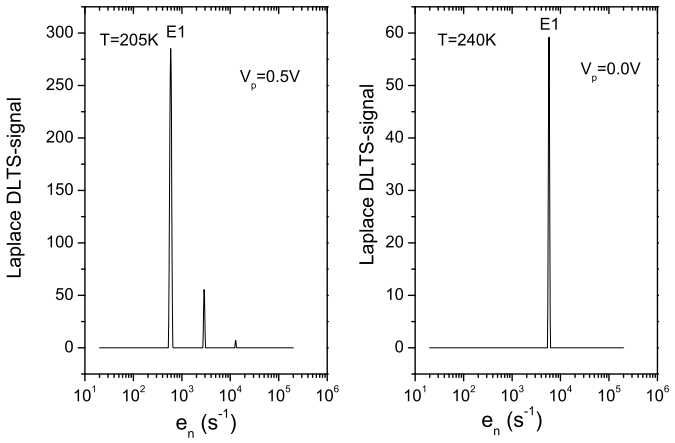

Figure 4.20: Laplace DLTS-spectra at two pulse conditions (a) the E1 level and additional features due to the defects closer to the surface, (b) The E1 level.

The detail detected in the final solution is thus less likely to be artifact. Figure 4.20 shows the Laplace DLTS-spectra with (a) and without (b) forward bias. It is seen that with a pulse $V_p = 0V$ only the E1 level could be observed, while for a pulse $V_p = 0.5V$ additional emission rates contribute to the transient. The latter probably correspond with the deep-level defects closer to the surface. Since the CONTIN routine selects the most simple solution however, it may be that a continuous emission from a broad distribution of bands is approximated by two emission rates.

4.7 Plasma treated oxygen doped germanium

A recent review on oxygen in Ge was given by Clauws in Ref. [28]: In order to obtain germanium with high oxygen concentration, i.e. $10^{16} - 10^{18}$ at cm^{-3}, it is necessary to dope the crystal deliberately, for instance by mixing oxygen gas or water vapor into the growth atmosphere. In similar material, defects consisting of agglomerated oxygen are formed besides O_i during crystal growth or

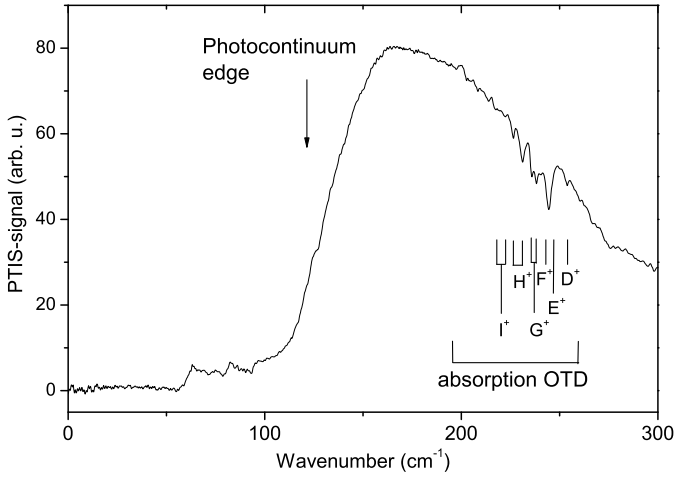

Figure 4.21: PTIS-spectrum of oxygen doped germanium after plasma treatments for 4h at 200℃. The characters $D^+ - I^+$ indicate OTD^+ species [30].

thermal treatments. Small clusters which form in the $300-500$℃ temperature range and contain a limited numbers of oxygen atoms, display donor activity and are called thermal donors (OTDs). Those OTDs are similar oxygen clusters as observed in silicon (see also chapter 2). During prolonged treatments at $550-650$℃, GeO_x precipitates are formed instead. Recently enhanced donor formation was observed in oxygen containing germanium by Kazuchits et al. [29] due to the plasma treatments, similar as discussed in chapter 2 for silicon. Kazuchits showed enhanced donor formation in oxygen rich p-type Ge crystals, which created a deep junction up to a depth of 1mm.

To investigate the formed donors a PTIS measurement was performed on an oxygen containing germanium sample after a 4h 200℃ plasma treatment. The plasma treatment was preceded with a quench from 900℃ to freeze-in almost all oxygen atoms in the interstitial position. The sample had an O_i concentration of $3 \times 10^{17} cm^{-3}$. Figure 4.21 shows the PTIS-spectrum of the hydrogenated sample. Between $120 cm^{-1}$ and $300 cm^{-1}$ a photocontinuum is observed. In this continuum absorption peaks due to the OTD^+ species ap-

pear as negative lines. Within the spectral range of $50 - 100cm^{-1}$ other PTIS features are present. The photocontinuum edge can correspond with neutral OTDs, however due to the absence of corresponding PTIS excitation lines, this assignment is uncertain. The absence of excited OTD^0 lines may be explained by a too low measurement temperature, for which thermal ionization is less probable. For higher temperatures however ($\approx 9K$), the measurement was too noisy. The features between $50cm^{-1}$ and $100cm^{-1}$ are possibly due to donors shallower than the OTD. Since the features are absent in as quenched material [30], this signal is probably due to a plasma related effect. Different attempts to improve the quality of this signal failed, but confirmed the presence of the shallow defects. The formation of OTD until species I is normally observed after thermal anneals at higher temperature [30]. Their presence after a treatment at only 200℃ also indicates a hydrogen-plasma effect. It may however be remarked that enhanced OTD formation has also been observed after electron irradiation of germanium [31], so that radiation damage due to the treatment may also play a roll.

4.8 Conclusions

Figure 4.22 shows an overview of the defects observed in H-plasma treated germanium using different experimental techniques, as a function of probed depth below the surface. Close to the surface within the first 10nm, $Ge-H$ bonds and H_2 molecules are observed by means of Raman spectroscopy. No polarization sensitive measurements were performed, however the similar position and form of the peak comparing to the work of Hiller et al. [5] allow to assign the vibrational modes to $Ge-H$ bonds and H_2 within {111} platelets. TEM has probed the first micron. Within this micron two regions could be distinguished. The first region until 70nm is heavily damaged and contains mostly {111} platelets. A second region ($70 - 1100nm$) contains plate-like cavity clusters oriented in {100} and {111} planes. The cavities inside are 2-5nm in diameter. Slow positron annihilation spectroscopy probes about the same region as the one

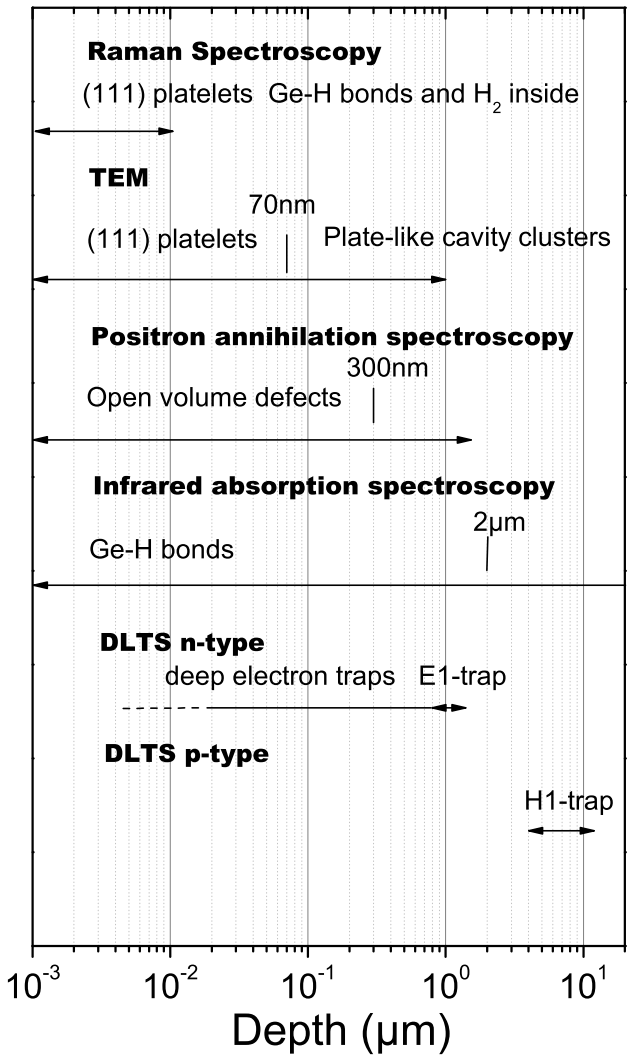

Figure 4.22: Overview of the defects induced in germanium by means of plasma hydrogenation.

examined by TEM. To first order the region with the defects observed can be approximated as 300nm thick. The positron signature corresponds with open volume defects of minimum 3 vacancies. The S-parameter might be influenced by the presence of hydrogen, so the positron possibly annihilates in the cavities observed by TEM. It may be emphasized that the depth of these structures is in good agreement with the one calculated from the size of the blisters.
Infrared absorption spectroscopy in general measures the absorption integrated over the total sample thickness, but the disappearance of the bands after removal of approximately the first 2 micron demonstrates that the signal originates from this layer. Both the stretch and wag mode of $Ge-H$ bonds in this region could be observed. The position of these bands are close to the frequencies calculated by Cardona [19]. The same trend in the infrared measurements as observed by Hiller et al. [5] in the formation of $Ge-H$ bonds as a function of sample temperature during the plasma treatment suggest the assignment of this $Ge-H$ band to the one in the $\{111\}$ platelets. The similarity (i.e. the same position and form) of the $Ge-H$ stretch band in infrared absorption and Raman spectroscopy supports this assignment. It means that the largest fraction of Ge-H bonds in the sample has formed in the $\{111\}$ platelets within the first 70nm, and that only a small fraction is involved in the cavities. However the small increase in S-parameter for an open volume defect of 2-5nm suggests the presence of hydrogen in the cluster. The diameter 2-5nm corresponds with open volume defects larger than three vacancies and thus this increase in S-parameter may also be assigned to an open volume defect with a diameter of 2-5nm loaded with hydrogen. The different annealing behavior of the positron signal and absorption of the $Ge-H$ band suggests the different nature of these spectroscopically observed defects. This may be tentatively explained if the positrons only observe the cavities and the $Ge-H$ bond concentration in the cavities is below the detection limit of infrared absorption spectroscopy. The $Ge-H$ absorption band reduces significantly in absorbance after 30 min anneal, while distinct peaks become observable. The position of the peaks is in very good agreements with the DFT-calculations of Hourahine et al. [20]

for the {111} platelets. The band at $1973cm^{-1}$ was assigned to either a {111} platelet with no or one hydrogen molecule in the structure. While the band at $2020cm^{-1}$ was assigned to the {111} platelets with two hydrogen molecules.
DLTS of an n-type sample reveals the E1 electron trap with a decreasing profile between $0.8\mu m$ and $1.4\mu m$. Not only this E1 level could be observed but also a broad band, which has the typical characteristics of defect structures more close to the surface. The same spatial region of the cavities observed by TEM and Positron annihilation spectroscopy makes the tentative assignment of the broad band to these clusters plausible. Due to the lower dopant concentration the DLTS of p-type probes the region between 4μm and $13\mu m$ and only a very weak H1 level could be observed.
The fact that the plasma hydrogenation can result in the formation of observable blisters on the surface, links the plate-like cavity clusters parallel to the treated surface to the defects that mediate the layer transfer in smart-cut technologies.
In hydrogenated oxygen doped germanium a signal was observed, which is related to the hydrogenation and might be a potential candidate for the observation of a hydrogen related shallow donors in germanium.

Bibliography

[1] R.C. Frank and J.E. Thomas. The diffusion of hydrogen in single-crystal germanium. *Journal of physics and chemistry of solids*, 16:144, 1960.

[2] J. Weber, M. Hiller, and E.V. Lavrov. Hydrogen in germanium. *Materials science in semiconductor processing*, 9:564, 2006.

[3] S.K. Estreicher and Dj.M. Maric. What is so strange about hydrogen interactions in germanium. *Physical review letters*, 70:3963, 1993.

[4] C.G. Van de Walle and J. Neugebauer. Universal alignment of hydrogen levels in semiconductors, insulators and solutions. *Nature*, 423:626, 2003.

[5] M. Hiller, E.V. Lavrov, and J. Weber. Hydrogen-induced platelets in ge determined by raman scattering. *Physical review B*, 71:045208, 2005.

[6] M. Bruel. Application of hydrogen ions beams to SOI material technology. *Nuclear istruments and methods in physics research B*, 108:313, 1996.

[7] X. Feng and Y. Huang. Mechanics of smart-cut technology. *International journal of solids and structures*, 41:4299, 2004.

[8] F. Yang. Hydrogen-induced silicon wafer splitting. *Journal of applied physics*, 94:1454, 2003.

[9] T. Akatsu, C. Deguet, L. Snachez, F. Allibert, D. Rouchon, T. Signamarcheix, C. Richtarch, A. Boussagol, V. Loup, F. Mazen, J.M. Hartmann, Y. Campidelli, L. Clavelier, F. Letertre, N. Kernevez, and

C. Mazure. Germanium-on-insulator (GeOI) substrates - a novel engineered substrate for future high performance devices. *Materials science in semiconductor processing*, 9:444, 2006.

[10] T. Akatsu, K. K. Bourdelle, C. Richtarch, B. Faure, and F. Letertre. Study of extended-defect formation in ge and si after h ion implantation. *Applied physics letters*, 86:181910, 2005.

[11] M.L. David, F. Pailloux, D. Babonneau, M. Drouet, J.F. Barbot, E. Simoen, and C. Claeys. The effect of the substrate temperature on extended defects created by hydrogen implantation in germanium. *Journal of applied physics*, 102:096101, 2007.

[12] L.J. Huang, Q.Y. Tong, Y.L. Chao, T.H. Lee, T. Martini, and U. Gösele. Onset of blistering in hydrogen implanted silicon. *Applied physics letters*, 74(7):982, 1999.

[13] J. Grisolia, G. Ben Assayag, A. Claverie, B. Aspar, C. Lagahe, and L. Laanab. A transmission electron microscopy quantitative study of the growth kinetics of h platelets in si. *Applied physics letters*, 76:852, 2000.

[14] P.F.P. Fichtner, J.R. Kaschny, R.A. Yankov, A. Mücklich, U. Kreissig, and W. Skorupa. Overpressurized bubbles versus voids formed in helium implanted and annealed silicon. *Applied physiscs letters*, 70:732, 1997.

[15] E. Oliviero, M.F. Beaufort, and J.F. Barbot. Dislocations induced by bubble formation in high energy he implantation in silicon. *Journal of applied physics*, 89:5332, 2001.

[16] J. De Baerdemaeker and C. Dauwe. Development and application of the ghent pulsed positron beam. *Applied Surface Science*, 194:52, 2002.

[17] A. Van Veen, H. Schut, J. de Vries, R.A. Hakvoort, and M.R. IJpma. *Positron Beams for Solids and Surfaces, AIP Conf. Proc. No. 218, P.J. Schultz and G.R. Massoumi and P.J. Simpson*, page 171. AIP, New-York, 1990.

[18] B. Nielsen, O. W. Holland, T. C. Leung, and K. G. Lynn. Defects in MeV Si-implanted Si probed with positrons. *Journal of Applied Physics*, 74:1636, 1993.

[19] M. Cardona. Vibrational spectra of hydrogen in silicon and germanium. *Physica status solidi b*, 118:463, 1983.

[20] B. Hourahine, R. Jones, and P.R. Briddon. Hydrogen molecules and platelets in germanium. *Physica B*, 376:105, 2006.

[21] S. Muto, S. Takeda, and M. Hirata. Hydrogen-induced platelets in silicon studied by transmission electron-microscopy. *Philosophical magazine A-Physics of condensed matter structure defects and mechanical properties*, 72(4):1057, 1995.

[22] E.V. Lavrov and J. Weber. Ortho and para interstitial H-2 in silicon. *Physical review letters*, 87:185502, 2001.

[23] J.N. Heyman, J.W. Ager III, E.E. Haller, N.M. Johnson, J. Walker, and C.M. Doland. Hydrogen-induced platelets in silicon - infrared-absorption and raman-scattering. *Physical review B*, 45:13363, 1992.

[24] M. Budde, B.Bech Nielsen, C. Parks Cheney, N.H. Tolk, and L.C. Feldman. Local vibrational modes of isolated hydrogen in germanium. *Physical review letters*, 85:2965, 2000.

[25] L. Dobaczewski, K.Bonde Nielsen, N. Zangberg, B.Bech. Nielsen, A.R. Peaker, and V.P. Markevich. Donor level of bond-center hydrogen in germanium. *Physical review B*, 69:245207, 2004.

[26] L. Dobaczewski, A.R. Peaker, and K. Bonde Nielsen. Laplace-transform deep-level spectroscopy: The technique and its applications to the study of point defects in semiconductors. *Journal of applied physics*, 96(9):4689, 2004.

[27] S.W. Provencher. Contin: A general purpose constrained regularization program for inverting noisy linear algebraic and integral equations. *Computer physics communications*, 27:229, 1982.

[28] E. Simoen and C. Claeys. *Germanium based technologies, from materials to devices*. Elsevier, 2007.

[29] N.M. Kazuchits, V.V. Litvinov, L.I. Murin, and V.A. Martinovich. Enhanced formation of oxygen-related thermal donors in ge crystals exposed to hydrogen plasma. *Materials science in semiconductor processing*, 9(4):625, 2006.

[30] P. Clauws. *Spectroscopische methodes voor de bepaling van defecten in halfgeleiders; identificatie en studie van de fysische eigenschappen van thermische donors in zuurstofrijk germanium*. Universiteit Gent, 1991.

[31] P. Vanmeerbeek and P. Clauws. Local vibrational mode spectroscopy of dimer and other oxygen-related defects in irradiated and thermally annealed germanium. *Physical review B*, 64(24):245201, 2001.

Chapter 5

Measurement of carrier capture cross-sections in DLTS; application to transition metal impurities in germanium

5.1 Introduction

The purpose of this chapter is: i) to describe the fitting method we developed to determine the capture cross-section for carriers at deep levels observed in DLTS, ii) to apply the method to deep levels from transition metal (TM) impurities in germanium which are studied in our research group. The passivation of these metal centres by hydrogen will then subsequently be investigated in the next chapter.

The accurate determination of the capture cross-section using a space charge technique like DLTS is a delicate problem, due to slow capture from free carrier tails. Accurate data on the capture cross-section and its temperature dependence are nevertheless very important. In the first place the cross-section is an important parameter with respect to the working of devices (leakage, lifetime

Ě). In DLTS the direct measurement of the capture cross-section also allows to extract deep level parameters like the entropy and enthalpy of the transitions, resulting in a parameter set allowing comparison with results from other techniques and with predictions from theoretical models. Theoretical results for TM centres in germanium may probably be expected in the near future. First in the next section an overview will be given of DLTS items relevant in the present context.

5.2 Deep Level Transient Spectroscopy

5.2.1 Emission of a carrier

The emission and capture of carriers can be described by the following rate equation (a schematic diagram clarifying the different processes is shown in figure 5.1):

$$\frac{dn_T(t)}{dt} = (c_n n + e_p)\,(N_T - n_T(t)) - (c_p p + e_n)\,n_T(t) \tag{5.1}$$

Herein $n_T(t)$ represents the number of deep levels occupied by an electron and $c_n n$, $c_p p$, e_n and e_p are the electron capture, hole capture, electron emission and hole emission rate constants respectively. Integration of (5.1) gives the trap occupation as a function of time:

$$n_T(t) = \left(n_T(0) - \frac{(c_n n + e_p)\,N_T}{c_n n + e_p + c_p p + e_n}\right) e^{-t(c_n n + e_p + c_p p + e_n)} + \frac{(c_n n + e_p)\,N_T}{c_n n + e_p + c_p p + e_n} \tag{5.2}$$

where $n_T(0)$ is the initial occupation. From equation (5.2) it can be seen that in equilibrium, which corresponds with $t = +\infty$, the fractional electron occupation of the trap becomes:

$$f_T = \frac{n_T(+\infty)}{N_T} = \frac{c_n n + e_p}{c_n n + e_n + c_p p + e_p}. \tag{5.3}$$

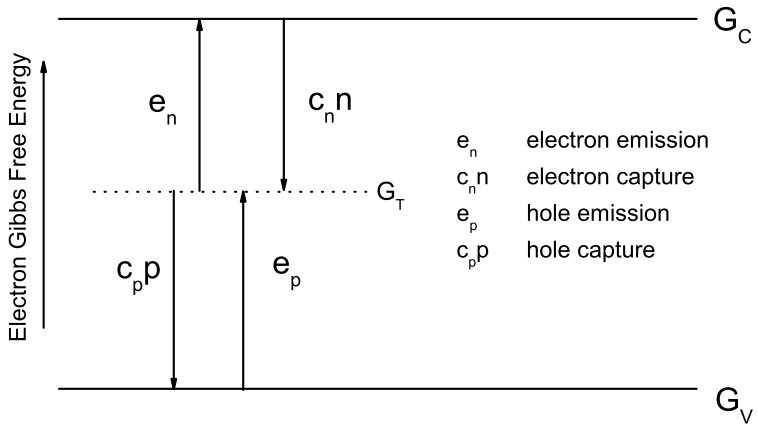

Figure 5.1: Energy diagram showing the emission and capture of holes and electrons at a deep trap level. The arrows correspond to the transition of an electron.

The fractional occupation of a level in equilibrium can be calculated using a Fermi-Dirac distribution, thus equation (5.3) can be set equal to:

$$f_T = \frac{1}{e^{\frac{G_T-\mu}{k_B T}} + 1}. \tag{5.4}$$

Herein G_T corresponds with the Gibbs free energy of an electron in the ground state bound to the defect structure and μ is the chemical potential, k_B is the Boltzmann constant and T the temperature. The free electron and free hole concentrations are given by:

$$n = N_C e^{\frac{\mu-G_C}{k_B T}} \tag{5.5a}$$

$$p = N_V e^{\frac{G_V-\mu}{k_B T}} \tag{5.5b}$$

where N_V and N_C are the density of states of the valence and conduction band respectively, G_V and G_C are the Gibbs free electron energy corresponding with the electron in the bands. Setting the fractional occupation in equilibrium equal to the Fermi-Dirac distribution yields:

$$\left(c_n N_c e^{\frac{G_T-G_C}{k_B T}} - e_n\right) + e^{\frac{-\mu}{k_B T}} \left(e_p e^{\frac{G_T}{k_B T}} - c_p N_V e^{\frac{G_V}{k_B T}}\right) = 0. \tag{5.6}$$

Equation (5.6) is valid for all carrier concentrations and thus independent of the chemical potential (μ). This is only valid if both terms in (5.6) are zero. Thus the emission rate constants for electrons and holes are:

$$e_n = c_n N_C e^{\frac{G_T - G_C}{k_B T}} \tag{5.7a}$$

$$e_p = c_p N_V e^{\frac{G_V - G_T}{k_B T}} \tag{5.7b}$$

The electron and hole emission rates constants are proportional to the electron or hole capturing rates respectively.

5.2.2 Capture of a carrier

The capture of a carrier by a deep level can be described using standard collision theory. Here a carrier with speed $\|\vec{v}\|$ interacts within a time Δt with the traps in a volume $\sigma \|\vec{v}\| \Delta t$. Where σ is the cross-section for the reaction of trapping a carrier. Because the density of traps unoccupied by an electron is $N_T - n_T$, the probability (P) that a carrier moving at speed $\|\vec{v}\|$ gets trapped by one of the $N_T - n_T$ available traps within time Δt is given by:

$$P(\Delta t) = \sigma \|\vec{v}\| \Delta t \, (N_T - n_T) \tag{5.8}$$

Including the carrier density (for example for electrons n) the occupation change of a trap Δn_T within time Δt is given by:

$$\Delta n_T = n\sigma \|\vec{v}\| \Delta t \, (N_T - n_T) \tag{5.9}$$

Because (5.9) is analogous to the rate equation (5.1) the general electron and hole capture in a semiconductor reduces to:

$$c_n n = \sigma_n < v_n > n \tag{5.10a}$$

$$c_p p = \sigma_p < v_p > p \tag{5.10b}$$

Here σ_n and σ_p are the electron and hole capture cross section respectively and $< v_n >$ and $< v_p >$ are the average thermal velocity of the electrons and holes respectively. Describing the carriers as a 3 dimensional non-interacting

Boltzmann gas with particles having the effective mass m^* the Maxwell-speed distribution becomes:

$$f(\|v\|) = 4\pi \left(\frac{m^*}{2\pi k_B T}\right)^{\frac{3}{2}} v^2 e^{\frac{-m^* v^2}{2k_B T}} \tag{5.11}$$

$$v_{prob} = \sqrt{\frac{2k_B T}{m^*}} \tag{5.12a}$$

$$\bar{v} = \sqrt{\frac{8k_B T}{\pi m^*}} \tag{5.12b}$$

$$v_{rms} = \sqrt{\frac{3k_B T}{m^*}} \tag{5.12c}$$

Here v_{prob} is the most probable velocity, $\bar{v}$ is the mean velocity and v_{rms} is the root mean squared speed of the distribution. It is general practice to identify the thermal velocity of the carriers with v_{rms} which corresponds with the equipartition law of Boltzmann:

$$\frac{1}{2} m^* v_{rms}^2 = \frac{3}{2} k_B T \tag{5.13}$$

The Maxwell distribution for n-type germanium is shown in figure 5.2 for different temperatures, the corresponding root mean squared speeds are also indicated.

5.2.3 Changing the occupation of a trap in the DLTS-experiment

The kinetics of filling and emission of carriers by a deep level in a DLTS-experiment may be conveniently studied using a Schottky barrier or p^+n or n^+p device. How the change in applied bias over the sample will result in a succession of trapping and emission of the carriers, is described below. We assume a n-type semiconductor with a shallow dopant concentration N_D and a deep level concentration $N_T << N_D$, on top of which a metal was evaporated resulting in a Schottky barrier. The depletion width W_r at a given reverse bias $V_r < 0$ is given by:

$$W_r = \sqrt{\frac{2\epsilon}{qN_D}\left(U_b - V_r - \frac{k_B T}{q}\right)} \tag{5.14}$$

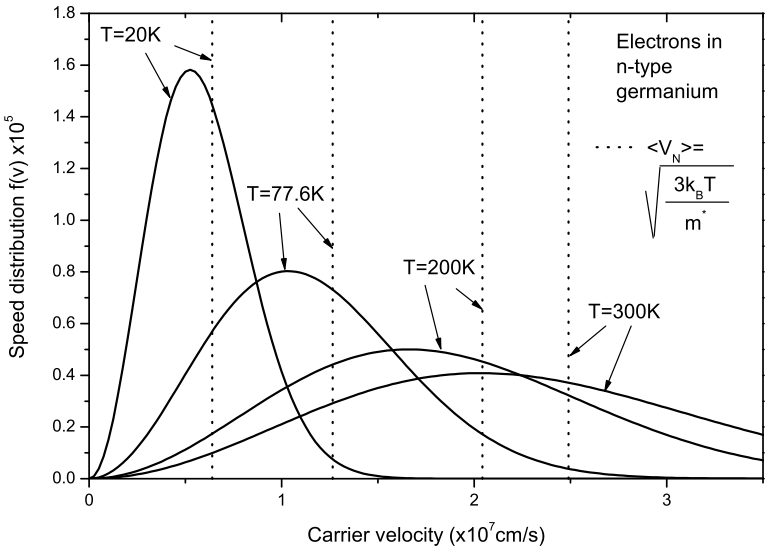

Figure 5.2: Maxwell speed distribution for electrons in germanium having an effective mass $m_e^* = 0.22m_e$ for different temperatures.

where U_b is the built-in potential related to the barrier height [1]. This means that if we switch from a reverse bias V_r to a reverse bias V_p and $V_p > V_r$, the region between the depletion in case V_r (W_r) and V_p (W_p) will fill with carriers. The range where capture of carriers into a deep level E_T will occur is indicated in figure 5.3. The distance between the depletion edge W and the edge of the region where the carriers will fill the deep levels is given by:

$$\lambda = \sqrt{\frac{2\epsilon\left(E_F - E_T\right)}{q^2 n_0}} \tag{5.15}$$

with n_0 the free carrier density and is defined by the position were the Fermilevel (E_F) crosses the trap level E_T. If the reverse bias V_r is restored again the deep levels will emit their carriers. The filling of and emission from these levels is reflected in the capacitance (C) of the diode. A schematic view of the capacitance as a function of time is shown in figure 5.4. Solving Poisson's

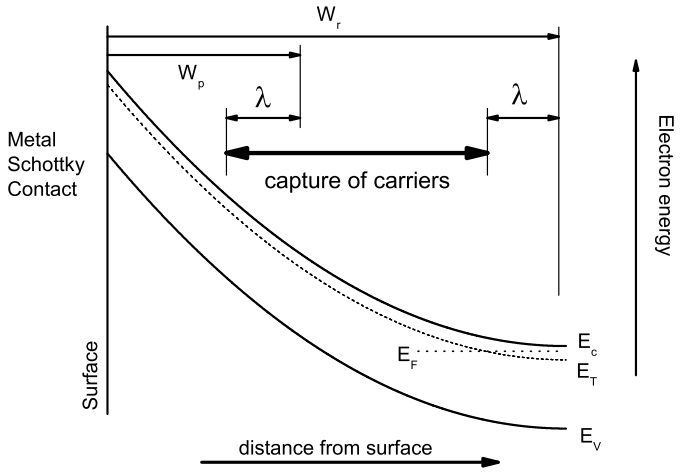

Figure 5.3: Band diagram of n-type semiconductor under reverse bias showing the region where the free carriers will be captured under pulse bias condition.

equation in both reverse and pulse configuration it is found that:

$$\frac{\epsilon\left(U_b + V_{r/p}\right)}{q} = \int_0^{W_{r/p}-\lambda} \left(n_0 + N_T\right) x dx + \int_{W_{r/p}-\lambda}^{W_{r/p}} n_0 x dx \tag{5.16}$$

In this case a deep donor level which is a $0/+$ is assumed, although a similar calculation can be made assuming an acceptor level. A similar integral can be written for the total charge (Q) in the semiconductor with A the area of the metal-semiconductor contact:

$$\frac{Q}{Aq} = n_0 W_r + N_T \left(W_r - \lambda\right) \tag{5.17}$$

Because λ is independent of the applied bias V_r, which can be seen from formula (5.15), the high frequency reverse capacitance C applying a bias V_r can be calculated:

$$C_r = \frac{dQ}{dV_r} = \frac{dQ}{dW_r}\frac{dW_r}{dV_r} = \frac{A\epsilon\left(n_0 + N_T\right)}{\left(n_0 + N_T\right) W_r - N_T \lambda} \tag{5.18}$$

This equation can for a low deep level concentration be approximated as

$$C_r = \frac{A\epsilon}{W_r} \tag{5.19}$$

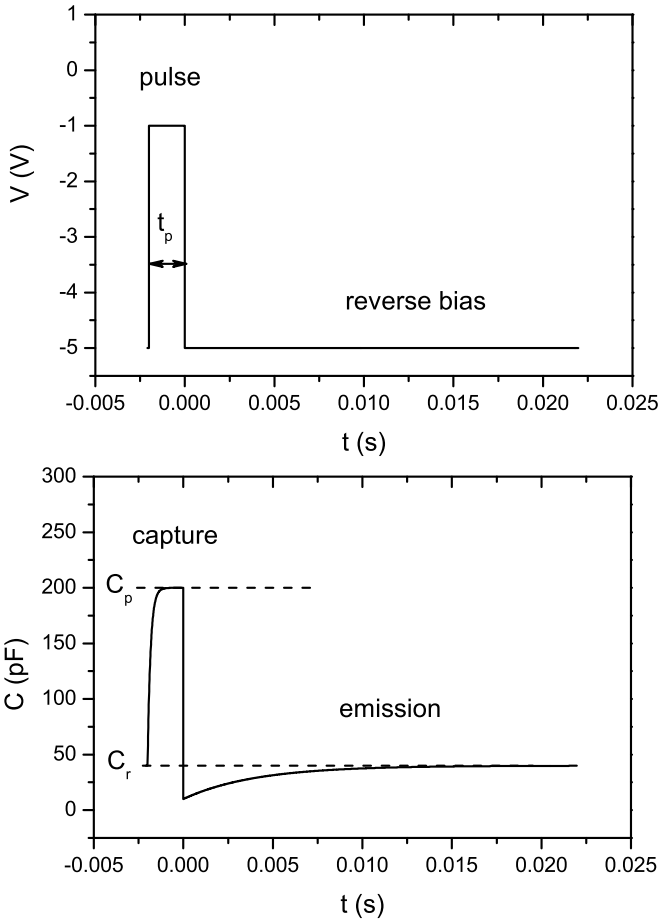

Figure 5.4: Schematic view of the applied voltage and corresponding capacitance as a function of time during a DLTS experiment

On the other hand one can see that for very high deep level concentrations $N_T >> n_0$ the capacitance becomes:

$$C_r = \frac{A\epsilon}{W_r - \lambda} \tag{5.20}$$

Without deep levels E_T and for a constant free carrier profile n_0 one can calculate the dependence of the capacitance on the variation of the bias:

$$\frac{d\left(\frac{1}{C_r^2}\right)}{dV_r} = \frac{d\left(\frac{1}{C^2}\right)}{dW_r}\frac{dW_r}{dV_r} = -\frac{2}{q\epsilon A^2 n_0} \tag{5.21}$$

From (5.21) it follows that the slope of a $1/C^2$-plot as a function of V_r is inversely proportional to the free carrier concentration n_0. A similar plot is called a Mott-Schottky plot. If n_0 is not constant the free carrier profile can be determinded from $\frac{d(1/C^2)}{dV}$.
The transient $C(t)$ after the voltage pulse (figure 5.4) may be separated in two parts. First the free carriers react, which can be approximated as instantaneously while the deep levels are still occupied. To describe this one has to analyze the Poisson equation.

$$\frac{\epsilon\left(U_b + V_r\right)}{q} = \int_0^{W_p-\lambda} \left(N_T\right) x dx + \int_0^{W_r+\Delta W_r} n_0 x dx \tag{5.22}$$

while the total charge Q in the semiconductor is:

$$\frac{Q}{Aq} = \int_0^{W_p-\lambda} \left(N_T\right) dx + \int_0^{W_r+\Delta W_r} n_0 dx \tag{5.23}$$

Here ΔW_r is the additional distance that is needed to keep the potential difference over the semiconductor constant during this process. From this the capacitance $C(t=0)$ directly after the pulse becomes:

$$C(t=0) = \frac{dQ}{d\Delta W_r}\frac{d\Delta W_r}{dV_r} = \frac{A\epsilon}{W_r + \Delta W_r} \tag{5.24}$$

Because the same potential is present in equilibrium (5.16) and directly after the pulse (5.22), one can easily see that $\Delta W_r > 0$. Thus the second part, usually much slower due to the emission of carriers from the deep traps described

by equation (5.2) has an amplitude $\Delta C < 0$. Comparing equations (5.16) and (5.22) one can calculate this ΔW_r and the change in the capacitance ΔC

$$\frac{N_T \left(W_p - \lambda\right)^2}{2} + \frac{n_0}{2} \left(W_r - \Delta W_r\right)^2 = \frac{n_0 W_r^2}{2} + \frac{N_T \left(W_r - \lambda\right)^2}{2} \tag{5.25}$$

$$\left(\left(1 - \frac{\Delta C}{C_r}\right)^{-2} - 1\right) \frac{n_0}{N_T} = \frac{\left(W_r - \lambda\right)^2 - \left(W_p - \lambda\right)^2}{W_r} \tag{5.26}$$

Herein $(1 - \frac{\Delta C}{C_r})^{-2} \approx 1 + 2\frac{\Delta C}{C_r}$ can be used for $\Delta C << C_r$. The right side of equation (5.26) is called the pulse correction factor and is used to calculate the trap concentration.

5.2.4 Analyzing the capacitance transient

As described in section 5.2.3 the presence of deep levels in the bandgap of the semiconductor results in a capacitance transient with amplitude ΔC. To analyze the transient one can use equation (5.2) which describes the trap occupation as a function of time. In the equation of Poisson the total potential difference over the semiconductor in equilibrium condition is set equal to the total potential difference during the emission of carriers:

$$\begin{aligned} \frac{\epsilon \left(U_b + V_r\right)}{q} = \frac{N_T}{2} \left(W_p - \lambda\right) + \\ \frac{\left(N_T - n_T(t)\right)}{2} \left(\left(W_r - \lambda\right)^2 - \left(W_p - \lambda\right)^2\right) + \frac{n_0}{2} \left(W_r + \Delta W_r(t)\right)^2 \end{aligned} \tag{5.27}$$

A similar calculation as in section 5.2.3 will result in the conclusion that for small relative defect concentrations the capacitance is proportional to $n_T(t)$. Because $n_T(t)$ can be written (see equation 5.1) as an exponentional decay with a rate constant:

$$\tau = \frac{1}{c_n n + e_p + c_p p + e_n} \tag{5.28}$$

the capacitance will converge exponentially to C_r with the same rate. Since the capacitance transient is recorded when the semiconductor is depleted no free carriers are present and the rate constant can be rewritten as:

$$\tau = \frac{1}{e_p + e_n} \tag{5.29}$$

In most cases it may be assumed that for the whole temperature range of the measurement $e_n >> e_p$ for an electron trap or $e_p >> e_n$ for a hole trap, for which this rate constant reduces to $\tau = \frac{1}{e_n}$ or $\tau = \frac{1}{e_p}$. For an electron trap using both (5.10a) and (5.7a), one obtaines:

$$e_n = \sigma_n < v_n > N_C e^{-\frac{\Delta G}{k_B T}} \tag{5.30}$$

with ΔG the Gibbs free energy difference between an electron bound to the defect and in the conduction band. Thermodynamically this Gibbs free energy difference may be expressed as $\Delta G = \Delta H - T\Delta S$, where ΔH is the enthalpy difference and ΔS the entropy difference, so that:

$$e_n = \sigma_n < v_n > N_C e^{\frac{\Delta S}{k_B}} e^{-\frac{\Delta H}{k_B T}} \tag{5.31}$$

N_C is the density of states of the conduction band, which is given by:

$$N_C = 2\left(\frac{2\pi m_e^* k_B T}{h^2}\right)^{\frac{3}{2}}. \tag{5.32}$$

Taking account of the $T^{\frac{1}{2}}$ dependence of $< v_n >$ the emission can be written as:

$$e_n = K_T T^2 e^{-\frac{E_T}{k_B T}}. \tag{5.33}$$

The parameters (K_T, E_T) are characteristic for the deep level in question and are called the signature of the level. In the DLTS method the capacitance transient with decay rate $e_n(T)$ is converted into the spectrum. We refer to e.g. the standard work of Blood and Orton [2] for a general description of the method. In our case the Fourier transform method introduced by Weiss and Kassing [3] is applied, which has been adequately described in the PhD thesis of Jochen Van Gheluwe [4]. In this chapter the emphasis will be rather on the determination of the capture cross-section σ_n, which is another important parameter of the deep level, next to the signature. It is often observed that the capture cross-section is temperature dependent and in many cases this dependence is exponential:

$$\sigma = \sigma_\infty e^{-\frac{E_\sigma}{k_B T}} \tag{5.34}$$

In that case the emission rate from an electron trap may be expressed as:

$$e_n = \sigma_\infty < v_n > N_C e^{\frac{\Delta S}{k_B}} e^{-\frac{\Delta H + E_\sigma}{k_B}} \tag{5.35}$$

The true enthalpy change is now extracted from the signature by subtracting E_σ from the apparent activation energy E_T:

$$\Delta H = E_T - E_\sigma \tag{5.36}$$

Similarly knowledge of the capture cross-section σ_∞ allows to calculate the entropy change from:

$$\sigma_{na} = \sigma_\infty e^{\frac{\Delta S}{k_B}} \tag{5.37}$$

Here σ_{na} is the apparent cross-section which is proportional to the K_T value of the signature [2]. The occurence of an activated capture cross-section has been explained by the multiphonon-assisted capture model of Henry and Lang [5].

5.3 Direct Capture measurement

To measure $c_n(T) = \sigma_n(T) < v_{th} >$ a DLTS experiment is performed with variable pulse length. This means for a fixed selected temperature T, a pulse V_p is applied for a time t_p and the transient is subsequently recorded at bias V_r between a time t_0 and $T_w + t_0$. To make it possible to measure the $\sigma(T)$ over a sufficiently large temperature range different sets of t_0 and T_w are used. The emission transient $C(t)$ after the pulse can be described as:

$$C(t) = -\Delta C(t_p) e^{-e_n(t+t_0)} + B \tag{5.38}$$

where B is the capacitance offset and t_0 dead time. This is analyzed using the Fourier component:

$$b_1 = \frac{2}{T_w} \int_0^{T_w} C(t) \sin \frac{2\pi t}{T_w} dt \tag{5.39}$$

$$b_1 = \frac{2\Delta C}{T_w} e^{-e_n t_0} \left(1 - e^{-T_w e_n}\right) \frac{\omega}{e_n^2 + \omega^2} \tag{5.40}$$

where $\omega = \frac{2\pi}{T_w}$. Inversely one may write:

$$\Delta C = b_1 \frac{T_w}{2} \frac{e^{e_n t_0}}{1 - e^{-e_n T_w}} \frac{e_n^2 + \omega^2}{\omega} \tag{5.41}$$

This means that if the emission rate is known from standard DLTS the transient amplitude ΔC can be calculated. The capture rate and σ_n are then determined from the dependence of ΔC on t_p, as will be described in the following section.

5.4 Theoretical description and assumptions following Pons [6]

A general theoretical description of the capacitance transient amplitude as a function of the filling pulse duration was published in an elaborate paper by D. Pons [6]. In this thesis work an analytical approximation based on the treatment by Pons has been developed, which is suitable to be implemented in the practical determination of the capture cross-section using DLTS and which can be used for a wide range of samples and circumstances.
In this section we will focus on some aspects in the treatment by Pons which are considered to be relevant for our case. Our analytical approximation will subsequently be described in section 5.5.
At first we will evaluate the assumptions made by Pons. These assumptions are made to treat the capture kinetics as a whole, both in the neutral semiconductor and in the Debye tails.

- The concentration of the deep traps N_T that cause the capacitance transient is negligible comparing to the free carrier concentration.

- The distribution of free carriers under reverse bias V_r or pulse V_p of the Schottky diode is completely determined by the position of the quasi Fermi level. This quasi Fermi level is constant throughout the space-

charge region and set equal to the bulk Fermi level. This assumption is only valid if the leakage current in the sample is negligible.

- The distribution of excess carriers during the pulse equilibrates sufficiently fast comparing to the time scale of capture. To have an idea of the time it takes for the excess carriers to establish equilibrium, we use the following thought experiment. We inject a distribution of excess electrons $n(x, t = t_0)$ at time t_0 in the semiconductor with relative electrical permittivity ϵ_r and electrical resistivity ρ. The Maxwell equations for this one-dimensional system give:

$$\begin{aligned} qn(x,t) &= -\epsilon_r \epsilon_0 \frac{d\mathcal{E}(x,t)}{dx} \\ j_n &= \frac{\mathcal{E}(x,t)}{\rho} \\ \frac{dj_n}{dx} &= q\frac{dn(x,t)}{dt} \end{aligned} \tag{5.42}$$

with j_n the electron current density and $\mathcal{E}$ the electrical field. This makes that the injected excess electrons will disappear and the material will return to an equilibrium situation. Finding $\rho(x,t)$ using the set of equations (5.42), the electron concentration as a function of time can be written as:

$$n(x,t) = n(x,t_0)\exp\left(-\frac{t-t_0}{\epsilon_r\epsilon_0\rho}\right) \tag{5.43}$$

Thus the Debye time constant in equation (5.43) is $\tau_D = \epsilon_r\epsilon_0\rho$ and should be smaller than the capture time constant $\tau_c = \frac{1}{c_n n_0}$. Introducing the mobility of the carriers μ_n this condition becomes:

$$\frac{\tau_D}{\tau_c} = \frac{\epsilon\sigma_n < v_n >}{q\mu_n} << 1 \tag{5.44}$$

The condition in equation (5.44) will result in a maximum value for the capture cross-section which can be allowed, set by the condition $\frac{\tau_D}{\tau_c} = 1$. To calculate σ_{max} for electron and hole traps the empirical electron μ_n and hole μ_p mobility in high purity germanium in the temperature range

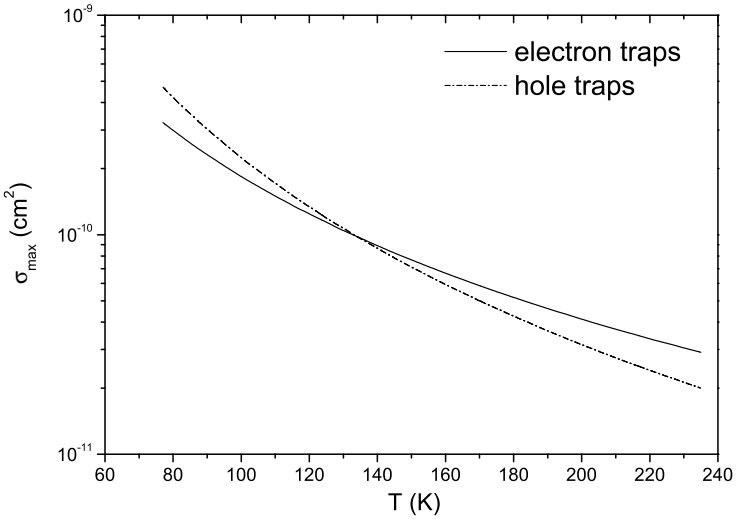

Figure 5.5: σ_{max} as a function of temperature for electron and hole traps in germanium.

$T = 77K$ to $300K$ given in Ref. [7] are used:

$$\mu_n = 4.9 \times 10^7 T^{-1.66} \frac{cm^2}{V.s} \tag{5.45}$$

$$\mu_p = 1.05 \times 10^9 T^{-2.33} \frac{cm^2}{V.s} \tag{5.46}$$

$$\tag{5.47}$$

A graph of the resulting maximum capture cross-section σ_{max} is shown in figure 5.5.

- Negligible free minority carrier concentrations everywhere in the semiconductor.

- Sufficiently high Schottky barrier
  The free electron concentration in the depletion layer of an n-type semiconductor may be written as:

$$n(x,t) = n_0 e^{\frac{qV(x,t)}{k_B T}} \tag{5.48}$$

Herein $V(x,t)$ is the electrical potential as a function of the position x within the semiconductor ($x = 0$ corresponds with the metal-semiconductor surface) and n_0 the free electron concentration in the neutral semiconductor. Using the Poisson equation the electrical potential as a function of the position x can be calculated:

$$\frac{W-x}{L_D\sqrt{2}} = -\int_{\frac{n(W)}{n_0}=\nu(W)}^{\frac{n(x)}{n_0}=\nu(x)} \frac{dz}{2z\sqrt{z-\ln(z)-1}} = \Psi\left(\frac{n(x)}{n_0}\right) \tag{5.49}$$

L_D is the Debye length given by $L_D = \sqrt{\frac{\epsilon k_B T}{q^2 n_0}}$. Herein W and x are in principle two arbitrarly chosen positions in the semiconductor and $V(W)$ and $V(x)$ the electrical potential at these positions respectively. Although we are not using the depletion approximation as in section 5.2.3 we still can use $W_{r/p} = \frac{\epsilon A}{C_{r/p}}$ as a definition for these distances. Herein $C_{r/p}$ are the high frequency capacitances at bias $V_{r/p}$. The total charge Q can be calculated by means of the Gauss law:

$$Q = \epsilon \int\int \vec{\mathcal{E}} d\vec{S} = q n_0 L_D \sqrt{2} \sqrt{e^{\frac{qV(0)}{k_B T}} - 1 - \frac{qV(0)}{k_B T}} \tag{5.50}$$

and the distance $W_{r/p}$ can be written as:

$$W = \frac{\epsilon A}{C} = \epsilon A \left(\frac{dQ}{dV}\right)^{-1} = L_D\sqrt{2}\frac{\sqrt{e^{\frac{qV(0)}{k_B T}} - 1 - \frac{qV(0)}{k_B T}}}{1 - e^{\frac{qV(0)}{k_B T}}} \tag{5.51}$$

Using equations (5.51) and (5.49) Pons [6] suggested following $\frac{n(0)}{n_0} << 1$ the universal law

$$\frac{n(W)}{n_0} = 0.55 \tag{5.52}$$

To illustrate this relation a numerical solution of equations (5.49) and (5.51) for different $\nu(0)$ is shown in figure 5.6 (a). It can be seen that $\nu(W) = 0.55$ is valid for small $\frac{n(0)}{n_0} << 1$. From this it can be seen that for $\nu(0) < 2.5 \times 10^{-2}$, $\nu(W) = 0.569$ which is within 3.6% of the proposed 0.55, thus acceptable. Because $\nu(0)$ depends on temperature T

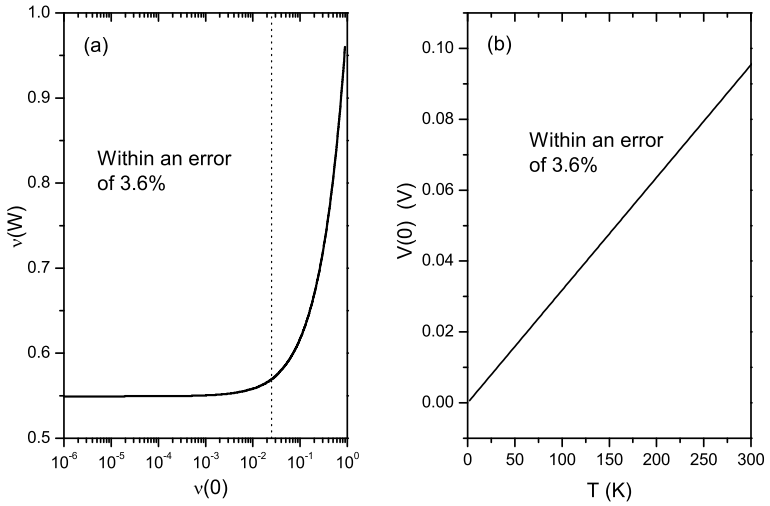

Figure 5.6: (a) Numerical integrated $\nu(W)$ as a function of $\nu(0)$ dotted line corresponds with $\nu(0) = 2.5 \times 10^{-2}$. (b) Resulted $V(0) = V_p + U_b$, which will fulfill the this condition.

and $V(0) = V_p + U_b$ and this results in a condition for the applied pulse bias. The same assumption results in:

$$V(0) = V_p + U_b > -\ln\left(2.5 \times 10^{-2}\right)\frac{k_B T}{q} \tag{5.53}$$

Because Indium on p-type and Gold on n-type germanium results in a built-in potential $U_b > 0.1V$ this assumption is fulfilled even for $V_p = 0$.

5.4.1 Capture kinetics and DLTS-signal amplitude

We have supposed that the above discussed carrier profile establishes itself sufficiently fast. This makes that a similar rate equation as used to describe the kinetics as in section 5.2.1 can be used (equation 5.1), but the capture rate $c_n n(x,t)$ becomes dependent on the position in the semiconductor and the time (filling pulse duration). Due to the absence of minority carriers, this

reduces to:

$$\frac{dn_T}{dt} = c_n n(x,t)\left(N_T(x) - n_T(x,t)\right) - e_n n_T(x,t) \tag{5.54}$$

In pulse biased configuration an integration of the Poisson equation yields

$$U_b - V_p = -\frac{q}{\epsilon}\int_0^{+\infty} x\left(n_0 - n(x,t) + N_T(x) - n_T(x,t)\right)dx \tag{5.55}$$

Because the pulse is kept constant during this filling process, the time derivative of equation (5.55) is zero and:

$$\int_0^{+\infty} x\frac{dn(x,t)}{dt}dx = -\int_0^{+\infty} x\frac{dn_T(x,t)}{dt}dx \tag{5.56}$$

From the free carrier profile equation (5.51) on can easily deduce that:

$$\frac{dW}{dt} = L_D\sqrt{2}\frac{d\Psi}{dn(x,t)}\frac{dn(x,t)}{dt} \tag{5.57}$$

Substituting equation (5.57) in the left-hand side of equation (5.56) and using the main theorem of the calculus then yields:

$$\begin{gathered}\frac{1}{\sqrt{2}L_D}\frac{dW}{dt}\int_0^{+\infty} x\left(\frac{d\Psi}{dn(x,t)}\right)^{-1}dx = \\ -\frac{1}{\sqrt{2}L_D}\frac{dW}{dt}\int_0^{+\infty}\frac{2xn}{n_0}\sqrt{\frac{n}{n_0} - 1 - \ln\frac{n}{n_0}}dx\end{gathered} \tag{5.58}$$

After using equation (5.48) as a substitution in this integral, $\sqrt{e^{\frac{qV}{k_BT}} - 1 + \frac{qV}{k_BT}}$ $dx = -\frac{L_D}{\sqrt{2}}\frac{qdV}{k_BT}$ this integral becomes:

$$-\frac{dW}{dt}\frac{q}{k_BT}\int_{-V(0)}^{-V(+\infty)} xe^{\frac{qV}{k_BT}}dV = -n_0\frac{dW}{dt}\left(W - L_D\sqrt{2}\int_{\frac{n(0)}{n_0}}^{1}\Psi(z)dz\right) \tag{5.59}$$

One can easily see that for $\frac{n(0)}{n_0} << 1$ the integral $\int_{\frac{n(0)}{n_0}}^{1}\Psi(z)dz$ becomes $\int_0^1\Psi dz$. To show that this integral is negligible during the pulse one has to show that:

$$\frac{W_p}{L_D\sqrt{2}} >> \int_{\frac{n(0)}{n_0}}^{1}\Psi(z)dz \tag{5.60}$$

Including the W_p calculated using equation (5.51) it can be seen in figure 5.7 that for $\frac{n(0)}{n_0}$ small enough this $\int_{\frac{n(0)}{n_0}}^{1}\Psi(z)dz$ is negligible. It should be noted

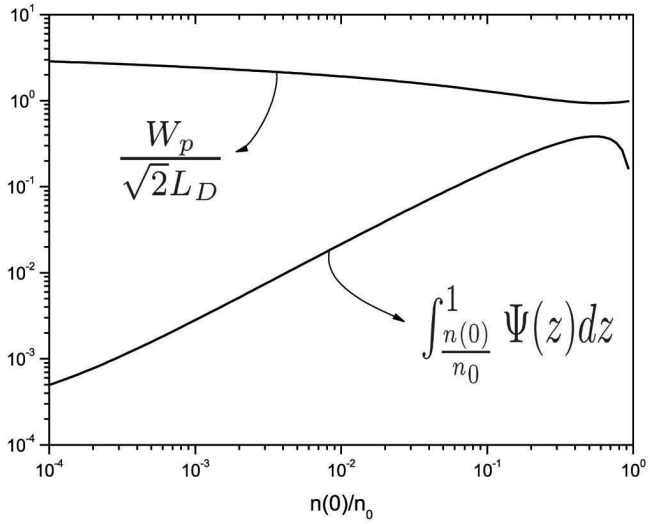

Figure 5.7: Comparing $\frac{W_p}{\sqrt{2}L_D}$ and $\int_{\frac{n(0)}{n_0}}^{1} \Psi(z)dz$

that for the integral $\Phi(z)$ the previously discussed $\frac{n(W)}{n_0} = 0.55$ was used. This makes that

$$\int_0^{+\infty} x\frac{dn(x,t)}{dt}dx = -Wn_0\frac{dW}{dt} \tag{5.61}$$

An integration over a time interval with length t then gives:

$$\int_{W_r}^{W(t)} Wn_0 dW = \int_0^{+\infty} \Delta n_T(x,t)xdx \tag{5.62}$$

Herein $\Delta n_T = n_T(x,t) - n_T(x,0)$. Integrating the left side of the equation and using the definition for the depletion depth as a function of the capacitance, one obtains:

$$\frac{1}{2}\left(\left(\frac{C_r}{C(t_p)}\right)^2 - 1\right) = \frac{1}{n_0 W_r^2}\int_0^{+\infty} N_T(x)\Delta f(x,t_p)xdx \tag{5.63}$$

The capacitance transient as a function of filling pulse duration for a negligible deep trap concentration finally becomes:

$$S(t_p) = -\frac{\Delta C(t_p)}{C_r} = \frac{1}{n_0 W_r^2}\int_0^{+\infty} N_T(x)\Delta f(x,t_p)xdx. \tag{5.64}$$

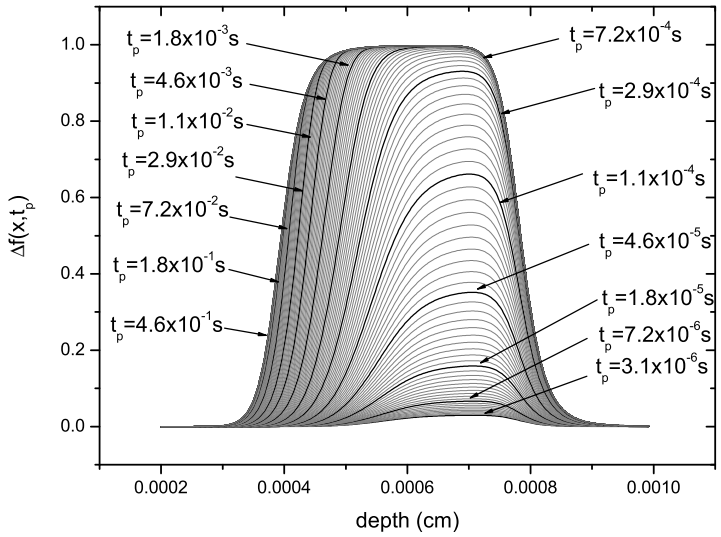

Figure 5.8: Numerical integrated $\Delta f(x, t_p)$ for different pulse durations for $n_0 = 2 \times 10^{13} cm^2$, $c_n n_0 = 10^4 s^{-1}$, $e_n = 10^2 s$, $V_r = -1V$ and $V_p = 0V$.

Herein $\Delta f = \frac{n_T}{N_T}$ represents the fractional occupation of deep levels after the pulse which can be described using the solution of the rate equation (5.2). The calculated Δf as a function of filling pulse duration for $n_0 = 2 \times 10^{13} cm^2$, $c_n n_0 = 10^4 s^{-1}$, $e_n = 10^2 s$, $V_r = -1V$ and $V_p = 0V$ is given in figure 5.8.

5.5 An analytical approximation

In this section we derive an analytical approximation to the DLTS signal (equation 5.64) that can be fitted to the DLTS signal in isothermal capture cross-section measurements. The accuracy of this approximation, independent of the filling pulse length, leads to a fitting method that can be used on a broad range of samples. Solving the detailed balance equation (5.54) for a defect trapping and emitting electrons at a position x , the fractional distribution of

defects contributing to the DLTS-signal can be written as:

$$\Delta f(x,t_p) = \left(\frac{c_n n(x)}{c_n n(x)+e_n} - f_0(x)\right)\left(1-e^{-t_p(e_n+c_n n(x))}\right) \tag{5.65}$$

Herein $f_0(x)$ is the initial occupation of the defect levels and $n(x)$ is the free carrier profile in the semiconductor material. As in Ref. [6] the distribution $\Delta f(x,t_p)$ describing the carrier contribution to the DLTS-transient is approximated by a rectangular function. While in Refs. [6] and [8] the reemission is neglected, in this work the borders of the rectangular function ($W_r - L_r$ and $W_p - L_p$, shown in figure 5.9 replace the λ from equation 5.15) and the amplitude include reemission. The amplitude Δf_{max} of $\Delta f(x,t_p)$ is set to:

$$\Delta f_{max} \approx \frac{cn_0\left(1-e^{-t_p(e_n+c_n n_0)}\right)}{cn_0+e_n} \tag{5.66}$$

Therefore the amplitude Δf_{max} and the edge of the depletion during the pulse ($W_p - L_p(t_p)$) shown in figure 5.9 are dependent of the filling pulse duration. We define ($W_p - L_p(t_p)$) as the position to which the defect levels are filled to $\frac{\Delta f_{max}}{2}$. The distance L_r is independent of the filling pulse length t_p and is set to $\lim_{t_p\to+\infty} L_p(t_p)$. Using equation (5.65) and assuming that the initial occupation f_0 is zero and n_p the free carrier concentration at $W_p - L_p(t_p)$ the problem $\Delta f(W_p - L_p, t_p) = \frac{1}{2}\Delta f$ can be reduced to finding the solution of the following set of equations:

$$\begin{aligned} F(c_n n) &= \left(1-e^{-t_p(e_n+c_n n)}\right)\left(1+\frac{e_n}{c_n n_0}\right) \\ G(c_n n) &= \frac{1}{2}\left(1-e^{-t_p(e_n+c_n n_0)}\right)\left(1+\frac{e_n}{c_n n}\right) \\ F(c_n n_p) &= G(c_n n_p) \end{aligned} \tag{5.67}$$

5.5.1 The $c_n n_1$ and $c_n n_2$ approximations to $F(c_n n) = G(c_n n)$

A numerical solution

It can be shown that the set of equations (5.67) has a single unique solution $c_n n_p$ for $c_n n > 0$. Because

$$\frac{dF(c_n n)}{dc_n n} = +\left(1+\frac{e_n}{c_n n_0}\right) t_p e^{-t_p(e_n+c_n n)} > 0 \tag{5.68}$$

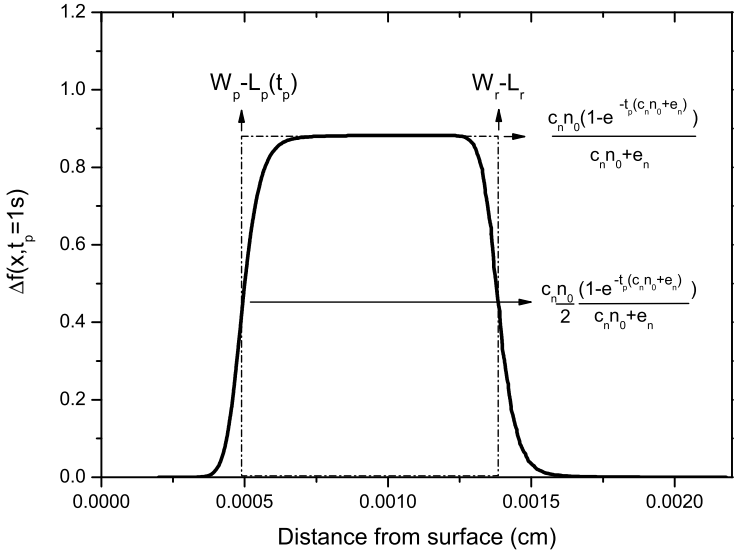

Figure 5.9: The suggested rectangular approximation to $\Delta f(x, t_p)$.

and $\frac{dG(c_n n)}{dc_n n} = -\frac{e_n}{2(c_n n)^2}\left(1 - e^{-t_p(e_n + c_n n_n)}\right) < 0$ for $c_n n > 0$, F increases while G decreases as a function of $c_n n$. It can then easily be shown that $e_n < c_n n_p < c_n n_0$, because for $n_p = n_0$ it is clear that $F(c_n n_0) = 2G(c_n n_0)$, while for $c_n n = e_n$:

$$F(e_n) = \left(1 - e^{-2t_p e_n}\right)\left(1 + \frac{e_n}{c_n n_0}\right) < 2\left(1 - e^{-t_p(e_n + c_n n_0)}\right) = G(e_n) \quad (5.69)$$

due to the chemical potential μ which is above the Gibbs-free energy G_T corresponding with the trap level $e_n = c_n n_0 exp\left(-\frac{\mu - G_T}{k_B T}\right)$, it can be seen that $e_n < c_n n_0$. This makes that there is only one single solution $c_n n_p$ between e_n and $c_n n_0$. Thus it is possible to find this solution iteratively. A first good guess $c_n n_g$ if one knows that the solution is within $c_n n_l$ and $c_n n_h$ would of course be the average:

$$c_n n_g = \frac{c_n n_l + c_n n_h}{2}. \quad (5.70)$$

Without any additional information the first lower limit $c_n n_l = e_n$ and the upper limit $c_n n_h = c_n n_0$. If this guess is too low (high) because $F(c_n n_g) <$

$G(c_n n_g)$ ($F(c_n n_g) > G(c_n n_g)$), the borders $c_n n_l$ and $c_n n_h$ can be adapted:

$$\begin{aligned} c_n n_l &= c_n n_g \quad \text{for} \quad F(c_n n_g) < G(c_n n_g) \\ c_n n_h &= c_n n_g \quad \text{for} \quad F(c_n n_g) > G(c_n n_g) \end{aligned} \tag{5.71}$$

Using equations (5.70) and (5.71) the region of the solution is clamped in halves every iterative step. The absolute error on this method can thus be written as:

$$\Delta c_n n_g = \frac{c_n n_0 - e_n}{2^N} \tag{5.72}$$

with N the number of iterations.

The $c_n n_1$-approximation

For $c_n n_p >> e_n$ an acceptable approximation for G is

$$G \approx \lim_{c_n n \to +\infty} G = \frac{1 - e^{-t_p(e_n + c_n n_0)}}{2} \tag{5.73}$$

or even better

$$G \approx G(c_n n_0) = \frac{1}{2}\left(1 - e^{-t_p(e_n + c_n n_0)}\right)\left(1 + \frac{e_n}{c_n n_0}\right) \tag{5.74}$$

But in this work a first approximation is taken as:

$$\tilde{G} = \left(1 - \frac{1}{2}e^{-t_p(c_n n_0 + e_n)} - \frac{1}{2}e^{-t_p e_n}\right)\left(1 + \frac{e_n}{c_n n_0}\right) \tag{5.75}$$

It will be shown that $\tilde{G}$ (5.75) is a better approximation for $G(c_n n_p)$ comparing to $G \approx \lim_{c_n n \to +\infty} G$ or $G(c_n n_0)$. First because:

$$\tilde{G} = G(c_n n_0) + \frac{1}{2}\left(1 - e^{-t_p e_n}\right)\left(1 + \frac{e_n}{c_n n_0}\right) \tag{5.76}$$

and thus it is clear that $\tilde{G} \geq G(c_n n_0) \geq \lim_{c_n \to +\infty} G$. Secondly it will be shown that $\tilde{G}$ is smaller than the ordinate for $F(c_n n_p) = G(c_n n_p)$. This is fulfilled if for $c_n n_0 > 0$ one obtains:

$$\tilde{G} < \max\left(G(c_n n); F(c_n n)\right) \tag{5.77}$$

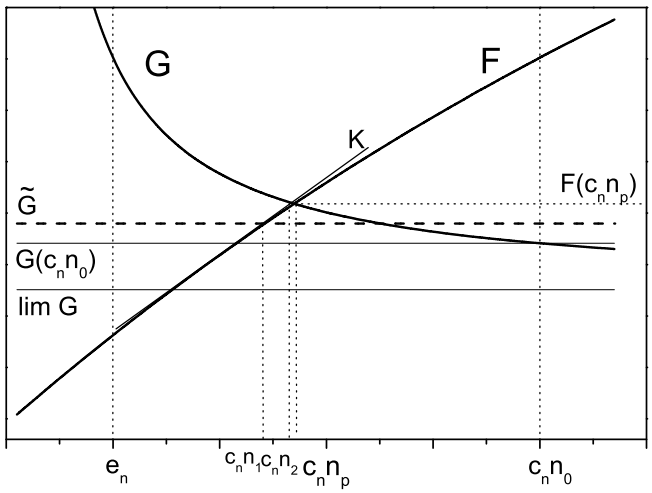

Figure 5.10: Graphical interpretation to the set of equations (5.67).

The equation $\tilde{G} < F(c_n n)$ reduces to:

$$
\begin{aligned}
\left(1-\frac{1}{2}\left(e^{-t_p(e_n+c_n n_0)}-\frac{1}{2}e^{-t_p e_n}\right)\right)\left(1+\frac{e_n}{c_n n_0}\right) &< \\
\left(1-e^{-t_p(e_n+c_n n)}\right) &\ . \quad \left(1+\frac{e_n}{c_n n_0}\right) \\
1-\frac{1}{2}\left(e^{-t_p(e_n+c_n n_0)}\right)-\frac{1}{2}e^{-t_p e_n} &< 1-e^{-t_p(e_n+c_n n)} \\
\frac{1}{2}\left(e^{-t_p(e_n+c_n n_0)}+e^{-t_p e_n}\right) &> e^{-t_p(e_n+c_n n)} \\
\ln\left(\frac{1}{2}\left(e^{-t_p(e_n+c_n n_0)}+e^{-e_n t_p}\right)\right) &> -t_p\left(e_n+c_n n\right) \\
-\frac{\ln\left(\frac{1}{2}\left(1+e^{-t_p c_n n_0}\right)e^{-e_n t_p}\right)}{t_p} &< e_n+c_n n \\
\frac{-\ln\left(\frac{1}{2}\left(1+e^{-c_n n_0 t_p}\right)\right)}{t_p} &< c_n n \qquad (5.78)
\end{aligned}
$$

While the equation $\tilde{G} < G(c_n n)$ becomes:

$$\begin{aligned}
\left(\frac{1}{2}\left(1-e^{-t_p(e_n+c_n n_0)}\right)+\frac{1}{2}\left(1-e^{-t_p e_n}\right)\right)\left(1+\frac{e_n}{c_n n_0}\right) &< \\
\frac{1}{2}\left(1-e^{-t_p(e_n+c_n n_0)}\right) &\cdot \left(1+\frac{e_n}{c_n n}\right) \\
\left[1+\frac{1-e^{-t_p e_n}}{1-e^{-t_p(e_n+c_n n_0)}}\right]\left(1+\frac{e_n}{c_n n_0}\right) &< 1+\frac{e_n}{c_n n} \\
\frac{e_n}{c_n n_0}\left[1+\chi\right]+\chi &< \frac{e_n}{c_n n} \\
\left[\frac{1}{c_n n_0}\left(1+\chi\right)+\frac{\chi}{e_n}\right]^{-1} &> c_n n \qquad (5.79)
\end{aligned}$$

with:

$$\chi(e_n t_p, c_n n_0 t_p) = \frac{1-e^{-t_p e_n}}{1-e^{-t_p(e_n+c_n n_0)}} \qquad (5.80)$$

Using (5.79) and (5.78), the condition $\tilde{G} < F(c_n n_p)$ (5.77) reduces to:

$$\left[\frac{1}{c_n n_0}\left(1+\chi\right)+\frac{\chi}{e_n}\right]^{-1} > \frac{-\ln\frac{1}{2}\left(1+e^{-c_n n_0 t_p}\right)}{t_p} \qquad (5.81)$$

or:

$$1 \geq \ln\left(\frac{2}{1+e^{-t_p c_n n_0}}\right)\left(\frac{1+\chi}{c_n n_0 t_p}+\frac{\chi}{e_n t_p}\right) = \Theta(e_n t_p, c_n n_0 t_p) \qquad (5.82)$$

The fact that for $c_n n_0 t_p > 0$:

$$\frac{d\Theta}{d(c_n n_0 t_p)} < 0 \quad \text{and} \quad \frac{d\Theta}{d(e_n t_p)} < 0 \qquad (5.83)$$

makes that the maximum of $\Theta(e_n t_p, c_n n_0 t_p)$ could be found for $\lim_{c_n n_0 t_p \to 0}$. By using the theorem of de L'Hopital:

$$\begin{aligned}
\lim_{c_n n_0 t_p \to 0} \ln\left(\frac{2}{1+e^{-t_p c_n n_0}}\right) &= 0 \\
\lim_{c_n n_0 t_p \to 0} \frac{\ln\frac{2}{1+e^{-t_p c_n n_0}}}{c_n n_0 t_p} = \frac{1+e^{-t_p c_n n_0}}{2}\frac{2}{\left(1+e^{-t_p c_n n_0}\right)^2} &= \frac{1}{2}
\end{aligned} \qquad (5.84)$$

and thus the $\lim_{c_n n_0 t_p \to 0} \Theta(e_n t_p, c_n n_0 t_p) = 1$.

An approximation can then be written as:

$$c_n n_p \approx c_n n_1 = \frac{-\ln\left(\frac{1}{2}\left(1+e^{-c_n n_0 t_p}\right)\right)}{t_p} \qquad (5.85)$$

The $c_n n_2$-approximation

A second approximation uses $c_n n_1$ as an initial result. Because

$$\frac{d^2F}{d(c_n n)^2} = -t_p^2 e^{-t_p(e_n+c_n n)}\left(1+\frac{e_n}{c_n n_0}\right) < 0 \tag{5.86}$$

the first derivative of $F(c_n n)$ is a decreasing function. A tangent $K(c_n n)$ at $c_n n_1$, with $c_n n_1 < c_n n_p$ (shown in figure 5.10) would then result in an intersection with $G(c_n n)$ at a point $c_n n_2$ with $n_1 < n_2 < n_p$. $K(c_n n)$ can be written as:

$$K(c_n n) = (c_n n - c_n n_1)\left(1+\frac{e_n}{c_n n_0}\right) t_p e^{-t_p(e_n+c_n n_1)} + \tilde{G} \tag{5.87}$$

The intersection of $K(c_n n)$ and $G(c_n n)$ can be reduced to a quadratic equation

$$(c_n n_2)^2 + b(e_n, c_n n_0, t_p)\,(c_n n_2) + c(e_n, c_n n_0, t_p) = 0 \tag{5.88}$$

with

$$\begin{aligned} c(e_n, c_n n_0, t_p) &= \frac{e^{-t_p(c_n n_0+e_n)-1}}{(1+e^{-t_p c_n n_0})\left(1+\frac{e_n}{c_n n_0}\right)e^{-t_p e_n}}\frac{e_n}{t_p} \\ b(e_n, c_n n_0, t_p) &= -c_n n_1 + \frac{2-e^{-t_p\left(2-e^{-t_p(c_n n_0+e_n)}-e^{-t_p e_n}\right)}}{(1+e^{-t_p c_n n_0})\,e^{-t_p e_n} t_p} + \frac{c(e_n, c_n, t_p)}{e_n} \end{aligned} \tag{5.89}$$

that can easily be solved in the standard way (i.e. $x = \frac{-B\pm\sqrt{B^2+4C}}{2}$). Mathematically two solutions are possible, but of course physically only the positive solution is accepted. It may be noted that if we multiply equation (5.88) with t_p^2, the quadratic equation becomes an equation in $c_n n_2 t_p$, with a factor $b(e_n, c_n n_0, t_p)t_p$ and $c(e_n, c_n n_0, t_p)t_p^2$ for terms proportional to $(c_n n_0 t_p)^1$ and $(c_n n_0 t_p)^0$ respectively. Because those two factors can then be written as a function of only $e_n t_p$ and $c_n n_0 t_p$, a solution $c_n n_2 t_p$ can be found depending only on the couple $(e_n t_p; c_n n_0 t_p)$. Increasing the pulse length for a given e_n and $c_n n_0$ corresponds then with a line parallel with direction coefficient 1.

Discussion

The relative error in terms of percentage on the concentration n_p at $W_p - L_p$ is given in figure 5.11, the exact solution was calculated by means of the numerical

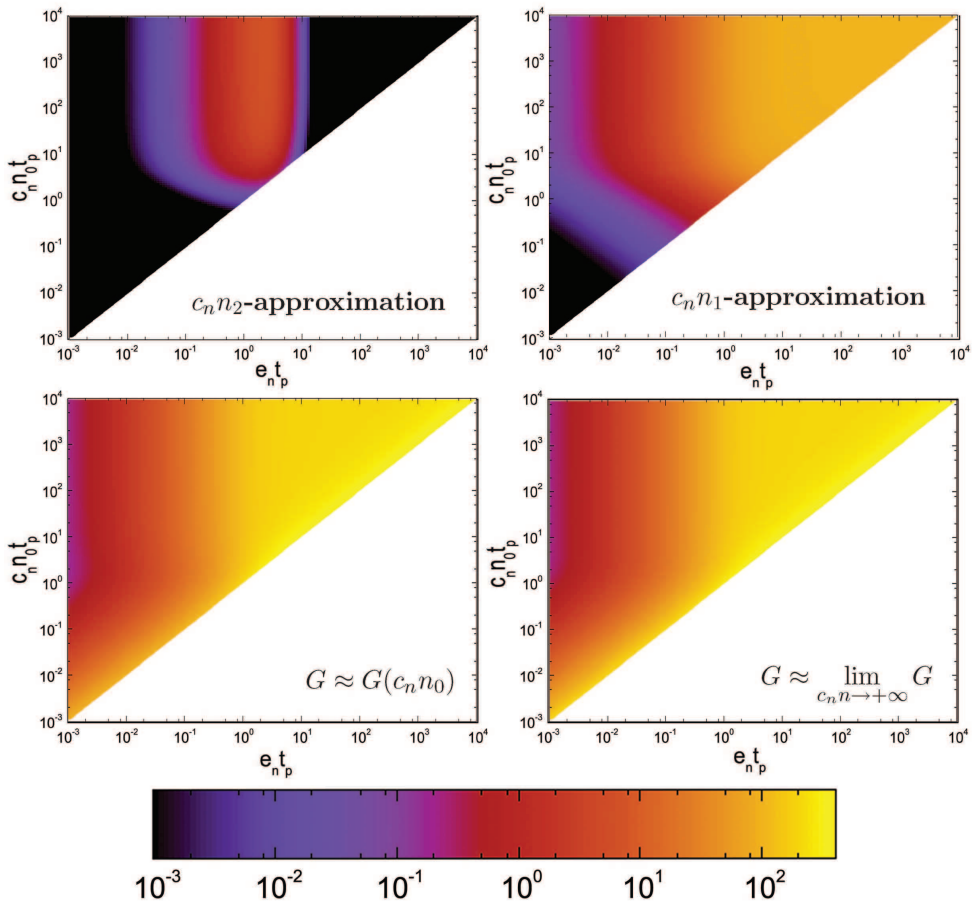

Figure 5.11: Procentual error on the concentration n_p at the position $W_p - L_p(t_p)$.

iterative solution. To have an idea on how large the maximum relative error made with this numerical method with N iterations is, one can write:

$$\frac{\Delta c_n n_g}{c_n n_p} < \frac{c_n n_0 - e_n}{e_n 2^N} = \frac{e^{\frac{\mu - G_T}{k_B T}} - 1}{2^N} < \exp\left(\frac{\mu - G_T}{k_B T} - N \ln 2\right) \tag{5.90}$$

For germanium (doped with group III acceptors or group V donors) the lowest temperature possible for a DLTS peak corresponds with the freeze out of the shallow levels, which is approximately $8K$. Similarly the maximum energy difference for the Gibbs-free energy of the trap and the chemical potential is of course the band gap, which can be approximated by $0.7eV$. Setting this as a physical upper limit to the relative error, one can see that for 2000 iterations a relative error below e^{-370} should be obtained. It could be noted that this is much too accurate for a 64-bit computer, but for this simple iterative algorithm it is not too computer time consuming.

Although this method is simple and accurate, the succession of $n_g(N)$ solutions does not form a continuous series. This makes that this solution is not ideal to implement in a stable fitting procedure.

The approximation $G \approx lim_{c_n n \to +\infty}$ assumes that $c_n n_p >> e_n$. Because $c_n n_p$ is always a fraction of $c_n n_0$ due to the decreasing free carrier profile toward the interface, this assumption is only valid for $c_n n_0 >> e_n$ and $\frac{n_p}{n_0} \approx 1$. This is valid for short filling pulses t_p.

The approximation $G \approx G(c_n n_0)$ is an improvement on the approximation using the limit. But due to the fact that $c_n n_p \approx c_n n_0$ it may be seen that this is only valid for short pulses t_p and for negligible reemission.

One of the drawbacks of both the $G(c_n n_0)$ and $\lim G$ approximation is that for large t_p the result not only has a large error but the resulted $n(W_p - L_p)$ can also be negative.

$$\lim_{t_p \to +\infty} F(0) > \lim_{t_p \to +\infty} G(c_n n_0) > \lim_{t_p \to +\infty; c_n n_0 \to +\infty} G \tag{5.91}$$

and the resulting L_p would give NaN. Although the simple model is valid for small pulses using it as a fitting formula would be not easy, because for the calculation of L_p usually due to the physical nature the logarithm should be

evaluated.

The n_1-approximation results again in a better solution, comparing to the previous approximations. Here it could be seen that the model is also valid for short filling pulses. But from equation (5.82) it follows that $n_1 = n_p$ for $\Theta(e_n t_p, c_n n_0 t_p) = 1$, which is valid for $c_n n_0 \to 0$, this makes that the n_1-approximation includes reemission for short pulses and thus is an accurate approximation for short pulses independent of the $\frac{e_n}{c_n n_0}$ relation. It could be shown that $\tilde{G} > F(0)$, which results in $n_1 > 0$ for the whole t_p range. One drawback of the n_1-approximation is that $\lim_{t_p \to +\infty} n_1 = 0$

The n_2-approximation[1] extends the n_1-approximation but is not only valid for short pulses t_p. For $t_p \to +\infty$:

$$\lim_{t_p \to +\infty} c_n n_2 = \lim_{t_p \to +\infty} c_n n_p = \frac{e_n c_n n_0}{c_n n_0 + 2e_n} \tag{5.92}$$

and thus n_2 has the same convergence behavior as n_p. Thus the main difference between n_1 and n_2 is the limit for $t_p \to +\infty$. n_1 is improved by approximating $F(c_n n)$ by a tangent $K(c_n n)$, this is of course always an improvement, but the more $F(c_n n)$ can be approximated by a straight line the more significant this improvement is. And this is of course the case for long filling pulses t_p, where the exponential depedence in F is negligible. Therefore it may be seen from figure 5.11 that for intermediate pulse lengths the error has a maximum. All four approximations shown in figure 5.11 have one similar property they all underestimate the n_p-value, and thus from the error in terms of percentage can be deduced how strong this underestimation is.

5.5.2 Approximation to the carrier concentration profile

Once the carrier concentration n_p is known at the position $W_p - L_p(t_p)$, the position can be calculated. For this an inverse function of the carrier concen-

[1] A discussion comparing the n_2-approximation with $S(t_p)$ equation (5.64) will be given later.

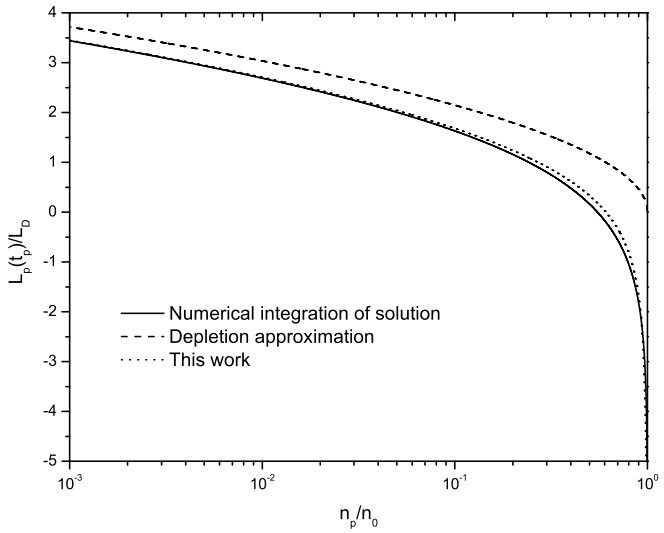

Figure 5.12: Approximations to the carrierprofile.

tration is needed. Figure 5.12 shows:

$$\frac{L_p}{L_D} = -\frac{2\ln\left(\frac{n_p}{n_0}\right)+1}{\sqrt{-2\ln\left(\frac{n_p}{n_0}\right)}} \tag{5.93}$$

This function is the inverse of:

$$\frac{n(L)}{n_0} = \exp\left(-\frac{1}{4}\left(\frac{L}{L_D\sqrt{2}}+\sqrt{\frac{L^2}{2L_D^2}+1}\right)^2\right) \tag{5.94}$$

which is used in this work as an approximation to the numerically integrated solution of equation (5.49) as an improvement with respect to the depletion approximation.

5.5.3 The inclusion of the $N_T(x)$ profile

Using the rectangular approximation with the above defined boundaries the integral in equation (5.64) becomes:

$$S(t_p) = -\frac{\Delta C(t_p)}{C_r} = \frac{c_n n_0}{n_0 W_r^2} \frac{\left(1 - e^{-t_p(e_n + c_n n_0)}\right)}{c_n n_0 + e_n} \int_{W_p - L_p(t_p)}^{W_r - L_r} N_T(x) x dx$$
$$= -\frac{c_n n_0}{n_0 W_r^2 \left(e_n + c_n n_0\right)} \left(1 - e^{-t_p(e_n + c_n n_0)}\right) I(t_p) \quad (5.95)$$

Integrating $I(t_p) = \int_{W_p - L_p(t_p)}^{W_r - L_r} N_T(x) dx$ by parts it can be written as:

$$\begin{aligned} I(t_p) &= (W_r - L_r)\, \bar{N_T}(W_r - L_r) - (W_p - L_p) \bar{N_T}(W_p - L_p) \\ &- \underline{N_T}(W_r - L_r) + \underline{N_T}(W_p - L_p) \quad (5.96) \\ \bar{N_T}(y) &= \int_0^y N_T(x) dx \quad (5.97) \\ \underline{N_T}(y) &= \int_0^y dz \int_0^z N_T(x) dx \quad (5.98) \end{aligned}$$

For a slowly varying defect profile around W_p these integral functions can be expanded using a Taylor series:

$$I(t_p) = (W_r - L_r)\bar{N_T}(W_r - L_r) - \underline{N_T}(W_r - L_r) + \underline{N_T}(W_p) - (W_p - L_p)^2 \frac{N_T(W_p)}{2} \quad (5.99)$$

And thus $I(t_p)$ can be written as:

$$I(t_p) = \int_{W_p}^{W_r - L_r} N_T(x) x dx + W_p L_p N_T(W_p) - L_p^2 \frac{N_T(W_p)}{2} \quad (5.100)$$

which makes that the amplitude of the DLTS-signal reduces to:

$$\begin{aligned} \frac{\Delta C(t_p)}{C_r} &= -\frac{c_n n_0}{(c_n n_0 + e_n)} \left(1 - e^{-t_p(e_n + c_n n_0)}\right) \quad (5.101) \\ &\cdot \left(-a_1 \left(\frac{L_p(t_p)}{L_D}\right)^2 + a_1 a_2 \left(\frac{L_p(t_p)}{L_D}\right) + a_3\right) \\ a_1 &= \frac{L_D^2}{2 n_0 W_r^2} N_T(w_p) \quad (5.102) \\ a_1 a_2 &= \frac{W_p L_D}{2 n_0 W_r^2} N_T(W_p) \quad (5.103) \\ a_3 &= \frac{1}{n_0 W_r^2} \int_{W_p}^{W_r - L_r} N_T(x) x dx \quad (5.104) \end{aligned}$$

5.5.4 Properties of the analytical approximation: a discussion

Figure 5.13 shows the relative error percentage for the analytic approximation in equation (5.101-5.104) comparing to the numerically integrated solution Eq. (5.64). This error is calculated for $W_r = 28.2 \times L_D$ and $W_p = 6.7 \times L_D$. According to equation (5.107) this corresponds for example with $T = 155K$, $U_r = 1V$ and $U_D = 0.3V$. From figure 5.13a it is seen that using the n_2-approximation the whole range is covered within an error of 2%. Figure 5.13 c shows that the approximation proposed by Stievenard et al. [8] is only valid for $e_n << c_n n_0$. Although is was suggested that the latter approximation is useful for $t_p > \frac{1}{c_n n_0 + e_n}$ the border of the rectangular function can be written as (Eq. 18 in Ref. [8]):

$$L_p^2(t_p) = 2L_D^2 \ln\left(\frac{c_n n_0 t_p}{\ln\left(\frac{2}{1+e^{-e_n t_p}}\right)}\right) \tag{5.105}$$

It follows from equation (5.105) that for $t_p \to +\infty$, L_p diverges to $+\infty$. This result may be compared to equation (5.64), which for $t_p \to +\infty$ reduces to:

$$\lim_{t_p=+\infty} \frac{\Delta C(t_p)}{C_r} \propto \int_0^\infty \left(\frac{c_n n(x)}{e_n + c_n n(x)} - \frac{c_n n_r(x)}{e_n + c_n n_r(x)}\right) x dx \tag{5.106}$$

Here $n(x)$ and $n_r(x)$ are the carrier profiles during filling pulse and reverse bias respectively. From equation (5.106) and describing the carrier profiles using equation (5.94), one can show that the integral converges for $t_p \to +\infty$. (The convergence is proved in appendix A.) From the set of equations (5.67) it follows that for $t_p \to +\infty$ the carrier concentration at position $W_p - L_p$ becomes $\frac{e_n n_0}{c_n n_0 + 2e_n}$ which results in a defined value for L_p. This result is similar for the n_2-approximation to Eq. (5.67). Because for $t_p \to +\infty$, $\tilde{G} = 1 + \frac{e_n}{c_n n_0}$ and $c_n n_1 = 0$ this results in a tangent $K(c_n n) = 1 + \frac{e_n}{c_n n_0}$, which has an intersection with $G(c_n n)$ for $n_2 = \frac{e_n n_0}{c_n n_0 + 2e_n}$. It may therefore be emphasized that the n_2-approximation is suitable for long pulse durations, which are applicable to a wide range of dopant concentrations.

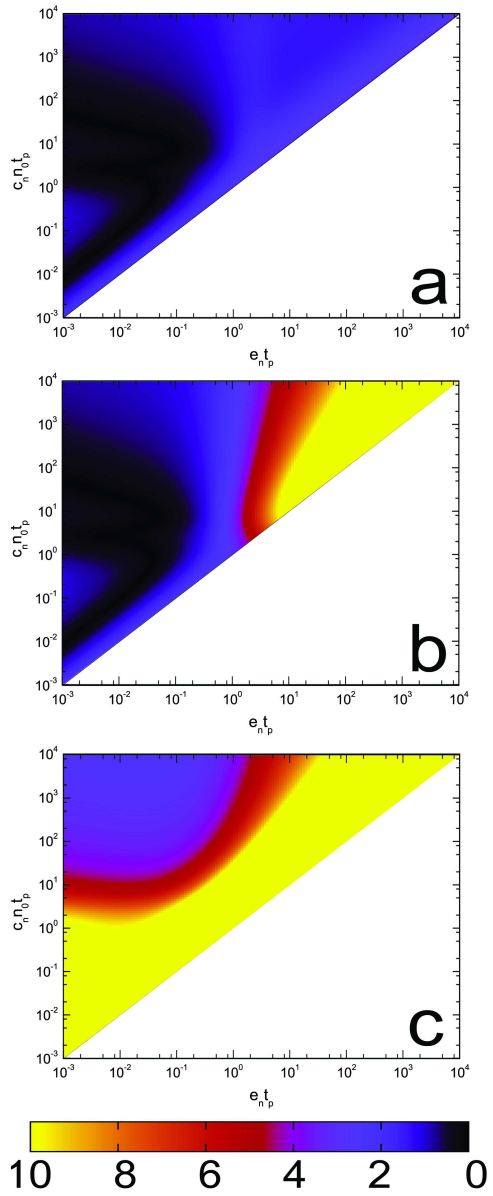

Figure 5.13: Colour map of the percentage error of (a) n_2-approximation (b) n_1-approximation and (c) approximation Ref. [8], comparing to equation (5.64) numerically integrated for $W_r = 28.2 \times L_D$ and $W_p = 6.7 \times L_D$. Yellow correspond with 10 or more.

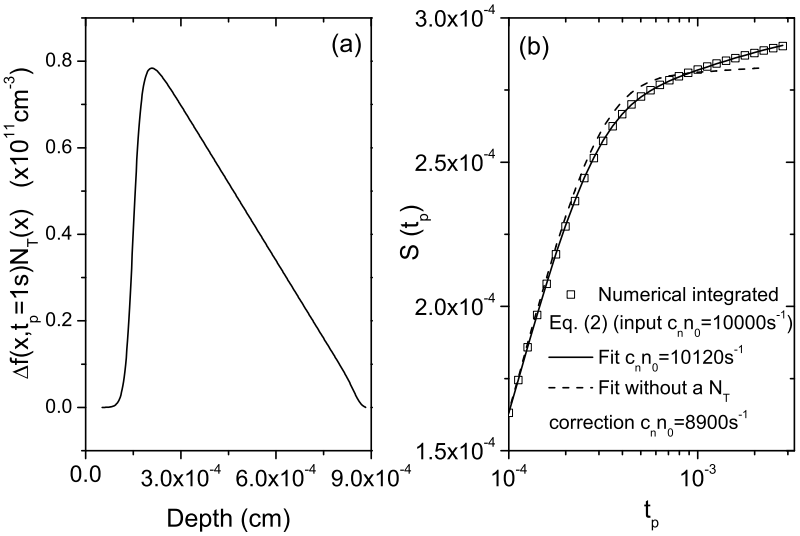

Figure 5.14: (a) Spatial distribution of deep levels contributing to the DLTS-signal for a linear $N_T(x)$ deep level profile. (b) Transient amplitude function $S(t_p)$ fitted with and without $N_T(x)$ correction. The input capture rate corresponds with $c_n n_0 = 10000s^{-1}$. A fit including a defect profile correction (full line) gives $c_n n_0 = 10120s^{-1}$ while not including this correction (dashed line) would give $c_n n_0 = 8900s^{-1}$.

The influence of a defect level profile was included using a Taylor series expansion of the L_p dependent integrals. And thus it is argued that the a_1 fitting parameter is proportional to the defect concentration N_T at W_p . It is clear that some assumptions concerning the defect profile between $W_p - L_p(t_p)$ and W_p are needed. Due to the t_p dependence of the distance L_p the inclusion of an unknown position dependent trap profile in this range would result in a DLTS-signal proportional to the integral function $I(t_p)$, with an unknown t_p dependence and thus impossible to include in a fitting procedure. On the other hand, the DLTS technique measures close to the metal-semiconductor interface and the defect profile within the DLTS measuring range often contains a non-negligible position dependence. The inclusion of the unknown defect profile in the analytical approximation of the DLTS-signal (5.104) can be interpreted as different approximation for two regions. A first region between $W_r - L_r$ and W_p, which has a border independent of the filling pulse and thus the full $N_T(x)$ dependence can be included in the a_3 fitting parameter. The remaining part of the region, where the DLTS-signal originates from, thus contains the t_p dependent border. Because $N_T(x)$ is unknown the inclusion of additional assumptions on the profile within this variable part of the region, would be no improvement on the deduced capture rate. It is therefore considered justified to take the trap concentration in the region between $W_p - L_p(t_p)$ and W_p constant. This concentration is included as a fitting parameter via the proportionality with the parameter a_1. Although from Taylor series expansion it is argued that this concentration can be approximated by the concentration N_T at position W_p , the resulted N_T calculated from the fitted a_1 parameter may differ from $N_T(W_p)$. To analyse the influence of a defect profile on the resulting capture cross-section, different signal amplitudes have been numerically generated including a trap-level profile $N_T(x)$. Figure 5.14 illustrates the case of a linearly descending profile. Figure 5.14 a shows the effect on the function under the integral in equation (5.64). Figure 5.14 b shows a detail of the numerical DLTS-signal (Eq. (5.64)) fitted with and without the $N_T(x)$ correction. From the fitted $c_n n_0$-values it may be seen that this $N_T(x)$ correc-

tion is a significant improvement comparing to the fit without this correction. It is clear that for a descending profile without $N_T(x)$ correction, the effect of slow capture will be underestimated, and thus the fitted capture rate will be underestimated too.

5.6 The fitting procedure and the accuracy of this method

From equations (5.102) and (5.103) it can be seen that the a_2 parameter can be written as a function of the applied pulse bias and the intercept U_D on the bias axis of the Mott-Schottky plot:

$$a_2 = \frac{a_1 a_2}{a_1} = \frac{2W_p}{L_D} = 2\sqrt{\frac{2\epsilon\,(V_p + U_D)}{qn_0}\frac{e^2 n_0}{\epsilon k_B T}} = \sqrt{\frac{8\,(U_p + U_D)}{k_B T}}. \qquad (5.107)$$

From this it can be seen that a_2 can be set as a fixed value during the fitting procedure, because the extrapolated barrier-height U_D can be deduced from the Mott-Schottky plot. Both the temperature T and the pulse bias U_p are tuned parameters for the measurements. The combination of equations (5.107) and (5.104) can be used as an analytic equation for the DLTS-signal in function of the applied filling pulse duration. This was implemented in a fitting routine using Levenberg-Marquardts algorithm, with $c_n n_0$, a_1 and a_3 as adjustable parameters.

The Levenberg-Marquardt algoritm

The set equations (5.104) and specially the $c_n n_0$ dependence show a strong non-linearity. Therefore the Levenberg-Marquardt method was chosen, which has become the standard method for non-linear least square problems. This was implemented in a Windows fitting tool written in Visual Basic, a screen shot is shown in figure 5.15.

This software-tool also includes a routine to estimate the error made by the fitting. This will be discussed more in detail for the example of the Hf-E1 level.

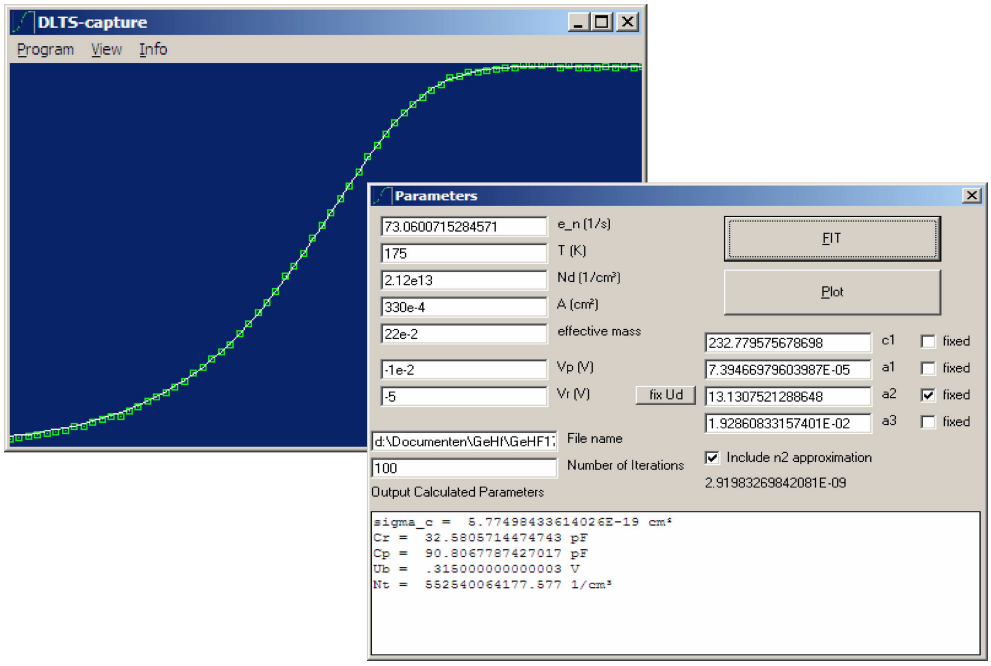

Figure 5.15: Print screen of the resulted software-tool, which was used to fit the carrier capture-cross section.

5.7 An application to transition metal impurity levels in germanium.

5.7.1 DLTS spectra

The electronic properties of metal impurities in germanium have been intensively studied about 50 years ago, mainly using Hall effect and photo-electric measurements. Summaries of the results may be found in Refs. [1, 9–11]. A general picture that emerges from those studies is that transition metals in germanium predominantly form multiple-acceptor centres corresponding with several deep levels in the band gap, in agreement with occurrence of the impurities on substitutional sites. Since those early studies DLTS has become available as the preferential technique to study deep level centres in semiconductors. Besides the higher versatility and better energy resolution compared with Hall-effect, the method is also more suitable to investigate deep levels in

a thin layer below the surface, as in impurity diffused or implanted samples. A review of DLTS data concerning metals in germanium may be found in Refs [11, 12]. Recently our research group has been involved in the study of germanium wafers implanted with different metal impurities (the GEWEL project). Distinct DLTS spectra were observed in n- and p-type samples implanted with one of the TM's: Hf, Ni, Ti, Cr, Co or Fe. Summaries of the results may be found in Refs [13, 14]. In this chapter we focus on the accurate determination of the capture cross section from direct capture experiments. These measurements are mainly concerned with the levels in the n-type material, where one level is observed for each metal studied. The DLTS spectra of these levels, which have been labelled M-E1 (with M the identity of the metal) are summarised in figure 5.16; the corresponding Arrhenius diagrams are shown in figure 5.17. The E1-levels have been assigned to $M^{3-/2-}$ or $M^{2-/-}$ acceptor levels. As may be expected for similar levels, the electron capture cross-sections are rather low so that they are accessible for direct capture experiments. In most cases the capture is thermally activated, typical for phonon-assisted capture. In some cases also hole capture in the p-type sample could be measured and these results will also be included.

5.7.2 Capture-cross-sections of transition metals in germanium.

Hafnium

The Arrhenius diagram of the Hf-E1 yields a signature ($K_T = 8.7\times10^7 K^{-2}s^{-1}$; $E_T = 0.367eV$). No other peak between freeze-out of the Sb shallow donor and 200K was observed. Figure 5.18 shows the Mott-Schottky plot at 175.4K. From this measurement the free carrier concentration in the neutral semiconductor n_0 and the extrapolated U_D are deduced. To lower the contribution of the Debye free carrier tail, $V_r = -5V$ and $V_p = -0.01V$ were used. Figure 5.19 (a) shows the free carrier density in the neutral semiconductor as a function of temperature. No strong variation in the n_0 concentration is observed, and thus the correction for $n_0(T)$ will have no effect on the temperature dependence

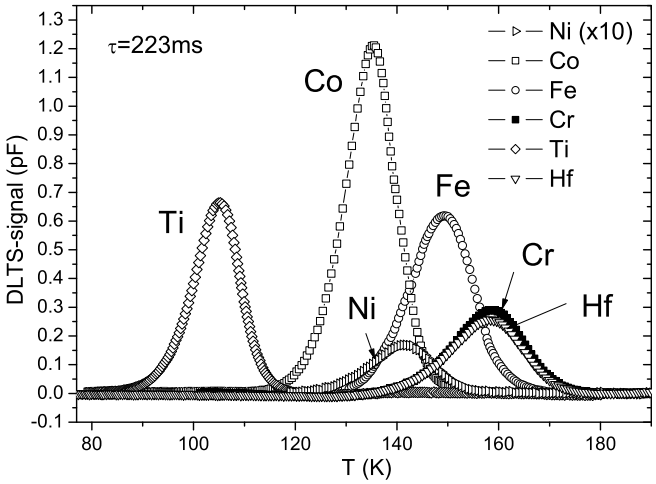

Figure 5.16: DLTS spectrum of n-type germanium implanted with the transition metal impurities studied in this section; the peaks correspond with the E1-level of the impurities

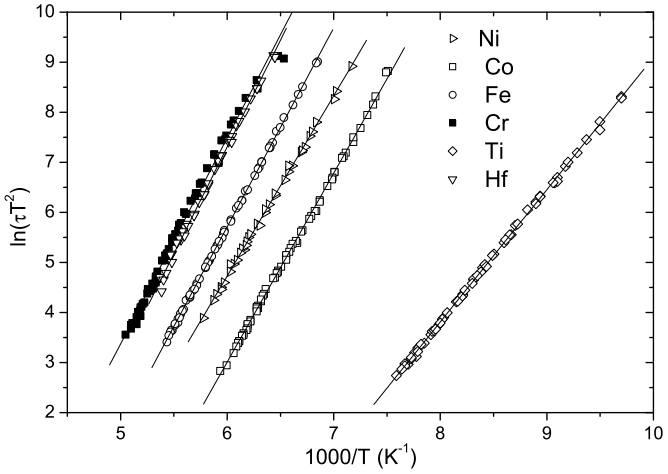

Figure 5.17: Arrhenius diagrams of the E1-levels with DLTS-spectrum in fig. 5.16.

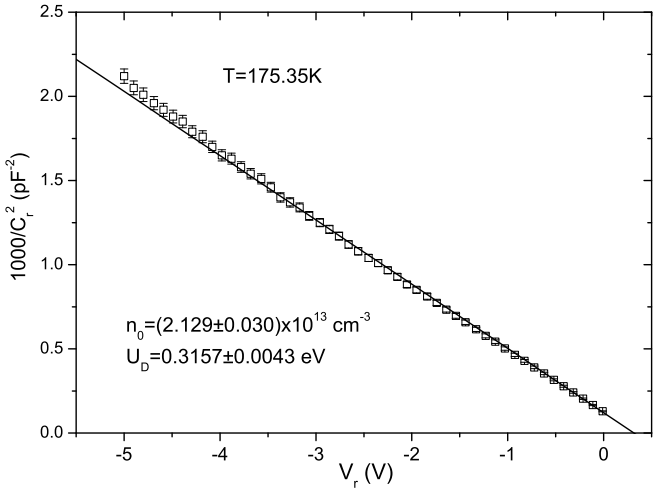

Figure 5.18: Mott-Schottky plot for the n-Ge:Hf sample at $T = 175.4K$, from which U_D and the free-carrier concentration in the neutral semiconductor is deduced.

of the capture cross section $\sigma(T)$. Figure 5.19 (b) shows the temperature dependence of U_D, using the equation (5.107). This results in an a_2-parameter, which is also shown in the figure. It can be seen that a_2 is fixed for each temperature but the value is a result of a linear fit to experimental values, assuming the error $0.1pF$ on the capacitance and $0.1K$ on the temperature, this gives an error Δa_2 on the a_2-parameter. To check the influence of the variation in a_2 parameter on the fitted capture rate $c_n n_0$, the experimental data was fitted for different a_2 parameters. Figure 5.20 shows the effect of the variation of the a_2 parameter on the fitted $c_n n_0$ for the n-Ge:Hf at 175.4K. The variation in a_2 between the error marges labeled $a_2^{\max}$ and $a_2^{\min}$ results in a variation in $\Delta^{a_2} c_n n_0 = 0.075 s^{-1}$.

An example of the fitted DLTS-signal as a function of filling pulse length is shown in figure 5.21. In this fit the n_2-approximation was used. The necessity of using this approximation is demonstrated in figure 5.22, were the procentual error on the n_p-concentration was given for the experimental $(e_n t_p; c_n n_0 t_p)$

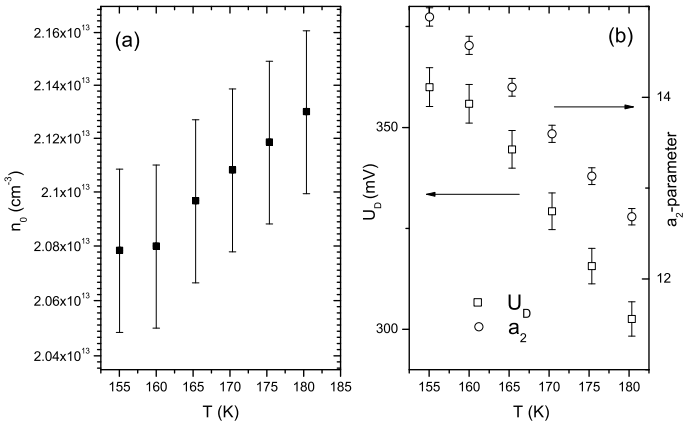

Figure 5.19: (a) The temperature dependence of the free carrier density in the neutral semiconductor n_0. (b) The temperature dependence of the extrapolated barrier height U_D and the resulted a_2 parameter.

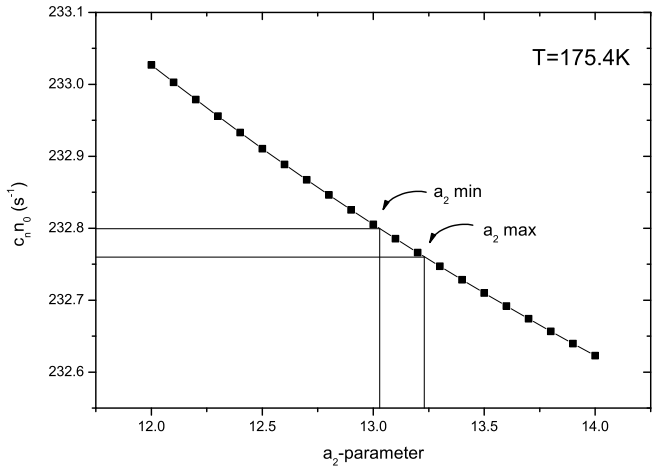

Figure 5.20: The fitted $c_n n_0$ dependence in n_2-approximation of the a_2 parameter for n-Ge:Hf at 175.4K.

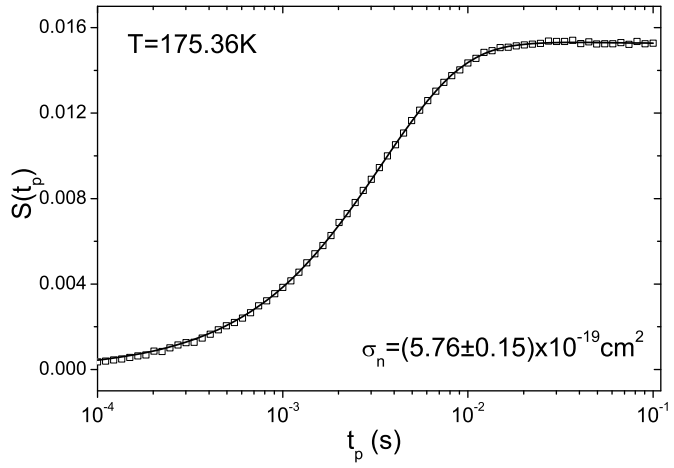

Figure 5.21: Experimental and fitted DLTS-signal $S(t_p)$ as function of filling pulse duration t_p for Hf-E1 at 175.4K

couples. The white line corresponds with the couples for $t_p = 10^{-4} \rightarrow 10^{-1}$. Not only the approximation that was used or the variation on the a_2 parameter, but also the noise or the variation on the measured DLTS-signal will influence the accuracy of the capture rate $c_n n_0$. To estimate the error on the capture cross section, 2000 functions $S(t_p)$ with generated random noise with the same standard deviation as the original signal, have been fitted. The error was then calculated from the standard deviation of the fitted Gauss-distribution to the resulted $c_n n_0$ distribution:

$$\Delta c_n n_0 = \sqrt{\sum_{i=1}^{2000} \frac{\left(c_n n_0^i - \sum_{j=1}^{2000} \frac{c_n n_0^j}{2000} \right)^2}{1999}} \tag{5.108}$$

Figure 5.23 shows an example of the resulted $c_n n_0$-distribution for 2000 fits generated with the same standard deviation as the fit shown in figure 5.21. The error induced by the error on the a_2-parameter is negligible comparing to the error due to the deviation of the fit to the experimental data. This deviation on the fit is not only due to the noise on the measurement but also includes the approximations made in the model (n_2-approximation).

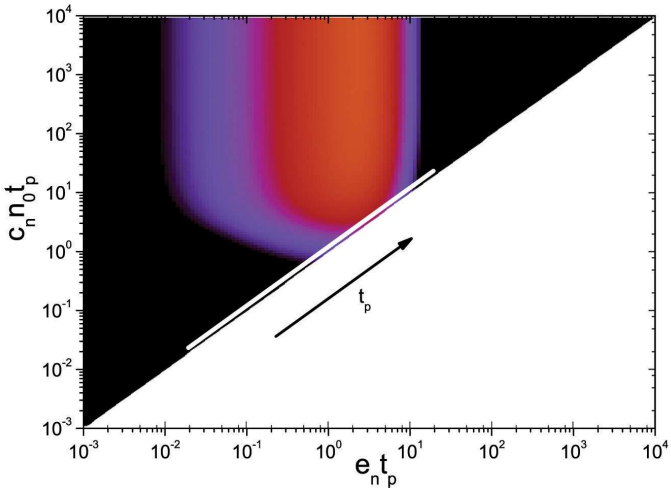

Figure 5.22: The procentual error in n_2 approximation of n_p, white line corresponds with the value $(e_n t_p; c_n n_0 t_p)$ for the Hf-E1 level at 175.4K, data shown in figure 5.21.

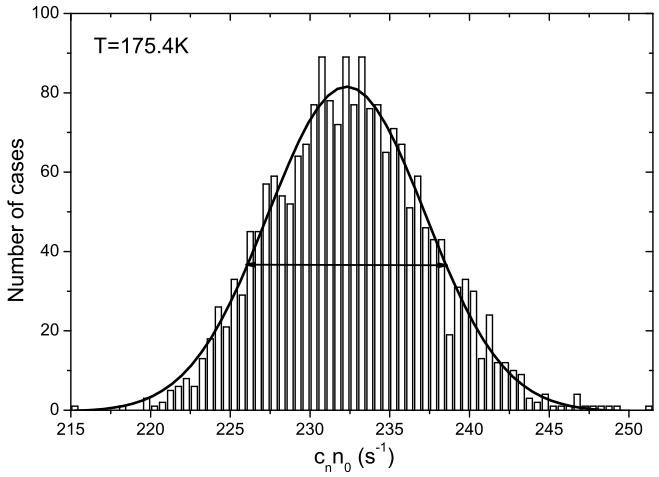

Figure 5.23: Distribution of $c_n n_0$ for the level Hf-E1 at 175 using 2000 simulated signals with Gaussian noise. The width of the Gauss curve gives the error on $c_n n_0$.

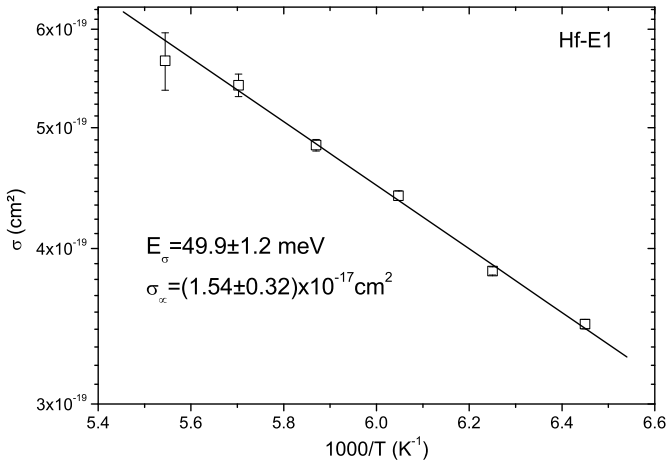

Figure 5.24: Arrhenius diagram for the electron capture cross-section of the Hf-E1 level.

The procedure is then repeated at different temperatures, resulting in a temperature dependence of capture cross-section of Hf-E1. As may be seen in figure 5.24 this dependence is well described by an exponential law (5.34) typical of multiphonon assisted capture. The fitted parameters are:

$$\sigma_\infty = 1.54 \pm 0.33 \times 10^{-17} cm^2$$

$$E_\sigma = 49.9 \pm 1.2 meV$$

From these parameters and the signature of the level the following entropy and enthalpy values for electron emission from the level are obtained:

$$\Delta S = 7.59 \pm 0.42 k_B$$

$$\Delta H = 0.318 \pm 0.004 eV$$

Nickel

The Arrhenius diagram of the Ni-E1 level yields a signature ($K_T = 2.2 \times 10^7 K^{-2} s^{-1}; E_T = 0.310 eV$). Not only the electron trap but also the hole trap

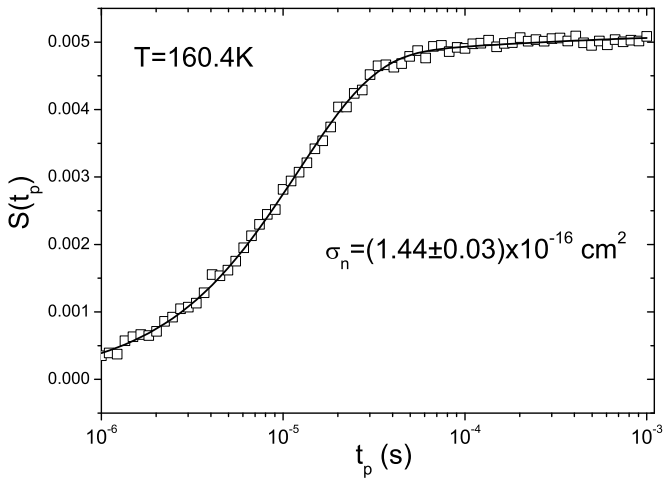

Figure 5.25: Measured and fitted DLTS-signal as a function of filling pulse duration for Ni-E1.

could be observed in the n-type sample due to the injection of minority carriers using a forward pulse.

Due to the significant lower Ni concentration in n-Ge:Ni, comparing to the Hf concentration in n-Ge:Hf discussed in the previous paragraph, a lower signal to noise ratio was obtained for these samples. The $S(t_p)$ dependence for the Ni-E1 level at 160.4K is shown in figure 5.25, with fitted value $\sigma_n = 1.44 \pm 0.03 \times 10^{-16} cm^2$.

The temperature dependence $\sigma_n(T)$ is shown in figure 5.26. Only a weak temperature dependence is observed in this case. The corresponding entropy and enthalpy values extracted from the signature are:

$$\Delta S = 3.65 \pm 0.38 k_B$$

$$\Delta H = 0.309 \pm 0.003 eV$$

The value of ΔH enthalpy change is in fair agreement with the energy $E_C - 0.30eV$ observed in Hall-effect measurements [9] where it was assigned to the $Ni^{2-/-}$ transition.

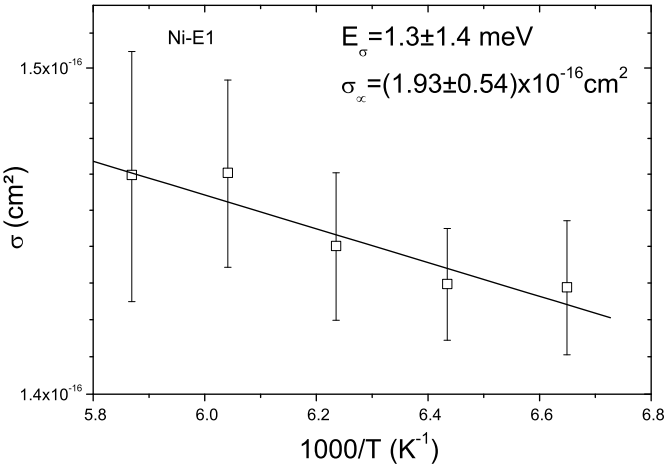

Figure 5.26: Arrhenius diagram for the capture cross-section of the Ni-E1 level.

We compare the capture cross section $\sigma(T)$ obtained here with the values published by different other authors. Kotina et al. [15] published $\sigma_n = 1.8 \times 10^{-14} cm^2$, but did not apply an entropy correction, so this value has to be compared with the apparent capture cross-section deduced from the K_T-value. The very good correspondence of the emission signature of this work compared with the values obtained by Kotina et al. means that also both apparent cross-sections are in good agreement. Here we find $\sigma_{na} = 7.5 \times 10^{-15} cm^2$. G. Huylebroeck et al. [16] obtained $\sigma_n = 4 \times 10^{-18} cm^2$ at 165K from direct capture measurements using Ni-diffused samples, a much lower value than found in our experiments. It should be mentioned however that in reference [16] the Ni-E1 peak overlaps with Cu-E1, so that a less accurate value of σ may be expected. On the other hand the capture cross section was fitted using an exponential model and neglecting slow capture, which would result in an underestimation of the capture cross-section. Another value for σ_n obtained by Pearton [17] is not taken into consideration since it probably concerns a different defect [16]. Finally two other studies concerning the $Ni^{2-/-}$ level in germanium may be mentioned. Wertheim [18] obtained a value $\sigma_n = 6 \times 10^{-16} cm^2$ independent of

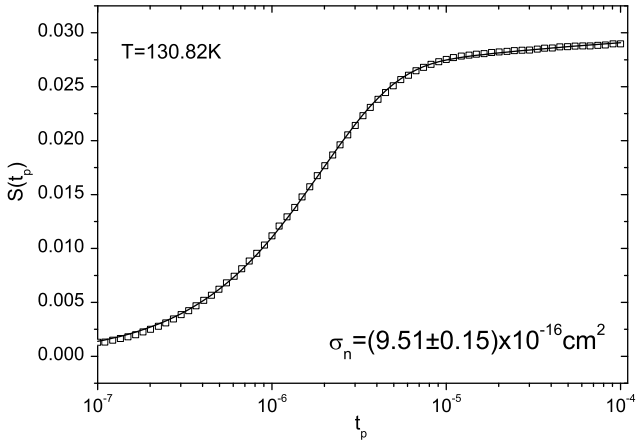

Figure 5.27: Measured and fitted DLTS-signal as a function of filling pulse duration for Co-E1.

temperature, in reasonable agreement with our data. Belyaev and Miselynk on the other hand also observed a weak temperature dependence, however with a σ_n value in the $10^{-18}cm^2$ range [19]. The reason for the discrepancy in the magnitude is unclear.

Cobalt

The signature of the Co-E1 level was determined as: ($K_T = 3.3 \times 10^8 K^{-2}s^{-1}$; $\Delta E_T = 0.325eV$). The DLTS-signal $S(t_p)$ as a function of filling pulse duration was fitted for different peak temperatures, an example of the measurement and fitted curve is shown in figure 5.27. The Arrhenius diagram for the capture-cross-section is shown in figure 5.28, the fit yields:

$$\Delta E_\sigma = 9.83 \pm 0.57meV$$

$$\sigma_\infty = (2.29 \pm 0.26) \times 10^{-15}cm^2$$

It may be emphasized that the distinct observation of a similar small activation energy is only possible using the fitting method presented in this chapter.

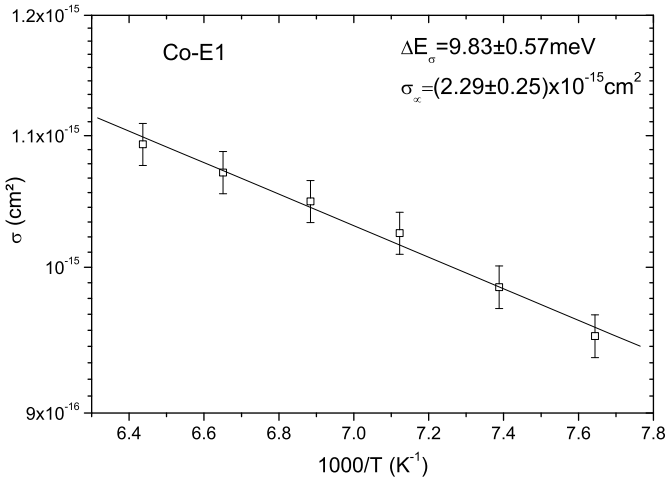

Figure 5.28: Arrhenius diagram for the electron capture cross-section of the Co-E1 level.

Using the standard method based on an $1-e^{-c_n n_0 t_p}$ dependence, no thermally activated trend can be discovered. Using the signature for the emission the following entropy and enthalpy change are obtained:

$$\Delta S = (3.93 \pm 0.17) k_B$$

$$\Delta H = (315.3 \pm 1.6) meV$$

The enthalpy corresponds very well with the value observed $E_C - 0.31eV$ by means of Hall experiments [9].

In p-type Co-implanted Ge two hole traps could be observed: $Co-H1(K_T = 6.8 \times 10^8 K^{-2}s^{-1}; E_T = 0.086eV)$ and $Co-H2(K_T = 1.7 \times 10^7 K^{-2}s^{-1}; E_T = 0.254eV)$. The temperature dependence of the corresponding capture cross-sections is shown in figure 5.29. The dependencies can be fitted using the following trend:

$$\sigma_p = \frac{\alpha 1000}{T} + \beta \tag{5.109}$$

with the parameters α and β are:

$$\alpha(Co-H1) = 8.41 \pm 0.84 \times 10^{-16} cm^2 K \quad \beta(Co-H1) = 1.92 \pm 0.20 \times 10^{-14} cm^2$$

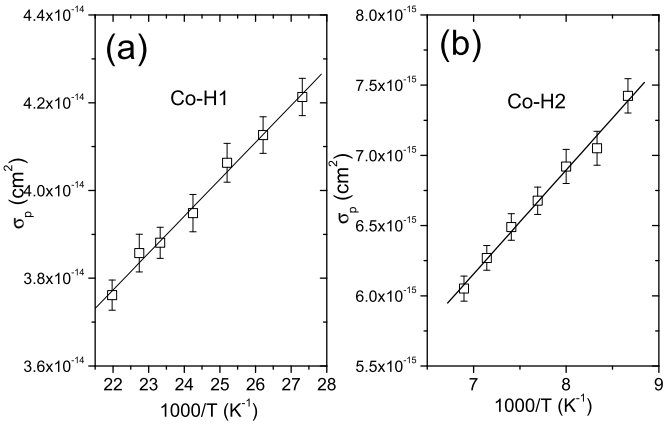

Figure 5.29: Diagram showing the capture cross-section as a function of temperature for the (a) Co-H1 and (b) Co-H2 level.

$$\alpha(Co-H2) = 7.40 \pm 0.68 \times 10^{-16} cm^2 K \quad \beta(Co-H2) = 9.7 \pm 5.3 \times 10^{-16} cm^2$$

Correction of the emission data for this capture cross-section has been done using an Arrhenius plot of $\ln \tau T^2 \sigma_n$ as a function of $\frac{1000}{T}$ as shown in figure 5.30. The following entropy and enthalpy change are then obtained:

$$\Delta S = 3.14 \pm 0.66 k_B \qquad \Delta H = 86.4 \pm 2.5 meV \qquad \text{Co} - \text{H1}$$

$$\Delta S = 1.39 \pm 0.22 k_B \qquad \Delta H = 260.8 \pm 2.6 meV \qquad \text{Co} - \text{H2}$$

The enthalpy values may be compared with the Hall-effect data $E_v + 0.09eV$ and $E_v + 0.25eV$ [20].

Iron

For iron implanted n-type germanium also one single electron trap Fe-E1 could be observed, with a signature ($E_T = 0.342eV; K_T = 7.5 \times 10^7 K^{-2} s^{-1}$). Direct capture experiments reveal a thermally activated capture cross-section; the arrhenius diagram is shown in figure 5.31:

$$\Delta E_\sigma = 49.88 \pm 0.06 meV$$

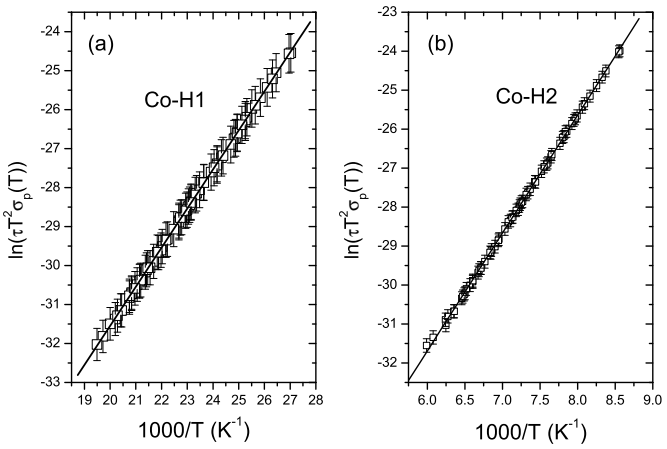

Figure 5.30: Arrhenius plot corrected for the capture cross-section for (a) the Co-H1 level and (b) the Co-H2 level.

$$\sigma_\infty = 3.7 \pm 0.4 \times 10^{-15} cm^2$$

The capture cross-section measurements are in excellent agreement with the photoconductivity measurements of Belyaev and Malogolovets [21]. They observed a thermal activation of $0.05eV$ and a capture cross-section slightly higher than 10^{-16} by extrapolation to 300K. Using our data an extrapolation to room temperature would give $5.3 \times 10^{-16} cm^2$. The entropy and enthalpy change for electron are then calculated as:

$$\Delta S = 1.98 \pm 0.12 k_B$$

$$\Delta H = 0.293 \pm 0.001 eV$$

The enthalpy change is in fair agreement with the $E_c - (0.27 \pm 0.02)eV$ observed by means of Hall-effect measurement of Tyler and Woodbury [22].
For p-type iron implanted germanium a hole trap Fe-H1 was observed where the emission could be described by the following signature ($K_T = 2.0 \times 10^9 K^{-2} s^{-1}$;$E_T = 0.345eV$). Although the capture rate was much higher comparing to the n-type samples, a capture cross-section could still be measured by means of this fitting method, using a smaller pulse height. Figure 5.32 shows

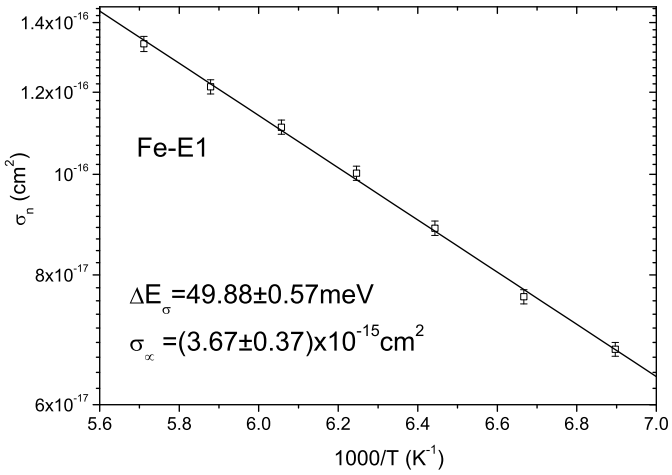

Figure 5.31: Arrhenius diagram for the capture cross-section of the Fe-E1 level.

the DLTS-signal and the corresponding fit for the measurement at $135.1K$. Within the temperature range of the emission peak no variation in capture cross-section could be observed ($T = 130 - 145K$). Correcting the signature for the average capture cross-section $\sigma_p = 2.35 \pm 0.03 \times 10^{-14}$ an entropy change for emission of:

$$\Delta S = 4.3 \pm 0.2 k_B$$

is obtained, while due to the absence of a temperature dependent capture cross-section, the enthalpy change remains equal to the activation energy of the signature, which is in very good agreement with the value value $E_v + (0.34 \pm 0.02)eV$ observed in Hall-effect measurements [22].

Chromium

For chromium an electron trap Cr-E1 is observed with a signature: ($E_T = 0.366eV; K_T = 5.2 \times 10^7 K^{-2} s^{-1}$). It may be noted that this emission energy differs seriously from the value $E_c - 0.31eV$ observed by Pearton and Tavendale for Cr-diffused n-type Ge [23]. A similar important difference indicate that a

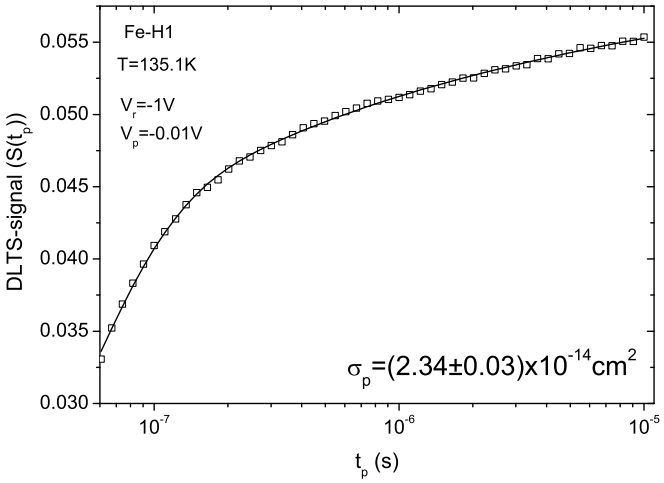

Figure 5.32: DLTS-signal as a function of filling pulse duration t_p for the Fe-H1 level.

different defect is concerned (it may be remarked that the value in [23] is close to the signature of Ni-E1, which is often encountered in metal-diffused Ge [14]). No other literature data are available on Cr related electron traps in germanium. Figure 5.33 (a) shows a $S(t_p)$ fit at 175K which reveals a capture cross-section of $\sigma_n = 5.5 \pm 10^{-19} cm^2$. The capture cross-section shows a strong temperature dependence which is shown in the diagram of figure 5.33 (b). The fitted values are:

$$\Delta E_\sigma = 55.74 \pm 0.70 meV$$

$$\sigma_\infty = (2.17 \pm 0.25) \times 10^{-17} cm^2$$

The entropy and enthalpy values obtained are:

$$\Delta S = (6.73 \pm 0.35) k_B$$

$$\Delta H = (0.311 \pm 0.004) eV$$

For p-type chromium three hole traps Cr-H1, Cr-H2 and Cr-H3 with respective E_T-values of 0.015, 0.042 and 0.088 eV could be observed [13]. The presence of a Pool-Frenkel shift [24], shows the acceptor character of the Cr-H2 and Cr-H3

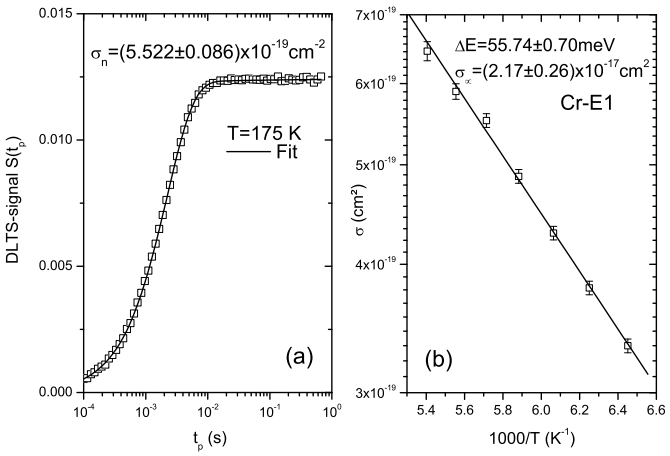

Figure 5.33: Arrhenius diagram for the capture cross-section of the Cr-E1 level.

levels. No capture experiments could be made in this case, indicating that the σ parameters are higher than $10^{-14}cm^2$. Comparison to the model of Darken [25] showed that the capture of holes by acceptor levels in germanium should be given by:

$$\sigma_p = \frac{\pi}{k^2} \tag{5.110}$$

with k the length of the wave vector describing the velocity of the carrier:

$$\frac{\hbar^2 k^2}{2m^*} = \frac{1}{2}m^* v^2 = \frac{3}{2}k_B T \tag{5.111}$$

Using equation (5.110) σ_p values in the range $10^{-13} - 10^{-12}cm^2$ are predicted.

Titanium

For Ti implanted germanium an electron trap (Ti-E1) closer to the conduction band comparing to the other metal impurities has been observed. The signature of this level corresponds to ($K_T = 3.3 \times 10^7 K^{-2}s^{-1}$, $E_T = 0.228eV$). The energy is in good agreement with the DLTS-study of Ti indifussed germanium of Pearton and Tavendale [23] who observed $E_C - 0.22eV$. Figure 5.34 (a)

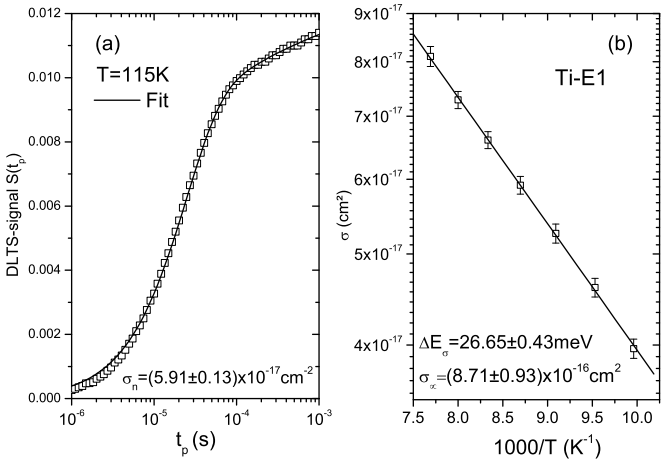

Figure 5.34: Arrhenius diagram for the capture cross-section of the Ti-E1 level.

shows the DLTS-signal as a function of filling pulse duration at 115K. The temperature dependence of the capture cross-section shown in figure 5.34 (b) could be fitted using:

$$\Delta E_\sigma = 26.65 \pm 0.44 meV$$

$$\sigma_\infty = 8.71 \pm 0.96 \times 10^{-16} cm^2$$

The corresponding correction on the signature results in the following enthalpy and entropy changes due to carrier emission:

$$\Delta S = 2.60 \pm 0.14 k_B$$

$$\Delta H = 0.201 \pm 0.001 eV$$

For the p-type Ti-implanted germanium a semi-shallow hole trap $Ti-H1$ with $E_T = 0.025eV$ has been observed. Similar as for the $Cr-H2$ and $Cr-H3$ level the acceptor property of this level was confirmed, observing the Poole-Frenkel shift. In this case too the capture rate was too fast in order to be measured.

Level	E_σ	σ_∞	ΔS	ΔH	$c_n(300K)$
	meV	cm^2	k_B	eV	cm^3s^{-1}
Ni-E1	1.3	1.9×10^{-16}	3.6	0.309	1.9×10^{-9}
Co-E1	9.8	2.3×10^{-15}	3.9	0.315	1.6×10^{-8}
Fe-E1	49.8	3.7×10^{-15}	2.0	0.293	5.3×10^{-9}
Cr-E1	55.7	2.2×10^{-17}	6.9	0.311	2.5×10^{-11}
Ti-E1	26.6	8.7×10^{-16}	2.6	0.201	3.1×10^{-9}
Hf-E1	49.9	1.5×10^{-17}	7.6	0.318	2.2×10^{-11}
Level	α	β	ΔS	ΔH	$c_p(300K)$
	cm^2K	cm^2	k_B	eV	cm^3s^{-1}
Co-H1	8.4×10^{-16}	1.9×10^{-14}	3.1	0.086	6.5×10^{-7}
Co-H2	7.4×10^{-16}	9.4×10^{-16}	1.4	0.261	4.0×10^{-8}
Fe-H1	-	2.3×10^{-14}	4.3	0.345	2.3×10^{-7}

Table 5.1: Overview of deep-level parameters obtained for transition metal impurity traps in germanium.

5.8 Influence on carrier lifetime

A summary of the deep level parameters obtained in this work is given in table 5.1. Based on these data, the effect of different metals on the minority carrier lifetime may be calculated. In the case of recombination via a deep level and in extrinsic n-type material the lifetime of the holes is given by:

$$\tau_p = \frac{1}{N_T \sigma_p v_{th}} \tag{5.112}$$

and similarly in the p-type semiconductor the lifetime of the electrons is given by

$$\tau_n = \frac{1}{N_T \sigma_n v_{th}} \tag{5.113}$$

An overview of the capture rates $c_n = \sigma_n v_{th}$ and $c_p = \sigma_p v_{th}$ calculated for the different observed levels is shown in figure 5.35. Charge states before capture are added corresponding with the assignment of Clauws et al. [13]. For simplicity the thermal velocity at room temperature is chosen $v_{th} = 10^7 cms^{-1}$.

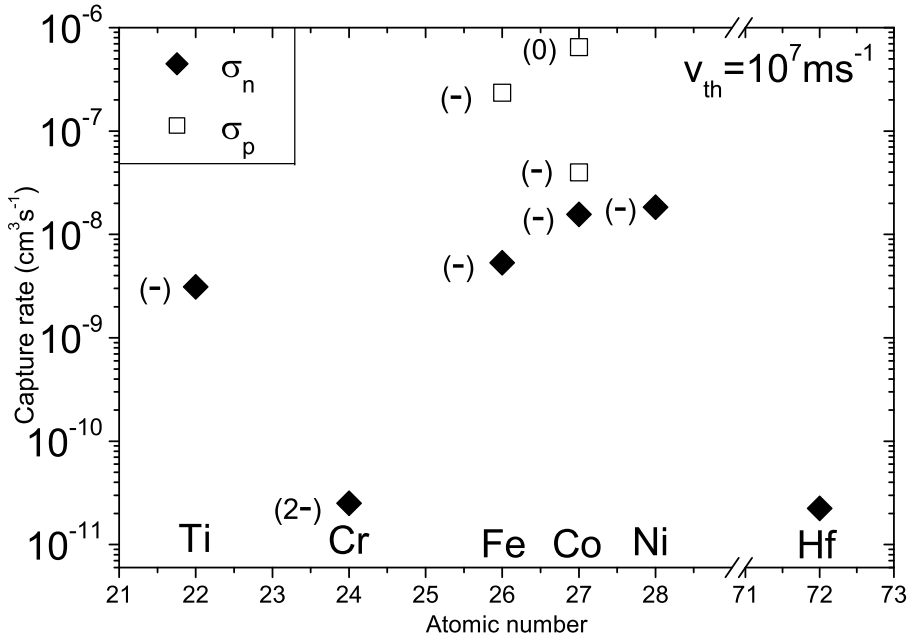

Figure 5.35: Carrier capture rate at 300K for substitutional transition metals in germanium. The charge state of defect before capture is indicared between brackets.

From these values the lifetime corresponding with a certain concentration of the impurity may be estimated. The diagram predicts that Ni and Co the most efficient life-time killers in p-type Ge while Hf and Cr are the least efficient. It may be remarked that the low capture rate for Cr corresponds with a doubly negative state, while the higher electron capture rates all correspond with a singly negative states. For Hf no charge state could be assigned. A recent review about metals in germanium is given by Claeys and Simoen [11]. The largest differences with the present data are observed for the electron capture of Co where our value is a decade higher and for Ni our value is a decade lower. However for the overall trend comparing hole and electron traps a fair correspondence is observed.

5.9 Entropy change due to electron emission

As shown in paragraph 5.2.4 direct capture experiments in combination with standard DLTS are able to determine the entropy change involved in the emission of a carrier. The entropy change ΔS for carrier emission for the different levels summarized in table 5.1. It may be noted that the entropy change involved in the electron emission of the $TM^{2-/-}$ levels is of the same order of magnitude as the values observed by Markevich et al. for donor-vacancy complexes and for the A-center (VO) (i.e. $2-4k_B$) [26]. However the Meyer-Nelder rule for the correspondence between K_T and E_T observed by Markevich et al. is not followed.

This entropy change can be divided in a configurational ΔS_{conf} and a vibrational part ΔS_{vibr} involved in the reaction. The Boltzmann formula to calculate the configurational entropy is:

$$S_{conf} = k_B \ln(\Omega) \tag{5.114}$$

where Ω is the total electronic degeneracy of the defect. The configurational entropy change in the transition would then be:

$$\Delta S_{\text{conf}} = k_B \ln\left(\frac{\Omega_{final}}{\Omega_{initial}}\right) \tag{5.115}$$

Experimental values larger than the configurational entropy may be ascribed to the lattice entropy change due to the generation of a carrier in the bands. Following Brotherton and Lowther [27], the change in lattice entropy depends on the final and initial phonon density ν_{final} and $\nu_{initial}$ and can be written as:

$$\Delta S_{vibr} = \sum_i k_B \ln\left(\frac{\nu_{final}}{\nu_{initial}}\right) \tag{5.116}$$

From simple theoretical considerations Van Vechten and Thurmond [28] have related lattice entropy change to that occuring when a free carrier is produced by band-gap excitation ΔS_{C-V}. To estimate the lattice entropy change of germanium change we use the temperature dependence of the band-gap:

$$E_G(T) = 0.742 - \frac{T[K]^2}{(T[K] + 235)\,2833}[eV] \tag{5.117}$$

which can in the temperature range concerned be approximated as $\Delta G_{C-V} = \Delta H_{C-V} - T\Delta S_{C-V}$. It follows that the lattice entropy can be approximated as $\Delta S_{vibr} \approx 2.5 k_B$ within the range between $100K - 180K$.

To calculate the configurational entropy change requires some detailed insight into the microscopic structure of the defect. The only substitutional transition metal studied, for which literature data on the microscopic structure are available, is Ni. From ESR (Electron Spin Resonance) measurements Woodbury and Ludwig observed a similar spectrum for Pd^- and Pt^- in Si [29] as for the 3d analogon Ni^- in Ge [30]. Essentially the same model has been proposed for the three centers. Figure 5.36 shows the binding configuration according to this model for the charge state Ni^0. The model bears many resemblances with the well-known model of the A-center in Si and Ge. The transition metal or the oxygen atom is displaced from the substitutional lattice position, making

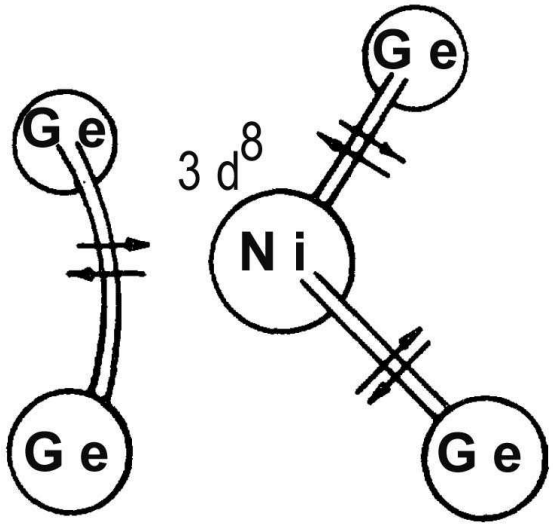

Figure 5.36: Schematic model of the microscopic structure of Ni^0 in Ge.

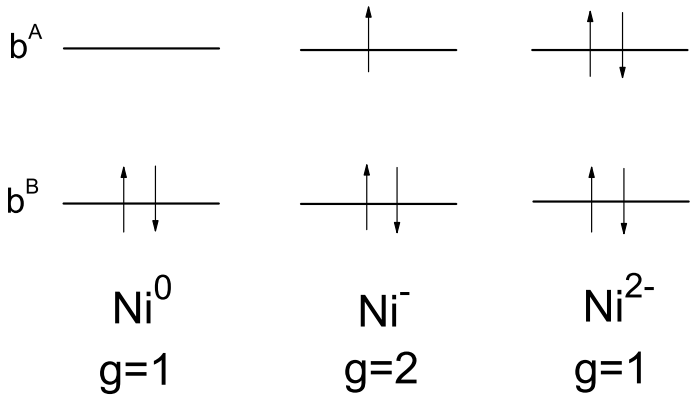

Figure 5.37: Occupation of the bonding (b^B) and antibonding (d^A) states of the reconstructed Ge atoms.

bonds with two Ge-neighbours, while the two other neighbours form a reconstructed bond. The transitions observed in DLTS of the Ni-E1 level are then due to electrons in the anti-bonding orbital of the reconstructed bond, similar as for the A-centre and the model for Pt^- in Si of Brotherton and Lowther [27].

Figure 5.37 shows the occupation of the levels for the neutral, singly negative and doubly negative charge state of Ni. The levels b^B and b^A refer to bonding and antibonding states respectively of the lattice reconstruction. The configurational entropy change for electron emission $Ni^{2-} \rightarrow Ni^- + e^-$ can be calculated from this model:

$$\Delta S_{conf} = k_B \ln(2) = 0.7 k_B$$

Concerning the vibrational entropy change ΔS_{vibr}, Brotherton and Lowther [27] assumed no vibrational entropy change for Pt^- in Si because the change in electron occupation occurs in the anti-binding orbital. However for the A-center Vanmeerbeek found using vibrational mode spectroscopy that the position of the oxygen atom changes depending on the total charge state of the center [31], and thus a vibrational contribution may be expected. If we include a vibrational entropy as described above $\Delta S = 2.5 k_B$ one may expect a total entropy change for the emission of an electron from the Ni-E1 level: $\Delta S_{tot} = 3.2 k_B$, which is in fair agreement with the experimental value $\Delta S_{tot} = 3.6 \pm 0.4 k_B$.

A similar procedure would perhaps also be possible to explain the observed entropy values of the other metals studied, however one should be careful about the conclusions in the absence of a valid binding model, following from ESR measurements for example.

5.10 Conclusions

In this chapter an accurate analytic approximation to the DLTS-amplitude as a function of filling pulse was derived. The function was implemented as a user

friendly fitting tool with a Levenberg-Marquardt fitting method, including the Hessian matrix. A study of the properties of this approximation showed that it is valid independent of the filling pulse duration and is still an accurate approximation for small pulse heights.

This model was applied on transition metals in germanium. This made it possible to obtain thermodynamical properties, like entropy and enthalpy change for emission.

Thanks to this novel method the reliability of the deep level parameters of transition metal impurities in germanium could be seriously improved. The data may be considered as a solid basis for comparison with literature data and with future theoretical calculations and for predicting effects of transition metals on devices.

Bibliography

[1] S.M. Sze. *The physics of semiconductor devices.* John Wiley and Sons, 1969.

[2] P. Blood and J.W. Orton. *The Electrical Characterization of Semiconductors: Majority Carriers and Electron States.* Academic Press, London, 1992.

[3] S. Weiss and R. Kassing. Deep level transient fourier spectroscopy (DLTFS) - A technique for the analysis of deep level impurities. *Solid state electronics*, 31(12):1733, 1988.

[4] J. Van Gheluwe. *Karakterisering van CdTe/CdS en CuInS2-op-Cu-tape dunnefilmzonnecelllen met behulp van fotoluminescentiespectroscopie en 'deep level transient spectroscopy'.* PhD thesis, Universiteit Gent, 2007.

[5] C.H. Henry and D.V. Lang. Nonradiative capture and recombination by multiphonon emission in gaas and gap. *Physical review B*, 15:989, 1977.

[6] D. Pons. Accurate determination of the free carrier capture kinetics of deep traps by space-charge methods. *Journal of applied physics*, 55(10):3644, 1984.

[7] O. Madelung, U. Rössler, and M. Schulz. *Landolt and Bornstein Semiconductors.* Springer-Verlag, 1998.

[8] D. Stievenard, J.C. Bourgoin, and M. Lannoo. An easy method to de-

termine carrier-capture cross sections: application to GaAs. *Journal of applied physics*, 55(6):1477, 1984.

[9] W.W. Tyler. Deep level impurities in germanium. *Journal of physical chemistry of solids*, 8:59, 1959.

[10] A.G. Milnes. *Deep impurities in semiconductors*. J. Wiley and Sons, 1973.

[11] E. Simoen and C. Claeys. *Germanium based technologies, from materials to devices*. Elsevier, 2007.

[12] P. Clauws and E. Simoen. Metals in germanium. *Materials science in semiconductor processing*, 9:546, 2006.

[13] P. Clauws, J. Van Gheluwe, J. Lauwaert, E. Simoen, J. Vanhellemont, M. Meuris, and A. Theuwis. Deep level transient spectroscopy of transition metal impurities in germanium. *Physica B-Condensed matter*, 401:188, 2007.

[14] S. Forment, J. Vanhellemont, P. Clauws, J. Van Steenbergen, S. Sioncke, M. Meuris, E. Simoen, and A. Theuwis. A deep-level transient spectroscopy study of transition metals in n-type germanium. *Materials science in semiconductor processing*, 9:559, 2006.

[15] I.M. Kotina, V.V. Kuryatkov, S.R. Novikov, and T.I. Pirozhkova. Capacitance spectroscopy of deep Cu, Au, Ag, and Ni centers in germanium. *Soviet physics semiconductors*, 21(6):635, 1987.

[16] G. Huylebroeck, P. Clauws, E. Simoen, and J. Vennik. DLTS of nickel impurities in germanium. *Solid state communications*, 82(5):367, 1992.

[17] S.J. Pearton. Deep metal-related centres in germanium. *Solid-state electronics*, 25(4):305, 1982.

[18] G.K. Wertheim. Recombination properties of nickel in germanium. *Physical review*, 115(1):37, 1959.

[19] A.D. Belyaev and E.G. Miselyuk. Electron recombination at negative ions of nickel in germanium. *Soviet physics-solid state*, 6(9):2101, 1964.

[20] W.W. Tyler, R. Newman, and H.H. Woodbury. Properties of germanium doped with cobalt. *Physical review*, 97(3):669, 1955.

[21] A.D. Belyaev and V.G. Malogolovets. Effective cross section for electron capture by negative iron ions in germanium. *Soviet phyiscs solid state*, 5(10):2229, 1964.

[22] W.W. Tyler and H.H. Woodbury. Properties of germanium doped with iron: I. Electrical conductivity. *Physical review*, 96(4):874, 1954.

[23] S.J. Pearton and A.J. Tavendale. Hydrogen passivation of deep metal-related donor centers in germanium. *Journal of applied physics*, 54(2):820, 1983.

[24] Frenkel. On pre-breakdown phenomena in insulators and electronic semiconductors. *Physical review*, 54:647, 1938.

[25] L.S. Darken. Theoretical model for hole capture at acceptors in germanium. *Physical review letters*, 69(19):2839, 1992.

[26] V.P. Markevich, I.D. Hawkins, A.R. Peaker, K.V. Emtsev, V.V. Emtsev, V.V. Litvinov, L.I. Murin, and L. Dobaczewski. Vacancy-group-V-impurity atom pairs in ge crystals doped with p, as,sb and bi. *Physical review B*, 70:235213, 2004.

[27] S.D. Brotherton and J.E. Lowther. Electron and hole capture at Au and Pt centres in silicon. *Physical review letters*, 44(9):606, 1980.

[28] J.A. Van Vechten and C.D. Thurmond. Entropy of ionization and temperature variation of ionization levels of defects in semiconductors. *Physical review B*, 14(8):3539, 1976.

[29] H.H. Woodbury and G.W. Ludwig. Spin resonance of Pd and Pt in silicon. *Physical review*, 126(2):466, 1962.

[30] G.W. Ludwig and H.H. Woodbury. Electron spin resonance of nickel-doped germanium. *Physical review*, 113(4):1014, 1959.

[31] P. Vanmeerbeek. *Locale vibrationele-mode infraroodspectroscopie van zuurstof gerelateerde defecten in germanium.* PhD thesis, Universiteit Gent, 2004.

Chapter 6

Passivation of transition metal impurities in germanium by means of hydrogenation

6.1 Introduction

Due to its high reactivity hydrogen interacts with a variety of defects in a semiconductor, including shallow and deep level impurities, point defects, extended defects with dangling bonds etc ... One interesting effect with respect to applications is the possibility to passivate electrically active defects trough binding with a hydrogen atom. In silicon passivation of shallow dopants and of transition metal impurities by complex formation with hydrogen has been well established; a recent summary may be found in Ref. [1].

The occurrence of defect complexes with hydrogen in germanium is known since the development of high purity germanium for radiation detector applications in the 1970's. This material is grown in a hydrogen containing atmosphere in order to suppress trapping, suggesting that deep traps become passivated by the hydrogen. On the other hand the neutral impurities Si, C and O become 'activated' and form shallow complexes such as (Si,H) and (C,H) acceptors and (O,H) donors, which may be observed with PTIS. Also a deep level inducing

severe trapping is formed by the V_2H complex. A review of these observations is given in Ref. [2]. Partially passivated multivalent acceptors in germanium are very interesting since they remain experimentally accessible trough their electronic level spectrum. The double acceptors Be and Zn become single acceptors (Be,H) and (Zn,H) with trigonal symmetry, trough binding with a hydrogen atom [3, 4]. Probably the most interesting case in the present context is passivation of the triple acceptor copper, which is presented in the next section. A simple model to explain passivation of multiple acceptors is that hydrogen is a single donor which is attracted by the negatively charged acceptor, forming a donor-acceptor pair. The acceptor multiplicity is then reduced with one unit for every hydrogen added.

The possibility to passivate transition metal impurities is obviously a topic of practical importance to advanced germanium material. As discussed in the previous chapter, transition metal impurities in general form double or triple acceptors in germanium and so are possible candidates for studying partial or complete passivation. In this chapter we summarize the DLTS results obtained with hydrogen-plasma treatment of the transition metal-implanted germanium available in our research group. It may be mentioned that in the past a few papers have already been published concerning hydrogen passivation of transition metals in germanium [5, 6]. The significance of the latter results may however be considered as rather doubtful. Indeed the DLTS spectra of the transition metals published by the authors have in most cases not been confirmed by later studies and so it is unclear what defects (contaminants ?) are concerned.

Concerning transition metal impurities in germanium, convincing evidence of passivation has only been presented for Cu, a triple acceptor that may be passivated partially or completely by formation of $Cu - H_n$ complexes discussed in the following paragraph.

Afterwards a study of hydrogenated transition metal implanted germanium by means of DLTS will be presented, which has resulted in the formation of metal dependent levels. Those could thus be tentatively assigned to transition metal

hydrogen complexes.

6.2 Copper-hydrogen complexes

Substitutional copper is in germanium a triple acceptor with an overcharged donor level close to the valence band. The three acceptor levels as measured by means of Hall-effect are: $E_v + 44meV$, $E_v + 330meV$ and $E_c - 260meV$ [7]. Those levels have also been observed by means of DLTS, the hole traps by Simoen et al. [8] and the electron trap by Clauws et al. [9]. The copper atom forms several complexes with hydrogen. The acceptor complexes $Cu-H$ (double acceptor) and $Cu-H_2$ (single acceptor) were first observed by Haller et al. [10]. Using PTIS and Hall-effect measurements the following energy levels were assigned: $Cu-H$: $E_v+17.5meV$ and $E_v+(170\pm20)meV$, $Cu-H_2$: $E_v + 17meV$. The levels are shown in the diagram in figure 6.1. From this trend Haller et al. [10] came to the following model. The triple acceptor Cu can accept either free electrons or electrons from hydrogen atoms to complete its strongly deficient site. In case of the acceptance of a free electron, further electrons have to be accepted against the Coulomb repulsion. A totally different situation occurs if a hydrogen atom is forming a complex with copper. No Coulomb barrier is created against further addition of electrons. This makes the energy levels of the complex move closer to the valence band edge. Thus it is believed that the $Cu-H_3$ complex is always neutral. Similar observations were made due to the binding with lithium but passivation by lithium atoms is beyond the scope of this work. Later new PTIS measurements were reported by Kahn et al. [11] which proved that the reported level $E_v+ \sim 17meV$ was indeed due to the copper-dihydrogen complex. For this purpose high-purity germanium crystals were grown in a H_2, D_2 or 1:1 H_2-D_2 mixture. Also hydrogen free crystals were exposed to plasmas of H_2-T_2 mixtures. PTIS revealed different effective mass like series, which could be explained by the substitutional copper complex passivated by two hydrogen nuclei X and Y shown in figure 6.2.

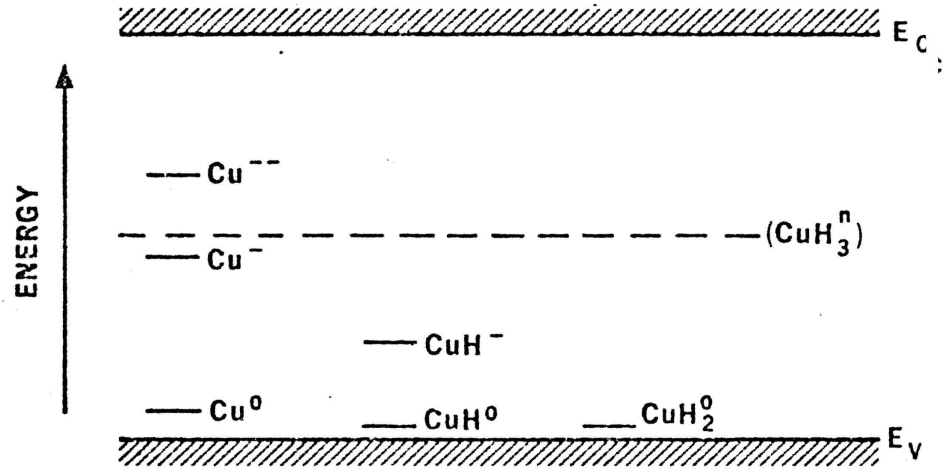

Figure 6.1: Position of the acceptor levels of copper and its complexes with hydrogen (figure taken from Haller et al. [10])

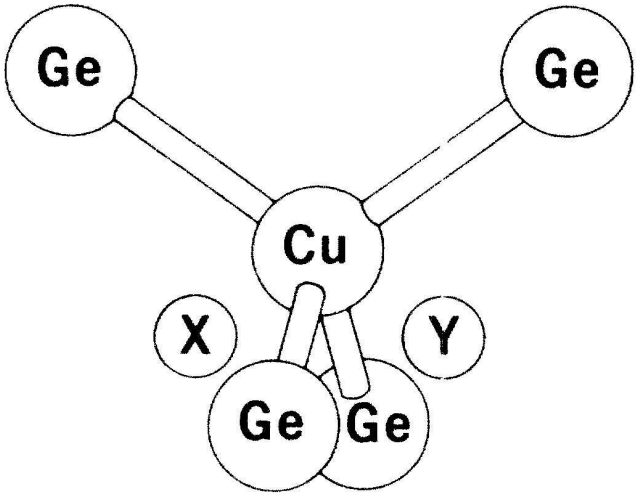

Figure 6.2: Schematic structure of the copper-dihydrogen complex with the two hydrogen nuclei X and Y, viewed slightly of a <110> direction (figure taken from Kahn et al. [11])

6.3 Experimental

To study the passivation effect of plasma hydrogenation on substitutional metal impurities, transition metal implanted germanium samples have been hydrogenated for 4h at 200℃. The original n-type and p-type material had a shallow dopant concentration of $5 \times 10^{13} cm^{-3}$ and $1 \times 10^{14} cm^{-3}$ respectively. A 5 min post-implantation thermal anneal at 500℃ was applied to restore the implantation damage and to diffuse the metal impurities deeper into the bulk of the wafer. Schottky diodes for DLTS were prepared by evaporation of a Au barrier (on n-type) or In barrier (on p-type). The evaporation was preceded by a short etch in a $HNO_3 : HF$ $(3:1)$ solution, a procedure which was already applied for the metal implanted samples studied in Chapter 5 and which seriously improves the quality of the diodes for DLTS. Comparing to chapter 4 where no etching step was made after the plasma treatment, the defects created deeper in the bulk were studied and the extended-defect rich region was removed. Possibly not only the etching but also the higher hydrogenation temperature makes that the E1 and H1 levels described in section 4.6 (see figure 4.16) are absent. Only in some p-type samples a small H1 band could still be observed.

6.4 Passivation of Cobalt

In figure 6.3 the DLTS spectrum of Co-implanted n- and p-type germanium is shown before and after a plasma hydrogenation treatment. The Co-H1, Co-H2 and Co-E1 levels are assigned by Clauws et al. [12] to the $Co^{+/0}$ donor and $Co^{0/-}$, $Co^{-/2-}$ double acceptor levels of Co-impurities respectively. This assignment was made based on the similarity with the levels observed by Tyler using Hall-effect [13]. After the hydrogenation all the substitutional cobalt levels within the measured region of 5μm are completely absent. Only a semi shallow level (E028) has formed within this spatial region approximately 28meV below the conduction band. The defect levels generated deeper into the bulk are discussed below.

Table 6.1: Overview of signatures (E_T, K_T) of defects observed in DLTS of Co-implanted and hydrogenated n-type and p-type germanium.

Level	Carrier	$E_T(eV)$	$K_T(K^{-2}s^{-1})$	Sample treatment
H126	h	0.126	7.4×10^7	H and Air plasma
H286	h	0.286	2.4×10^8	H and Air plasma
H347	h	0.347	6.8×10^7	H and Air plasma
E028	e	0.028	3×10^8	H and Air Plasma
E300	e	0.307	2.8×10^7	H and Air plasma
E230	e	0.23	4×10^6	Co-impl. + H plasma
E270	e	0.27	1.9×10^7	Co-impl. + H plasma

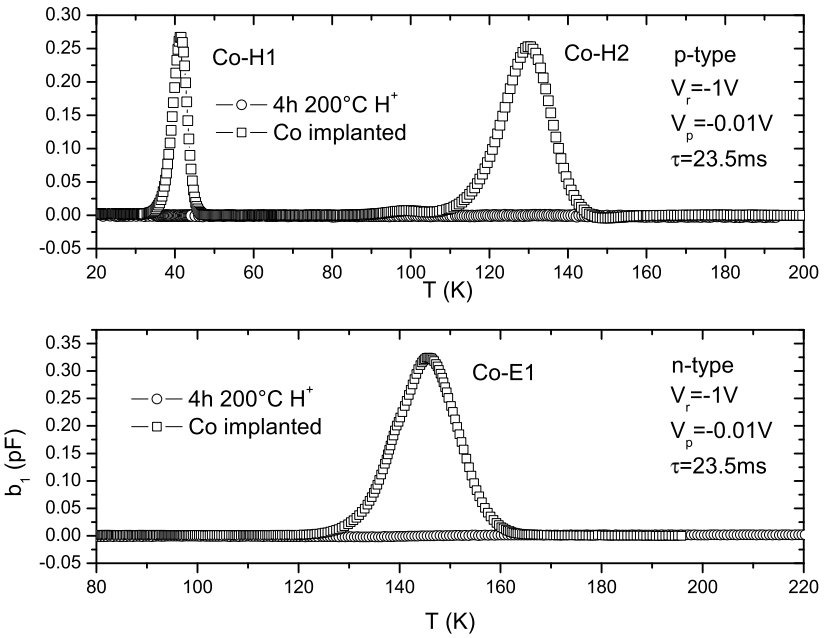

Figure 6.3: DLTS-spectra of n- and p-type Co-implanted germanium before and after 4h 200℃ hydrogen plasma treatment.

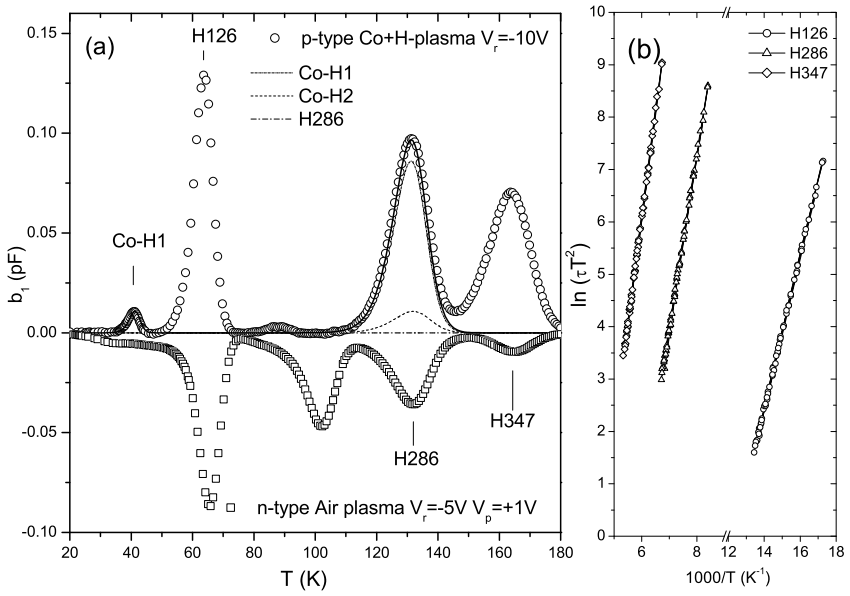

Figure 6.4: (a) DLTS-spectra of p-type cobalt implanted germanium after 4h 200℃ hydrogen plasma treatment using $V_r = -10V$, which shows that Co-H1 and Co-H2 are still present deeper into the bulk. The spectrum of n-type after 4h 200℃ residual air plasma treatment shows the H126, H286 and H347 levels as minority carrier traps. (b) Arrhenius diagram for the H126, H286 and H347 levels.

6.4.1 P-type

Beyond 5μm from the treated surface different hole traps are observed after the hydrogenation. In figure 6.4 the DLTS-spectrum shows three levels different from the original substitutional cobalt defect shown in figure 6.3. A small signal corresponding to the Co-H1 level is also detected. Due to the strong contribution of the H286 level at 130K, a probable contribution of the Co-H2 level is difficult to distinguish. Nevertheless it was possible to fit the DLTS-signal as a sum of two components. The Arrhenius diagram of the carrier emission of the H126, H286 and H347 levels is shown in figure 6.4 (b). To

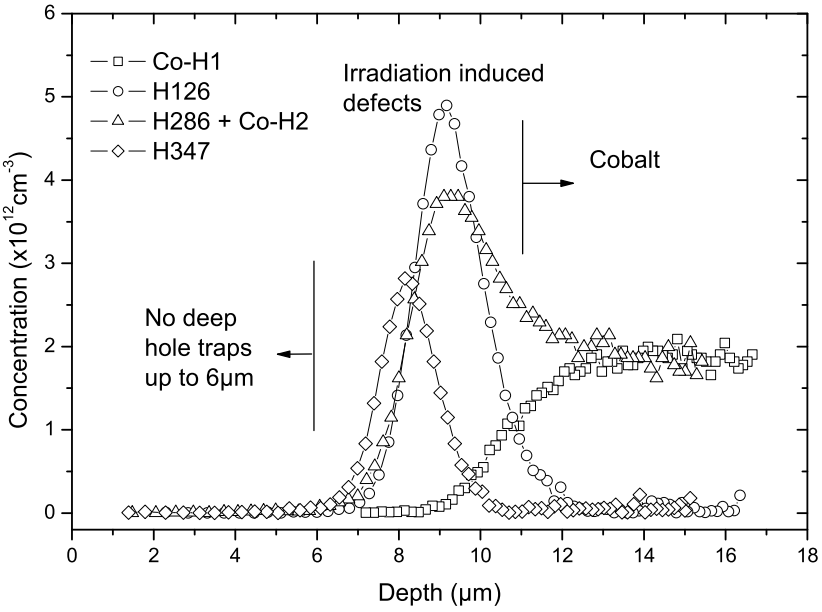

Figure 6.5: Depth profile measured using a constant pulse height ($V_p - V_r = 0.5V$) for different reverse biases. The emission transient originating from the hole trap was measured at the corresponding peak temperature.

evaluate the impact of the plasma irradiation as such, an originally non-cobalt implanted n-type Sb-doped sample has been treated in a residual air plasma for comparison. The presence of the H126, H286 and H347 hole traps in this sample (figure 6.4 b, lower spectrum) indicates that the traps are not hydrogen or cobalt related. This observation makes it plausible to assign the three levels to irradiation damage generated by the plasma treatment. It may be noted that in the reference sample an additional band is present at 100K, which is less relevant in the context of this chapter.

The depth profile of the Co implanted hydrogenated sample obtained, using an isothermal constant pulse height measurements at the different peak temperatures, is given in figure 6.5. The concentration of defects was calculated

directly from the amplitude of the emission transient including a pulse correction factor. Because no entropy or enthalpy correction was included in the calculation of the position where the Fermi level crosses the trap level, it might be possible that small errors in the estimated profiles have been introduced. It could be clearly observed that the thus obtained profile measured at 134.1K includes a contribution of the Co-H2 emission with the same profile as the Co-H1 level, which confirms the presence of the original cobalt defect beyond 9μm from the surface (figure 6.5). From the absence of traps up to 6μm depth, one can conclude that close to the surface no defects with electronic states within the band gap have been formed. One possibility may be the formation of irradiation damage clusters close to the surface, which getter the Co. The absence of a significant change in the free carrier profile would in this case suggest that all the Ga acceptors have stayed electrically active. The higher diffusion coefficient of Co comparing with Ga would make the gettering of Co more probable. Another possible explanation is that the hydrogen passivates not only the dangling bonds of the cobalt defects, but also the irradiation defects.

Different Rapid Thermal Anneal (RTA) steps were performed on these samples. Figure 6.6 shows the DLTS-spectra after RTA 320℃, 400 ℃ and 500℃ for 1 minute. While 320℃ and 400℃ result in a reduction of the irradiation induced defects, no restoration of the cobalt impurity can be observed. After the RTA step at 500℃ different new hole traps could be observed. The H027 and H304 levels can most probably be identified with so-called quenching defects in germanium (see e.g. Pearton et al. [14]), also because the levels are observed with a higher concentration using a 600℃ or 700℃ RTA step. Also the presence of the two peaks in a 750℃ RTA quench of an as-grown sample[1] confirms the assignment to thermally induced defects. It should be noted that the irradiation damage due to hydrogenation significantly enhances the formation of thermal defects, because after a single RTA step at 500℃ of a non-hydrogenated Co-implanted sample none of these levels could be observed.

[1]Internship report Agnieska Witecka and Marta Szankowska, Ugent september 2007

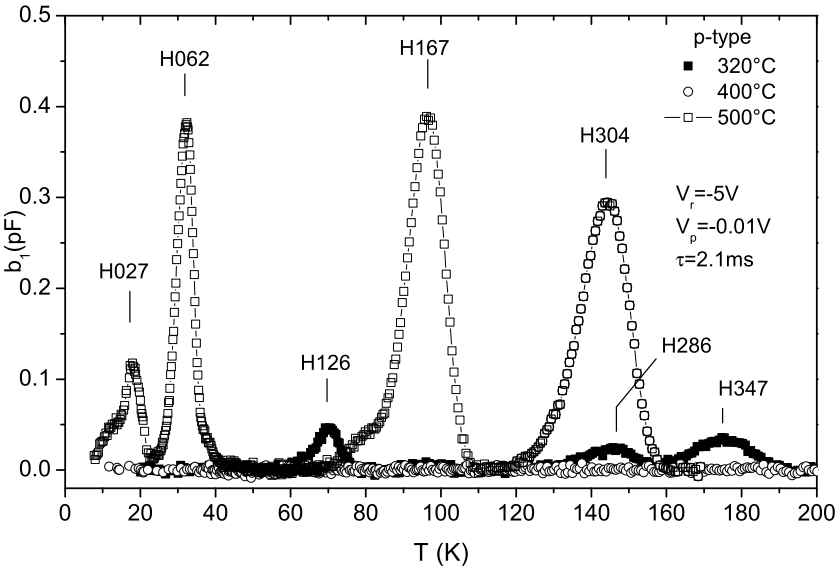

Figure 6.6: DLTS of p-Ge:Co hydrogenated 4h 200℃ plus an additional RTA step.

The H062 and H167 hole traps show a similar concentration profile suggesting that they belong to the same defect, most probably the Cu-H defect. Comparing to the measurement shown in figure 6.6 the position of the emission peaks corresponding with the Arrhenius of $Cu-H$ [15] should be at 101K and 36K, which is higher than the peak maxima observed in our sample. This shift may be explained by the Poole-Frenkel effect for attractive centers. The assignment to Cu-H would mean that due to one of the process steps the sample has been contaminated with copper. Due to the absence of the traps at higher RTA temperatures and after a 15 minutes 500°C oven anneal and the absence of other fast diffusing contaminants like Ni, the reason for the occurrence of the Cu-H bands is unclear.

6.4.2 N-type

The DLTS-spectrum of the n-type Co-implanted sample after plasma hydrogenation contains five different electron traps, which are listed in table 6.1. Figure 6.7 shows the DLTS-spectrum after an RTA treatment for 1min at 400°C. Directly after the plasma treatment the DLTS-spectrum is strongly dominated by the E300 level, which has a similar depth profile as the irradiation related levels (H126, H286 and H347) in p-type material. It may be noted that also a semi shallow level E028 may be observed. The strong reduction of the concentration of the E300 level after a thermal treatment (i.e. a 30min 200°C oven anneal results in a complete disappearance of this level) and the signature that has a good correspondence with a level reported by Fage-Pedersen et al. [17] suggest the assignment of this defect to the di-vacancy. The signature of the E300 level in Table 6.1 level has been measured using the Constant Capacitance DLTS-technique (CC) on an as-plasma treated sample. Figure 6.8 shows the Arrhenius diagrams of the four emission constants which have been deduced from the fits to the DLTS-spectra of the Co-implanted samples. The symbols correspond with the emission constant derived from the isothermal DLTS measurements of the RTA-treated sample at 400°C. The electron capture cross-section of the band Co-E1, determined from isothermal measurements as

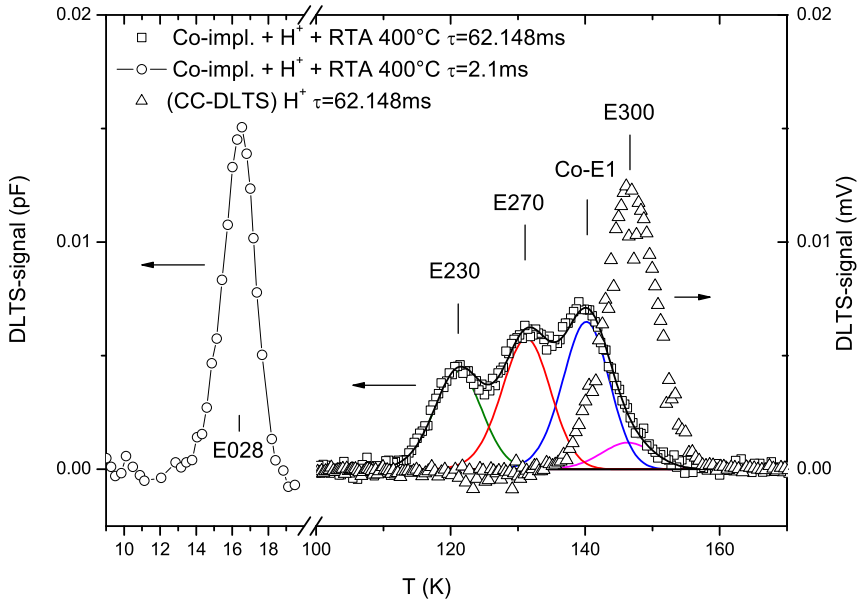

Figure 6.7: DLTS-spectrum of Cobalt implanted plasma hydrogenated sample after an RTA treatment of 1 minute at 400°C. The constant-capacitance spectrum of a n-type hydrogen plasma sample was added to show the presence of the E300 level in a non-cobalt implanted sample. The peaks have been resolved using a Double Sqr [16] filter function.

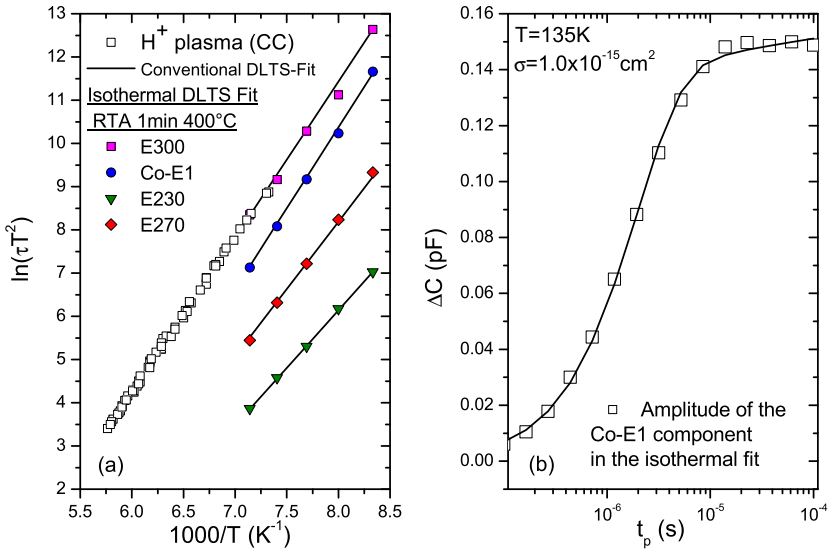

Figure 6.8: (a) Arrhenius diagrams of the four components in the spectrum of the hydrogenated cobalt implanted sample. (b) Amplitude of the Co-E1 component in function of the filling pulse duration.

a function of pulse duration corresponds with the value obtained for substitutional Co, substantiating its assignment to the $Co^{-/2-}$ level (Chapter 5 and [12]). The E230 and E270 levels which are observed after the hydrogenation are still present after a 1min 400°C RTA step, while the E300 level has reduced significantly. This suggests that the E230 and E270 levels may be tentatively assigned to a cobalt related center. After a 1 min RTA at 500°C only one DLTS peak is observed, as shown in figure 6.9 (a). The signature obtained at $V_r = -5V$ is ($K_T = 2.4 \times 10^8 K^{-2} s^{-1}; \Delta E_T = 188meV$). The strong freeze-out of the quiescent capacitance and the peak shift to larger rate windows for increasing reverse bias [18], demonstrates that the high trap concentration has an influence on the free carrier concentration. It may be noted that similar isothermal measurements in constant capacitance mode show no peak shift, which

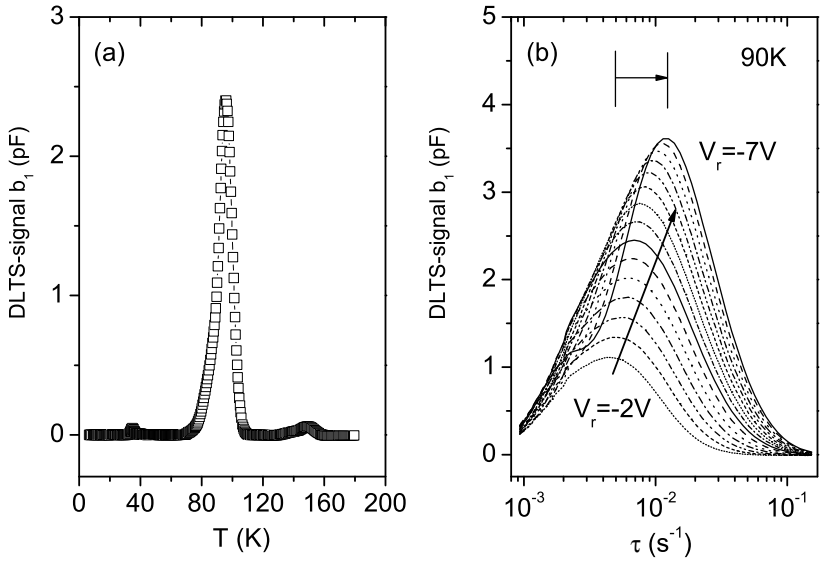

Figure 6.9: Electron trap E187 observed in n-Ge:Co hydrogenated and RTA annealed at 500°C. (a) Conventional DLTS-spectrum (b) Isothermal DLTS at 90K

confirms that the shift in standard DLTS is due to the high concentration. CC-DLTS reveals a signature of ($K_T = 8.5 \times 10^7 K^{-2} s^{-1}; \Delta E_T = 189meV$).

6.5 Hydrogenation of iron, chromium and titanium implanted samples

6.5.1 Iron

The DLTS-spectrum of n-Ge:Fe hydrogenated at 200°C for 4 hours is shown in figure 6.10 (a). Close to the surface no electron traps could be observed, demonstrating the passivation by means of hydrogenation. Further beyond the surface (i.e. $V_r = -5V$) a large emission peak at 150K was observed which can be fitted using both the E300 and the Fe-E1 signature characteristics

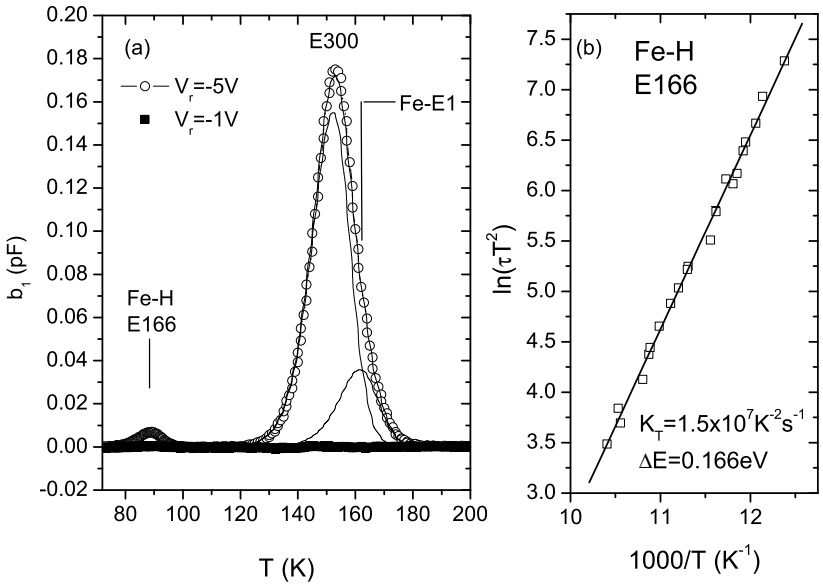

Figure 6.10: (a) DLTS spectrum of the n-Ge:Fe hydrogenated at 200℃for 4 houres (b) Arrhenius diagram for the Fe-H E166 level.

as shown in figure 6.10 (a). For lower temperatures only a small emission peak labeled Fe-H E166 is observed, which has only been observed in Fe-doped material and therefore is tentatively assigned to a Fe related level. The Arrhenius diagram is shown in figure 6.10 (b). Figure 6.11 (a) shows the DLTS spectrum of an hydrogenated p-Ge:Fe sample. Similar irradiation induced hole traps are observed as in the Co-implanted samples. The small feature at 90K corresponds with the H170 level observed in as-plasma treated material at 150℃(i.e. the H1-level discussed in section 4.6). A small emission peak at 42K labeled Fe-H H076 is transition metal dependent and thus can be assigned to an Fe related complex. From the depth profile shown in figure 6.11 (b) one can conclude that up to 5 μm beyond the surface all levels are passivated, while from 12μm on Fe can be observed. Not only the relation to Fe but also the profile close to the surface confirms the assignment of H076 to an iron-hydrogen

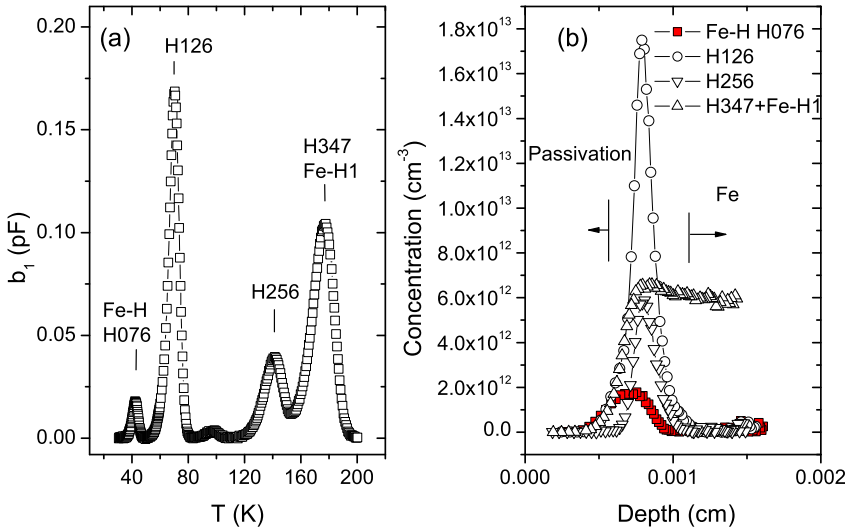

Figure 6.11: (a) DLTS spectrum of p-Ge:Fe hydrogenated at 200°C for 4 hours (b) Depth profile measured using a $\Delta V = 0.5V$ constant pulse height method for the different hole traps.

related complex.

6.5.2 Chromium

Although for n-Ge:Cr no real passivation has been observed (i.e. the Cr-E1 level is still present after hydrogenation), a new metal related electron trap E098 could be detected. Figure 6.12 (a) shows the DLTS spectrum for $V_r = -0.5V$ and $V_r = -1V$. The Arrhenius diagram of the Cr-H E098 level is shown in figure 6.12 (b). Figure 6.13 shows the DLTS-spectra for p-Ge:Cr after the plasma hydrogenation. Close to the treated surface no hole traps could be observed, while further from the surface different hole traps were detected. Apart from the irradiation damage and substitutional chromium levels, two metal dependent levels were discovered (marked with an arrow). In figure 6.13 (a) using the shortest rate window the Cr-H H030 level is visible

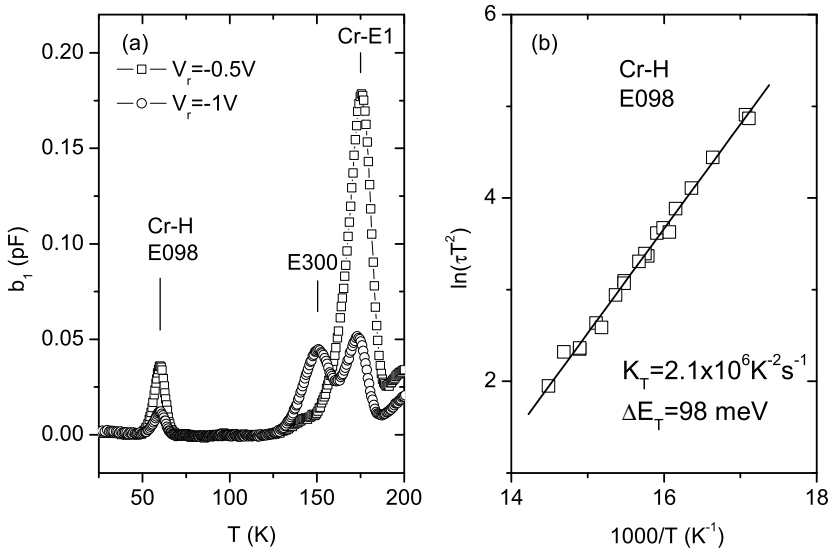

Figure 6.12: (a) DLTS spectrum of n-Ge:Cr hydrogenated at 200°C for 4 hours (b) Arrhenius diagram for the Cr-H E098 level.

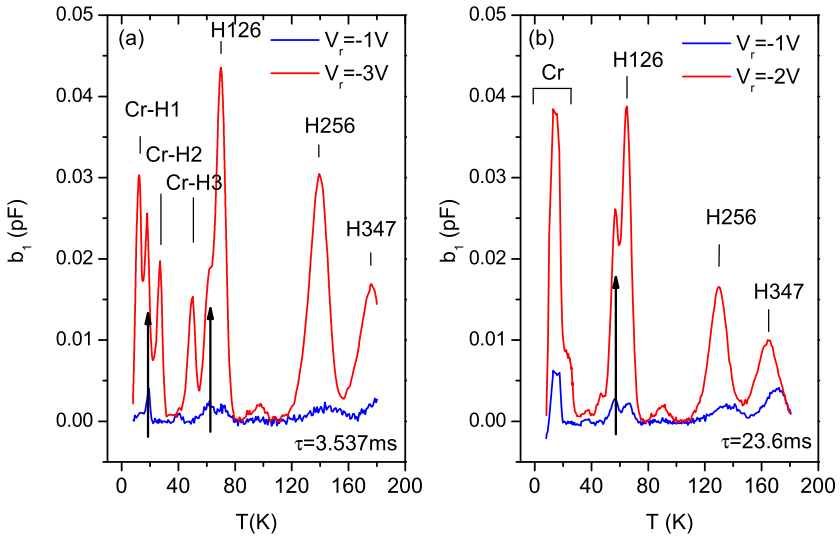

Figure 6.13: DLTS spectrum for p-Ge:Cr hydrogenated samples for two different rate windows (a) 3.5ms and (b) 23.6ms

with a signature ($K_T = 4.5 \times 10^7 K^{-2} s^{-1}$, $\Delta E = 0.030eV$), while the Cr-H H100 level is only visible as a shoulder in the H126 peak. For longer rate windows shown in figure 6.13 (b) the peak can be resolved and the signature could be determined as ($K_T = 2.2 \times 10^7 K^{-2} s^{-1}$, $\Delta E = 0.100eV$). Due to the observed Poole-Frenkel effect of the Cr-H2 and Cr-H3 levels we could show that chromium acts as a triple acceptor in germanium, which is a similar situation as for copper. This similarity would suggest a Cr-H center which acts as a double acceptor with two hole traps. The presence of Cr-H H100 and Cr-H H030 level in the p-type hydrogenated sample may therefore be tentatively assigned to the Cr-H center. Further experiments are needed to support this assignment.

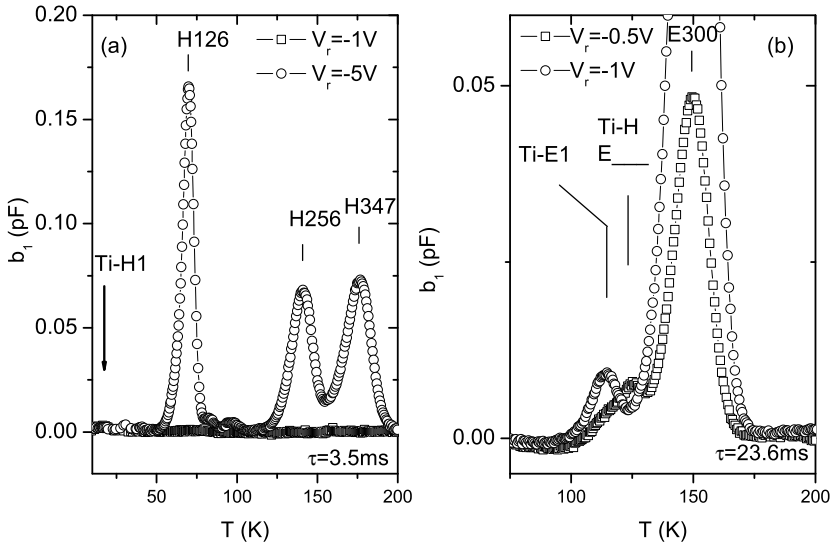

Figure 6.14: DLTS spectrum of hydrogenated titanium implanted samples (a) p-type (b) n-type

6.5.3 Titanium

Titanium has been completely passivated in p-type germanium and no Ti related trap could be observed after the hydrogenation. DLTS-spectra for p-Ge:Ti after hydrogenation show that deeper into the bulk only the irradiation related levels are present (see figure 6.14). For n-type material the Ti-impurities are passivated close to the surface, while a metal dependent peak could be observed as a shoulder to the E300 peak on the lower temperature side. Deeper into the bulk the Ti-E1 level was observed. It should be noted that the passivation of Ti corresponds well with the observation of Pearton et al. [5].

6.6 Conclusions and outlook

Before the hydrogenation the Co, Fe, Cr and Ti implanted germanium samples show both for n-type and p-type a decreasing trap level profile from the surface (see chapter 5 and reference [12]). After a direct plasma hydrogenation at 200°C for 4 hours three not strictly separated spatial regions, with different trap levels could be observed by means of isothermal DLTS profiling techniques.

A first region is approximatelly 5 μm thick. Within this region all electron and hole traps are completely absent. It may be noted that this is not the case for n-type Cr-implanted germanium. The hydrogenation results in the passivation of only the deep traps, because no obvious changes in the shallow background doping was measured by means of capacitance voltage profiling. This observation is in agreement with the well-known fact that high-purity germanium with a sufficiently low trap concentration can only be obtained by growing in an hydrogen ambient [19].

In the second region which lies approximately between 5 and 12 μm, radiation induced electron traps could be observed, one of which could be assigned to the di-vacancy [17]. Also different hole traps could also be detected with a similar concentration profile. The H126, H286, H347, E300 and E028 levels could be observed after a residual air plasma treatment of a transition metal lean sample and so are not hydrogen or metal related. These levels are most probably equally passivated in the first region by the hydrogen treatment. The most interesting observation in the second region undoubtedly is the appearance of transition metal specific levels, which may be tentatively assigned to transition metal-hydrogen complexes. An overview of these levels compared with those of substitutional transition metal impurities is shown in in the band diagram in figure 6.15 and summarized in table 6.2.

No obvious trend in the (metal,H) levels compared with the substitutional metals is observed, similar to the case of Cu-passivation [10]. Only for Cr a similar hierarchy of (Cr,H) with respect to Cr is observed as for (Cu,H) with

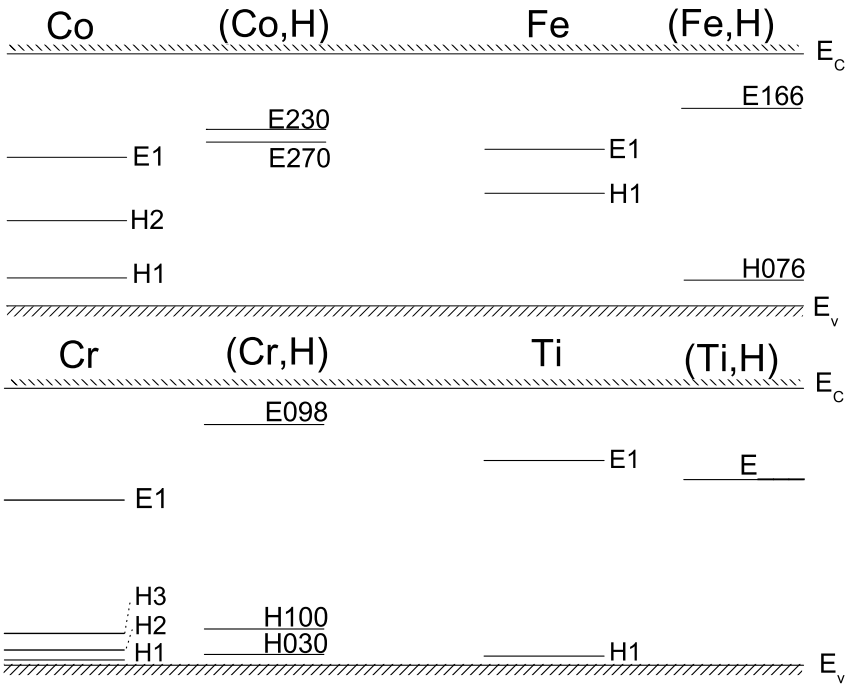

Figure 6.15: Energy level diagram of transition metal impurities (chapter 5 and reference [12]) compared to the new transition metal dependent levels, which are potential candidates for transition metal-hydrogen complexes.

respect to Cu. In both cases we are concerned with a triple acceptor + deep donor for the substitutional metal. Thus the H100 and H030 level may be tentativly assigned to the $Cr - H$ complex. For all the other levels no obvious assignment to a certain complex can be made and further research is necessary to gain better insight into the interaction of hydrogen with electrically active defects in germanium.

In the third region beyond $12\mu m$ again the substitutional transition metal impurity levels could be observed.

Table 6.2: Overview of signatures (E_T, K_T) of metal-specific levels observed after hydrogenation

Metal	Level	Carrier	$E_T(eV)$	$K_T(K^{-2}s^{-1})$
Co	E230	e	0.23	4×10^6
Co	E270	e	0.27	1.9×10^7
Fe	E166	e	0.166	1.5×10^7
Fe	H076	h	0.076	1.6×10^8
Cr	E098	e	0.098	2.1×10^6
Cr	H100	h	0.1	2.2×10^7
Cr	H030	h	0.03	4.5×10^7
Ti	E-	e	-	-

Due to the dominance of the radiation bands the new levels are difficult to study. For a more detailed investigation a higher concentration of metal specific levels should be formed in absence or at least a smaller concentration of irradiation defects. In the present setup plasma parameters such as gas pressure, voltage and temperature can be varied. The setup can however be modified such that remote H-plasma treatments also become possible, which cause less radiation damage by the plasma. As a third variant H-implantations may be programmed, which enable introduction of high concentrations of hydrogen in a controlled way. Finally a high concentration of transition metal-hydrogen complexes would be ideal to use the new numerical method (described in chapter 5) enabling to accurately determine capture cross-sections of the deep levels. The formation of transition metal impurities and transition metal-hydrogen complexes in more resistive germanium would make it possible to extend this numerical procedure to levels with a higher capture rate, such as acceptor levels in p-type.

Bibliography

[1] P. Siffert and E. Krimmel, editors. *Silicon. Evolution and future of a technology*, chapter C.A.J. Ammerlaan 'Hydrogen', pages 261–290. Springer-Verlag, 2004.

[2] J.I. Pankove and N.M. Johnson, editors. *Hydrogen in semiconductors*, volume 34 of *Semiconductors and semimetals*, chapter E.E. Haller 'Hydrogen-related phenomena in crystalline germanium', pages 351–380. Elsevier, 1991.

[3] R.E. McMurray, N.M. Haegel, J.M. Kahn, and E.E. Haller. Beryllium-hydrogen and zinc-hydrogen shallow acceptor complexes in germanium. *Solid state communications*, 61(1):27, 1987.

[4] J.M. Kahn, R.E. McMurray, E.E. Haller, and L.M. Falicov. Trigonal hydrogen-related acceptor complexes in germanium. *Physical review B*, 36(15):8001, 1987.

[5] S.J. Pearton and A.J. Tavendale. Hydrogen passivation of deep metal-related donor centers in germanium. *Journal of applied physics*, 54(2):820, 1983.

[6] S.J. Pearton. Deep metal-related centres in germanium. *Solid-state electronics*, 25(4):305, 1982.

[7] W.W. Tyler. Deep level impurities in germanium. *Journal of physical chemistry of solids*, 8:59, 1959.

[8] E. Simoen, P. Clauws, M. Lamon, and J. Vennik. Signature and capture cross section of copper-related hole traps in p-type high-purity germanium. *Semiconductors Science and Technology*, 1:53, 1986.

[9] P. Clauws, G. Huylebroeck, E. Simoen, P. Vermaercke, F. De Smet, and J. Vennik. DLTS of the third acceptor level of substitutional copper in germanium. *Semiconductor science and technology*, 4:910, 1989.

[10] E.E. Haller, G.S. Hubbard, and W.L. Hansen. Hydrogen-multivalent acceptor complexes in high-purity germanium. *IEEE Transactions Nuclear Science*, 24:48, 1977.

[11] J.M. Kahn, L.M. Falicov, and E.E. Haller. Isotope-induced symmetry change in dynamic semiconductor defects. *Physical review letters*, 57(16):2077, 1986.

[12] P. Clauws, J. Van Gheluwe, J. Lauwaert, E. Simoen, J. Vanhellemont, M. Meuris, and A. Theuwis. Deep level transient spectroscopy of transition metal impurities in germanium. *Physica B-Condensed matter*, 401:188, 2007.

[13] W.W. Tyler, R. Newman, and H.H. Woodbury. Properties of germanium doped with cobalt. *Physical review*, 97(3):669, 1955.

[14] S.J. Pearton, E.E. Haller, and J.M. Kahn. Quenched in deep acceptors in germanium. *Journal of physics C: Solid state physics*, 17:2375, 1984.

[15] A. Blondeel. *Ontwikkeling van optische varianten van 'Deep Level Transient Spectroscopy' voor de karakterisatie van hoog-zuiver n-type germanium.* PhD thesis, Universiteit Gent, 1998.

[16] S. Weiss and R. Kassing. Deep level transient fourier spectroscopy (DLTFS) - A technique for the analysis of deep level impurities. *Solid state electronics*, 31(12):1733, 1988.

[17] J. Fage-Pedersen, A.N. Larsen, and A. Mesli. Irradiation-induced defects in ge studied by transient spectroscopies. *Physical review B*, 62(15):10116, 2000.

[18] J. Van Gheluwe. *Karakterisering van CdTe/CdS en CuInS2-op-Cu-tape dunnefilmzonnecelllen met behulp van fotoluminescentiespectroscopie en 'deep level transient spectroscopy'.* PhD thesis, Universiteit Gent, 2007.

[19] E. Simoen. *Studie van ultra-zuiver Ge voor de fabrikatie van gamma-detectors met behulp van deep level transient spectroscopy.* PhD thesis, Universiteit Gent, 1984.

Appendix A

The capacitance transient amplitude in DLTS convergence for $t_p \to +\infty$

In this part a proof is given that the integral:

$$\lim_{t_p=+\infty} \frac{\Delta C(t_p)}{C_r} \propto \int_0^\infty \left(\frac{c_n n(x)}{e_n + c_n n(x)} - \frac{c_n n_r(x)}{e_n + c_n n_r(x)} \right) x dx, \tag{A.1}$$

which describes the amplitude of the DLTS-transient for an infinite filling pulse is convergent.

$$\begin{aligned}
\lim_{t_p=+\infty} \frac{\Delta C(t_p)}{C_r} &\propto \int_0^\infty \left(\frac{1}{\frac{e_n}{c_n n(x)} + 1} - \frac{1}{\frac{e_n}{c_n n_r(x)} + 1} \right) x dx \\
&= \int_0^\infty \left(\frac{\frac{e_n}{c_n n_r(x)} - \frac{e_n}{c_n n(x)}}{\left(1 + \frac{e_n}{c_n n(x)}\right)\left(1 + \frac{e_n}{c_n n_r(x)}\right)} \right) x dx \qquad \text{(A.2)} \\
&= \frac{e_n}{c_n} \int_0^\infty \left(\frac{\frac{1}{n_r(x)} - \frac{1}{n(x)}}{1 + \frac{e_n}{c_n n(x)} + \frac{e_n}{c_n n_r(x)} + \left(\frac{e_n}{c_n}\right)^2 \frac{1}{n_r(x) n(x)}} \right) x dx
\end{aligned}$$

$$= \frac{e_n}{c_n n_0} \int_0^\infty \frac{\exp_r(x) - \exp_p(x)}{1 + \frac{e_n}{c_n n_0}\left(\exp_p(x) + \exp_r(x)\right) + \left(\frac{e_n}{c_n n_0}\right)^2 \exp_p(x) \exp_r(x)} x dx$$

Herein $\exp_r$ and $\exp_p$ are describing the relative free carrier profiles during reverse bias and pulse bias respectively. Those functions can be written as:

$$\exp_{r/p}(x) = \exp\left(\frac{1}{4}\left(\frac{W_{r/p}-x}{\sqrt{2}L_D} + \sqrt{\frac{\left(W_{r/p}-x\right)^2}{2L_D^2}+1}\right)^2\right) \tag{A.3}$$

The argument of the $\exp_{r/p}$ function for the simplicity $fa_{r/p}$ can be written as (The depletion width in general named W, is W_r during reverse and W_p during pulse:

$$\begin{aligned} fa_{r/p} &= \frac{1}{4}\left(\frac{W-x}{\sqrt{2}L_D} + \sqrt{\frac{(W-x)^2}{2L_D^2}+1}\right)^2 \\ &= \frac{1}{4}\frac{(W-x)^2}{L_D^2}\left(1 + \frac{L_D^2}{(W-x)^2} + \sqrt{2}\frac{L_D}{W-x}\sqrt{\frac{W-x}{2L_D^2}+1}\right) \\ &= \frac{1}{4}\frac{(W-x)^2}{L_D^2}\left(1 + \frac{L_D^2}{(W-x)^2} + \text{signum}\,(W-x)\sqrt{1+\frac{2L_D^2}{(W-x)^2}}\right) \end{aligned} \tag{A.4}$$

Using Newtons binomial expansion to write the square root $\sqrt{1+\frac{2L_D^2}{(W-x)^2}}$ as a series for $x \to +\infty$. This series for $x > W - \sqrt{2}L_D$ can be written as:

$$fa_{r/p} = \frac{1}{8}\frac{L_D^2}{(W-x)^2} - \frac{1}{8}\left(\frac{L_D^2}{(W-x)^2}\right)^2 + \dots \tag{A.5}$$

Taking into account that for $y > 0$ and $y << 1$:

$$1 + \frac{y}{2} - \frac{y^2}{8} < \sqrt{1+y} < 1 + \frac{y}{2} - \frac{y^2}{8} + \frac{y^3}{16} \tag{A.6}$$

it can be shown that for $x > W - \sqrt{2}L_D$:

$$\frac{1}{8}\frac{L_D^2}{(W-x)^2}\left(1 - \frac{L_D^2}{(W-x)^2}\right) < fa_{r/p} < \frac{1}{8}\frac{L_D^2}{(W-x)^2} \tag{A.7}$$

From A.7 it can be seen that $\lim_{x=\infty} fa_{r/p} = 0$, which results in $\lim_{x=\infty} \exp_{r/p}(x) = 1$. This can physically interpreted as far from the junction the carrier concentration is n_0 which is independent of the reverse bias. Defining a constant $C^{integral}$ for a value $A > W_r - L_D/\sqrt{8}$ as:

$$C^i = \int_0^A \left(\frac{1}{\frac{e_n}{c_n n(x)}+1} - \frac{1}{\frac{e_n}{c_n n_r(x)}+1}\right) x dx \tag{A.8}$$

and using that property that $\exp_{r/p}(x) > 1$ and equation (A.7) to increase the first term and reduce the second term:

$$\begin{aligned}
& \lim_{t_p=+\infty} \frac{\Delta C(t_p)}{C_r} < \frac{\frac{e_n}{c_n n_0}}{\left(1+\frac{e_n}{c_n n_0}\right)^2} \int_0^\infty \left(\exp_r(x) - \exp_p(x)\right) x dx \\
< \quad & C^i + \frac{\frac{e_n}{c_n n_0}}{\left(1+\frac{e_n}{c_n n_0}\right)^2} \int_A^\infty (\exp\left(\frac{1}{8}\frac{L_D^2}{(W_r-x)^2}\right) - \\
& \exp\left(\frac{1}{8}\frac{L_D^2}{(W_p-x)^2}\left(1-\frac{L_D^2}{(W_p-x)^2}\right)\right)) x dx \\
< \quad & C^i + \frac{\frac{e_n}{c_n n_0}}{\left(1+\frac{e_n}{c_n n_0}\right)^2} \int_A^\infty \left(\exp\left(\frac{1}{8}\frac{L_D^2}{(W_r-x)^2}\right)\left[1-\exp\left(-\frac{1}{4}\frac{L_D^2}{(W_r-x)}\right)\right]\right) x dx \\
< \quad & C^i + \frac{\frac{e_n}{c_n n_0}}{\left(1+\frac{e_n}{c_n n_0}\right)^2} \int_A^\infty \exp\left(\frac{1}{8}\frac{L_D^2}{(W_r-x)^2}\right)\left[\frac{1}{8}\frac{L_D^4}{(W_r-x)^4}\right] x dx
\end{aligned} \tag{A.9}$$

For the last two steps the properties that for a pulse in DLTS $W_r > W_p$ and the fact that $\exp(x) > 1 - x$ were used. For the integral A.9 a primitive function can be found:

$$\begin{aligned}
& \int \frac{1}{8} \exp\left(\frac{L_D^2}{8\left(W_r-x\right)^2}\right) \frac{x L_D^4}{\left(W_r-x\right)^4} dx = \\
& \frac{L_D^2 \exp\left(\frac{L_D^2}{8(W_r-x)^2}\right) x + \sqrt{2\pi} L_D W_r \left(x - W_r\right) \hat{i}\,\mathrm{erf}\left(\frac{\hat{i}\, L_D}{2\sqrt{2}(W_r-x)}\right)}{2\left(W_r-x\right)}
\end{aligned} \tag{A.10}$$

Herein $\hat{i}$ is the imaginary number and erf is the error function. It can be seen that this primitive function convergences to $-L_D^2/2$ for $x \to \infty$. Because the original integral was clamped by the upper limit given by A.10 and is positive it can be seen that the DLTS-signal is convergent.

Appendix A: The capacitance transient amplitude in DLTS convergence for $t_p \to +\infty$

Appendix B

Solving the neutrality equation

To solve the neutrality equation in a semiconductor as a function of temperature and the respective the free electron and hole concentration, an iterative method was implemented.

$$n + \sum N_A^- = p + \sum N_D^+ \tag{B.1}$$

All terms within this equation are dependent on the chemical potential and thus the problem reduces to finding the chemical potential $\mu(T)$. In this method the energies are relative to the valence band energy. Thus physically it can be understand or mathematically it can be shown that:

$$\frac{dQ}{d\mu} < 0 \tag{B.2}$$

This makes it possible to use the a similar method as for $F = G$ method to find to zero crossing. The fractional occupation of deep levels is calculated using:

$$f_T = \frac{1}{e^{\frac{G_T - \mu}{k_B T}} + 1} \tag{B.3}$$

The free carrier concentrations are calculated using the Fermi-Dirac $F_{1/2}$ distribution

$$n = N_C F_{1/2}\left(\frac{\mu - G_C}{k_B T}\right)\frac{2}{\sqrt{\pi}} \tag{B.4}$$

which can be approximated using the formula of Aymerich-Humet [1]:

$$T = 3 * \sqrt{\frac{\pi}{2}} \left(E + 2.13 + \left(|E - 2.13|^{2.4} + 9.6 \right)^{5/12} \right)^{-1.5} \tag{B.5}$$

$$F_{1/2} = \sqrt{\frac{\frac{\pi}{4}}{e^{-E} + T}} \tag{B.6}$$

[1] Aymerich-Humet 1983 Journal of applied physics 54(5) 2850-2851

Appendix C

Overview of experimental techniques

In this appendix a list of experimental techniques used in this work and the information one expects to extract from them is given.

Capacitance-Voltage profiling Method to measure the free carrier density from the capacitance of the depletion width of the device as a function of the applied bias.

Infrared absorption spectroscopy Spectroscopic technique to measure the absorption spectrum, this method can detect both electrical and vibrational transitions.

Photo-Thermal Ionization Spectroscopy (PTIS) Photoconductivity variant of infrared absorption spectroscopy, with as main advantage the lower detection limit for electrically active defects.

Deep Level Transient Spectroscopy (DLTS) Conventional DLTS is used to identify deep levels within the band gap of a semiconductor by evaluating the capacitance transient as a function of temperature. Different isothermal variants are possible: from variation of biases one can deduce the spatial profile of the trap level and variation of measurement window

can be used to measure the emission rate. The variation of the filling pulse length makes it possible to deduce the capture cross-section of the level (see chapter 5).

Laplace Transform Deep Level Transient Spectroscopy High resolution variant of isothermal DLTS that uses numerical inversion of Laplace transform to deduce the emission rate of the capacitance transient.

Slow Positron Depth Profiling Technique to measure open volume defects based on the Doppler broading of the gamma-rays created by the annihilation of a positron. To measure a spatial dependence the positrons are implanted with different kinetic energies.

Raman Spectroscopy Spectroscopic technique that measures the Raman-shift of the laser wavelength used for the excitation. This technique gives complementary information to local vibrational mode absorption spectroscopy.

Electron Microscopy Microscopical technique that uses electrons to illuminate the sample and make an enlarged image. Scanning Electron Microscopy (SEM) is used to study the surface of a sample by detecting low energy secundary electrons. Transmission Electron Microscopy (TEM) is used to study bulk defects by transmission of electron through a thin sample.

Nederlandstalige samenvatting

Het is bekend dat in p-type Cz-Si tijdens een H-plasmabehandeling een p-n junctie nabij het oppervlak wordt gevormd. De diepte van de junctie hangt af van de duur van de plasmabehandeling en kan verklaard worden aan de hand van de indiffusie van waterstof. De diepte van de junctie wordt groter door een nabehandeling en stijgt met de temperatuur ervan. In de literatuur werd tot nog toe aangenomen dat de omslag van p- naar n-type materiaal gebeurt door de versnelde vorming van thermische donoren (OTD), waarbij waterstof als een soort van katalysator optreedt. Capaciteit-spanning metingen (C-V) gecombineerd met Deep Level Transient Spectrscopy (DLTS) hebben echter aangetoond dat dit beeld niet volledig klopt - zeker niet voor een uitgloeitemperatuur beneden 350°C.

De DLTS-waarnemingen leidden tot het besluit dat er bij een behandelingstemperatuur beneden 340°C naast OTDs vermoedelijk nog ondiepere donoren worden gevormd, die evenwel niet toegankelijk zijn voor DLTS. Om dit te onderzoeken werden een aantal monsters onderzocht met IR-spectroscopie. Wegens de geringe absorptie (de donoren bevinden zich immers in een laag van slechts enkele tientallen μm dik, waardoor slechts enkele zwakke lijnen van ondiepe donoren worden waargenomen) dienden we beroep te doen op Photo-Thermal Ionization Spectroscopy (PTIS), waarbij de elektronische overgangen worden gedetecteerd in fotogeleiding bij lage temperatuur. Het monster wordt daarbij voorzien van ohmse contacten bovenop het behandelde oppervlak. Zowel in het p-type Cz-Si als in het n-type MCz-Si werden naast de bekende lijnen van de B- of de P-dotering ook nieuwe lijnen aangetroffen afkomstig van ondiepe

donoren met een bindingsenergie in de buurt van 40meV; deze lijnen bevinden zich in het ver-IR gebied. Enkele van deze lijnen werden eerder gerapporteerd in H-gedoteerd n-type Si en toegeschreven aan partieel gepassiveerde OTDs, waarbij het waterstof deel uitmaakt van het gevormde defect. Andere lijnen werden nog niet eerder gerapporteerd en konden toegeschreven worden aan een effectieve-massa donor. Bij hogere meettemperatuur worden overgangen waargenomen van vroege OTDs, wat in overeenstemming is met de DLTS waarnemingen. De PTIS metingen bevestigen het beeld dat bij lage behandelingstemperaturen niet enkel diepe maar ook ondiepe donoren worden gevormd; het waterstof speelt daarbij niet enkel de rol van katalysator maar neemt zelf actief deel aan de donorvorming.

Waterstofdefecten in germanium werden tot nog toe slechts weinig onderzocht in vergelijking met silicium. Een van de redenen is de blijkbare moeilijkheid om waterstof door diffusie in te brengen. Gezien de grote heropleving van de belangstelling voor germanium als materiaal voor elektronische toepassing en het belang van processen waarbij waterstof een rol speelt, is een studie van defecten die met waterstof verband houden hoogst interessant. Voor de H-dotering werd een waterstof-plasmareactor van eigen ontwerp gebouwd. Het betreft een direct-plasmaopstelling waarbij het specimen op een instelbare temperatuur kan worden gehouden met een door een temperatuurcontroller gestuurde lamp en waterkoeling. De doelmatigheid van de opstelling werd uitvoerig gecontroleerd aan de hand van verschillende H-behandelingen van Si die uit de literatuur bekend zijn. Zo werden passivatie van B-acceptoren, diodevorming in p-type Cz-Si en het onstaan van waterstof 'platelets' waargenomen.

Waterstofplasmabehandeld germanium werd onderzocht met verschillende experimentele technieken. Met behulp van TEM (Transmission Electron Microscopy, uitgevoerd dr. M.-L. David, Univ. Poitiers) werd aangetoond dat een H-plasmabehandeling aanleiding geeft tot vorming van een 300nm dikke defectrijke laag, met daarin plaatvormige clusters van caviteitjes van ongeveer 5nm diameter. Deze laag werd verder bestudeerd met Slow Positron Annihilation Spectrsocopy (Dr. J. De Baerdemaeker, Ugent). De positronsignatuur

van de waargenomen defecten correspondeert met multiple vacaturen V_n met $n \geq 3$. Door behandeling bij temperaturen tot 400°C wordt de concentratie van deze openvolumedefecten verlaagd. Een dergelijke behandeling blijkt ook gepaard te gaan met omvorming van de aanwezige defecten tot schilfers aan het oppervlak die waarneembaar zijn met optische microscopie. De interpretatie van de waarnemingen is dat het ingebrachte waterstof nucleëert in plaatvormige structuren, waarin de druk van het waterstofgas toeneemt door thermische behandeling met schilfering als gevolg. Deze experimenten hebben voor het eerst aangetoond dat H- plasmabehandeling van Ge mogelijk dezelfde rol kan spelen als bij Si, als goedkoop alternatief voor H-implantatie bij de fabricatie van Ge-On-Insulator (GeOI) substraten met behulp van het 'smart cut' proces. Hierbij wordt H geïmplanteerd in een donorplak, waarna in een uitgloeistap de plak splitst op de plaats waar de implantatie zich situeert en een dunne laag van de donorplak achterblijft op een dragerplak (Si+SiO2).
In de specimens behandeld in de plasmareactor van de UGent werden IR-absorptiebanden waargenomen bij 630 en 1980cm^{-1}. Deze werden toegewezen aan de 'wag' en 'stretch' mode van Ge-H bindingen. De 1980 cm^{-1} mode werd voordien enkel waargenomen met Raman-spectroscopie en werd toegeschreven aan Ge-H bindingen in plaatvormige clusters. De goede waarneembaarheid van de absorptie toont aan dat met onze plasmareactor wellicht grotere H-concentraties worden ingebracht dan met andere opstellingen. De IR-band kan worden gezien als de tegenhanger van een band in Si rond 2100cm^{-1}. De H-concentratie na een plasmabehandeling op 0-150°C wordt geschat op $10^{16} - 10^{17} cm^{-3}$. De absorptie neemt af met stijgende behandelingstemperatuur en de absorptieband wordt t.z.t asymmetrischer, met een verschuiving van het maximum van 1997 naar 2021cm^{-1} voor behandeling bij respectievelijk 150 en 250°C. Na een bijkomende behandeling bij 400°C, waarbij de totale absorptie verder afneemt, worden scherpere banden waargenomen met in het 150°C spectrum twee componenten. De waarnemingen zijn in goede overeenstemming met DFT-berekeningen van de vibratiefrequenties van een (2Ge-H + nH_2) model, d.w.z. een dubbele laag van Ge-H bindingen met een variatie

aan moleculaire waterstof in de nabijheid.
Met DLTS (Deep Level Transient Spectroscopy) werd aangetoond dat zich in de gestoorde laag elektrisch actieve defecten bevinden. Energieniveaus worden waargenomen op 0.24 eV beneden de conductieband en 0.17 eV boven de valentieband. Een andere, brede band vertoont de kenmerken van oppervlak- of grensvlaktoestanden.
Met behulp van DLTS werd ook de electrische passivatie van transitiemetaal onzuiverheden met behulp van waterstof bestudeerd. Hiervoor beschikten we over p-type en n-type germanium plakken die opzettelijk verontreinigd werden door implantatie met 3d transitiemetalen. Omdat over de elektrische eigenschappen van de meeste transitiemetalen nog geen literatuurgegevens beschikbaar zijn, was een grondige studie vóór de plasmabehandeling noodzakelijk. De traditionele DLTS-methode maakte het mogelijk om de energieniveaus in de verboden zone als gevolg van deze onzuiverheden waar te nemen. Hierbij bestudeert DLTS de emissiekarakteristiek van de ladingsdragers, hetgeen leidt tot het nauwkeurig bepalen van de emissiesignatuur. Om deze schijnbare vangstwerkzamedoorsnede en emissie-energie te corrigeren zodat de werkelijke ligging van het energieniveau en de entropieverandering bij emissie kunnen worden bepaald is het noodzakelijk om de vangstwerkzame doorsnede te kennen. In het kader van dit doctoraatsonderzoek werd deze standaard DLTS-methode uitgebreid met een nieuwe methode om de vangstwerkzamedoorsnede voor meerderheidsladingsdragers van deze niveaus te bepalen. Deze methode is gebaseerd op de theoretische beschrijving van de capaciteitstransientamplitude in functie van de lengte van de vulpuls ($S(t_p)$). Een nauwkeurige analytische benadering van de $S(t_p)$-functie onafhankelijk van het emissie- en vangsttempo maakte het mogelijk om een gebruiksvriendelijk fitprogramma te implementeren. Hierbij werd rekening gehouden met het tragevangstregime in de debyestaarten van het depletiegebied en de aanwezigheid van een onbekend profiel van het vangstcentrum. Met behulp van deze unieke methode kon de ionizatie enthalpie van de niveaus bekomen worden. Voor Co, Fe en Ni waren reeds literatuurgegevens bekend uit Hall-effect metingen, hiermee werd dan

ook een zeer goede overeenkomst gevonden. De methode laat toe om ook de invloed van deze niveaus op de levensduur van de ladingsdragers te bepalen. Door deze grondige karakterisatie kon het metaalgeïmplanteerde materiaal gebruikt worden als startmateriaal voor een passivatiestudie.
Na een behandeling van 4u op 200°C blijken de niveaus van de substitutionele metalen volledig verdwenen te zijn tot op een diepte van ongeveer 6 μm, terwijl geen verandering van de concentratie van de ondiepe dopanten (Sb in n-type, Ga in p-type) waargenomen wordt. Dieper in het materiaal worden echter nieuwe DLTS-banden waargenomen, die verschillen naargelang het origineel geïmplanteerde metaal. Deze banden worden voorlopig toegeschreven aan metaal-waterstof complexen. Aangezien de vermelde metalen allemaal multipele acceptoren zijn, levert binding met H mogelijkheden voor volledige of gedeeltelijke passivatie, naargelang het aantal aangehechte H-atomen. Daarnaast werden ook nog vier defectniveaus gevonden die onafhankelijk zijn van het soort metaal en waarvan één eerder toegeschreven werd aan de di-vacature. Het analoge uitgloeigedrag van deze laatste banden evenals hun aanwezigheid in H-plasmabehandeld referentiemateriaal zonder metaalimplantatie, suggereert dat alle vier de banden wellicht kunnen toegewezen worden aan stralingsschade bij de behandeling.